On the discretisation of actuation in locomotion

Impulse- and shape-based modelling for hopping robots

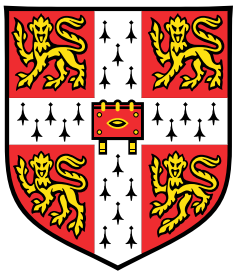

Fabio Felice Giardina

Department of Engineering
University of Cambridge

This dissertation is submitted for the degree of
Doctor of Philosophy

Darwin College

April 2018

Declaration

I hereby declare that except where specific reference is made to the work of others, the contents of this dissertation are original and have not been submitted in whole or in part for consideration for any other degree or qualification in this, or any other university. This dissertation is my own work and contains nothing which is the outcome of work done in collaboration with others, except as specified in the text and Acknowledgements. This dissertation contains fewer than 65,000 words including appendices, bibliography, footnotes, tables and equations and has fewer than 150 figures.

Fabio Giardina, April 2018

Acknowledgements

My time at the University of Cambridge has been a unique experience, and I had the opportunity to meet and work with outstanding people who supported and inspired me throughout my studies, and to whom I would like to express my deepest gratitude. First, I would like to thank my supervisor Dr. Fumiya Iida for giving me the opportunity to come to Cambridge. His constant support and the many stimulating meetings motivated me throughout my doctoral studies. I would further like to thank my PhD examiners Professor Rodolphe Sepulchre and Professor Auke Ijspeert for their valuable input to my work. The inspiring discussion with them during my viva helped me to clarify my work and sharpen my arguments.

My parents and sister have been of greatest support throughout my studies and in any other aspect of my life, and I am thankful for their endless care, understanding, and encouragement.

Throughout my PhD, I was privileged to have worked with amazing engineers, scientists and friends. To begin with, my colleagues with whom I shared most experiences in the bio inspired robotics lab, Professor Andre Rosendo and Josie Hughes. I greatly enjoyed working with them and I am thankful for their friendship and support. I further would like to thank my colleagues Dr. Utku Culha, Dr. Fabian Guenther, Dr. Alessandro Crespi, and Simon Birrell for making my time in the bio inspired robotics lab so enjoyable.

I would like to thank my peers Steve Heim, Amarjot Singh, Marco von Atzigen, and Vuk Vujovic, for being both personally and intellectually supportive to me.

I was privileged to be working with remarkable fourth year engineering students and internship students and would like to thank Jonathan Hunt, Jia Lei Wang, Kaur Aare Saar, Davide Bray, and Remma Matsuda for their great effort and for making working with them so stimulating.

I am deeply thankful also to my college, Darwin College, for giving me a second home. I would like to thank all my college friends, especially Tania Amoiridou, Vagheesh Narasimhan, Amani Zalzali, Anjali Mehrotra, Anh Khoa Doan, Adam Boyce, and my band mates from the GalapaGoGos.

Lastly, I would like to thank my Swiss friends, especially Patrick Fellmann, Patrick Suhner, and Marc Zimmermann, who never forgot about their friend in Cambridge and who made me feel at home when I wasn't.

Abstract

In an age where computers challenge the smartest human beings in cognitive tasks, the conspicuous discrepancy between robot and animal locomotion appears paradoxical. While animals can move around autonomously in complex environments, today's robots struggle to independently operate in such surroundings. There are many reasons for robots' inferior performance, but arguably the most important one is our missing understanding of *complexity*.

This thesis introduces the notion of *discrete actuation* for the study of locomotion in robots and animals. The actuation of a system with discrete actuation is restricted to be applied at a finite number of instants in time and is impulsive. We find that, despite their simplicity, such systems can predict various experimental observations and inspire novel technologies for robot design and control. We further find that, through the study of discrete actuation, causal relationships between actuation and resulting behaviour are revealed and become quantifiable, which relates the findings presented in this thesis to the broader concepts of complexity, self-organisation, and self-stability.

We present four case studies in Chapters 3-6 which demonstrate how the concept of discrete actuation can be employed to understand the physics of locomotion and to facilitate novel robot technologies. We first introduce the *impulsive eccentric wheel model* which is a discretely actuated system for the study of hopping locomotion. We find that the model predicts robot hopping trajectories and animal related hopping characteristics by reducing the dynamics of hopping–usually described by hybrid differential equations–to analytic maps. The reduction of complexity of the model equations reveals the underlying physics of the locomotion process, and we identify the importance of robot shape and mass distribution for the locomotion performance. As a concrete application of the model, we compare the energetics of hopping and rolling locomotion in environments with obstacles and find when it is better to hop than to roll, based on the fundamental physical principles we discover in the model analysis. The theoretical insights of this modelling approach enable new actuation techniques and design for robots which we display in *Robbit*; a robot that uses strictly convex foot shapes and rotational impulses to induce hopping locomotion. We show that such systems outperform hopping with non-strictly convex shapes in terms of energy effective

and robust locomotion. A system with discrete actuation motivates the exploitation of shape and the environment to improve locomotion dynamics, which reveals advantageous effect of inelastic impacts between the robot foot and the environment. We support this idea with experimental results from the robot *CaneBot* which can change its foot shape to induce timed impacts with the environment. Even though inelastic impacts are commonly considered detrimental for locomotion dynamics, we show that their appropriate control improves the locomotion speed considerably.

The findings presented in this thesis show that discrete actuation for locomotion inspires novel ways to appreciate locomotion dynamics and facilitates unique control and design technologies for robots. Furthermore, discrete actuation emphasises the definition of causality in complex systems which we believe will bring robots closer to the locomotion behaviour of animals, enabling more agile and energy effective robots.

Preface

The content of this dissertation is based on four peer-reviewed publications. The content of the publications has been edited and extended to match this thesis. The publication from which the content of a chapter is derived is indicated on the first page of the respective chapter. All projects are the result of collaborative work with Dr. Fumiya Iida. My personal contribution to the project will be mentioned on the first page of every chapter. As this thesis is the result of four independent projects, there is some overlap between the chapters.

The publications are:

1. Fabio Giardina and Fumiya Iida. Collision-based energetic analysis of rolling and hopping over obstacles. *PLOS ONE*, 13(3), 2018.

2. Fabio Giardina and Fumiya Iida. Efficient and stable locomotion for impulse-actuated robots using strictly convex foot shapes. *IEEE Transactions on Robotics*, 2018.

3. Fabio Giardina and Fumiya Iida. Simulation of forward hopping dynamics in robots and animals using a template with a circular foot and impulsive actuation. In *Biomedical Robotics and Biomechatronics (BioRob), 2016 6th IEEE International Conference on*, pages 7–12. IEEE, 2016.

4. Fabio Giardina and Fumiya Iida. Discrete foot shape changes improve dynamics of a hopping robot. In *International Symposium on Experimental Robotics*, pages 113–122. Springer, 2016.

Table of contents

Declaration iii

Acknowledgements v

Abstract vii

Preface ix

List of figures xv

List of tables xvii

1 Introduction 1

1.1 Discrete Actuation . . . 3

1.1.1 The Process of Discretisation . . . 6

1.2 Modelling Terrestrial Locomotion . . . 8

1.2.1 Morphology . . . 9

1.2.2 Actuation . . . 11

1.2.3 Control Laws . . . 13

1.2.4 Other Modelling Aspects . . . 16

1.3 Objectives . . . 16

1.4 Contributions . . . 17

1.4.1 Physics of Locomotion . . . 17

1.4.2 Locomotion Actuation and Control . . . 18

1.4.3 Self-Organisation . . . 19

1.5 Structure of Dissertation . . . 19

2 Planar Rigid Body Contact Dynamics 21

2.1 Planar Rigid Body Kinematics . . . 22

2.2 Constrained Rigid Body Dynamics 24
2.3 Inelastic One-Contact Collision without Friction 25
2.4 Impulsive Actuation 27
2.5 Multi-Contact Collision with Friction 27
2.5.1 Set-Valued Functions 28
2.5.2 The Linear Complementarity Problem 29
2.5.3 The Multi-Contact LCP with Friction and Impacts 30
2.5.4 Time Stepping Algorithm 32

3 The Impulsive Eccentric Wheel Model 33
3.1 Introduction 33
3.2 Template 35
3.2.1 Derivation of Template Equations 36
3.3 Simulation Set-Up 39
3.4 Results 40
3.4.1 Template behaviour 40
3.4.2 Cargo Trajectory Comparison 44
3.4.3 Hopping Animal Comparison 44
3.5 Conclusion 46

4 Energetics of Surpassing Obstacles 47
4.1 Introduction 47
4.2 Methods 51
4.2.1 Model Assumptions 51
4.2.2 Rotational Hopping Strategy 51
4.2.3 Rolling Strategy 54
4.2.4 Trivial Hopping Strategy 55
4.2.5 Allometric Scaling Laws 55
4.2.6 Experimental Set-Up 56
4.3 Results 57
4.3.1 Theoretical Results of the Rotational Hopping Strategy 57
4.3.2 Mass-Independent Theoretical Results 59
4.3.3 Animal-Related Theoretical Results 60
4.3.4 Experimental Results 63
4.4 Discussion 65

5 Rotational Impulses for Robot Locomotion 69
5.1 Introduction . . . 69
5.2 Locomotion Model . . . 71
5.2.1 Constrained Equations of Motion . . . 71
5.2.2 Impulsive transitions . . . 73
5.2.3 Locomotion with Strictly Convex Shapes . . . 73
5.3 Stability of Locomotion . . . 76
5.3.1 Finding Periodic Solutions . . . 76
5.3.2 Stability of Fixed Points . . . 79
5.3.3 Performance of Control . . . 81
5.4 Robot Design . . . 85
5.5 Experimental Results . . . 86
5.6 Discussion . . . 89
5.7 Conclusion . . . 92

6 Improving Hopping Dynamics with Inelastic Impacts 93
6.1 Introduction . . . 93
6.2 Methods . . . 95
6.3 Results . . . 96
6.4 Analysis . . . 100
6.5 Conclusion . . . 102

7 Conclusions 103
7.1 Discussion of Contribution . . . 103
7.2 Related Work . . . 107
7.3 Future Work . . . 108

References 111

Appendix A Energetic Analysis of the Eccentric Wheel Collision 125
A.1 Eigenvalues and Eigenvectors of the Collision Matrix . . . 125
A.2 Wheel-Obstacle Energy Loss due to Collision . . . 126
A.3 Limit Case of Hopping vs. Rolling . . . 126
A.4 Eigenvalue Ratio . . . 127

Appendix B Extension to Chapter 5 129

Appendix C Self-Stability of the Impulsive Wheel **133**
C.1 The impulsive Wheel Model 133
C.2 Discrete-Time Dynamics of the Impulsive Wheel 136

List of figures

1.1 Discretisation of dynamics 7

2.1 Contact kinematics 23
2.2 Unilateral primitive and set-valued relay function 28

3.1 Sketch of template 35
3.2 Cargo robot 40
3.3 Cargo efficiency and velocity 41
3.4 Template time series of the impulsive eccentric wheel 42
3.5 Impulsive eccentric wheel model trajectories 45
3.6 Model predictions for kangaroo rats and wallabies 46

4.1 Locomotion strategies 50
4.2 Rotational hopping model 52
4.3 Experimental set-up 57
4.4 Costs for rotational hopping strategy 58
4.5 Comparison of rotational hopping strategy and rolling strategy 60
4.6 Strategy comparison for animal related parameters 62
4.7 Motion progression of experimentally tested strategies 63
4.8 Experimental collision loss for rolling and trivial hopping strategies 64
4.9 Prediction error of energetic collision loss for rotational hopping strategy . 65

5.1 Definition of shape 72
5.2 Locomotion of arbitrary strictly convex shape through momentum-stored impulse 74
5.3 Diversity of hopping behaviour for different shape functions in simulation . 75
5.4 Fixed point actuation from nonlinear optimisation 78
5.5 Stability of the off-centred wheel model 80
5.6 Simplified hopping model of non-strictly convex shapes 82

5.7 Locomotion speed as a function of impulse per travelled distance 84
5.8 Mechanism of the brake for impulse transmission 85
5.9 The off-centred disc robot *Robbit*. 86
5.10 Series of pictures of *Robbit* 87
5.11 Centre of mass trajectories of *Robbit* 88
5.12 Experimental converged hopping speeds of *Robbit* 90

6.1 The robot *CaneBot* 94
6.2 Open-loop control 96
6.3 Robot progression over one period T 97
6.4 *CaneBot* trajectories 98
6.5 Averaged travelled distance per hop of *CaneBot* 99
6.6 Fastest trajectory of *CaneBot* 100
6.7 Observed take-off positions 101
6.8 Transient trajectories of *CaneBot* 102

A.1 Interpretation of eigenvectors 126

C.1 Impulsive wheel model 134
C.2 Bifurcation diagram of impulsive wheel 137
C.3 Iteration-series of impulsive wheel for various impulse magnitudes 138

List of tables

3.1 Parameter ranges of template for simulated cases. 43

5.1 Parameter ranges for simulation and robot. 76

Chapter 1

Introduction

Robots' great potential in supporting humanity and human endeavours promises to enhance numerous aspects of our lives. Exploratory ventures, search and rescue missions, and the support of the elderly are only a few examples where robots can have a significant economical and cultural impact. However, the success of robots in these areas stands or falls by their capacity to cope with a complex and uncertain environment. Today's industrial robots function in well-defined and simplified domains, but struggle to operate in difficult surroundings such as disaster areas. Machines that can purposefully operate in these areas are urgently needed, as the 2011 Fukushima incident showed: a tsunami-caused energy accident unleashed considerable amounts of radioactive material. While repair work during the incident posed a lethal task for humans, autonomous robots could have been employed to repair the critical damage. Initiatives like the DARPA robotics challenge[1] were launched to stimulate the development of such systems which can solve "complex tasks in dangerous, degraded, human-engineered environments". Even though there have been substantial advances in the autonomy of robots since the Fukushima incident, robots operating in the highly challenging and uncertain environment are still not living up to their potential.

The poor performance of robots in natural surroundings is surprising, especially in an age where artificial intelligence is surpassing humans in cognitive tasks. For instance, the recent achievements of the company *DeepMind* in the game of *Go* have shown that a computer can outperform the best human player in a game where high intelligence and intuition is required. Bizarrely, it also emphasises the shortcomings of today's artificial intelligence: even though the algorithm based on deep neural networks and reinforcement learning *AlphaGo* learned to beat the human world champion [1], it is to this day impossible to build a machine that can *reliably* pick up the game stones and place them precisely on the board - a task a two year old kid could do. This is not to say that it is impossible to build a robot arm which

[1] https://www.darpa.mil/program/darpa-robotics-challenge

can recognise a stone, pick it up, and place it on the targeted place on the board, but that any uncertainty in any of these tasks may lead to a situation that terminates the operation and human involvement is needed. For instance, the stone may slip out of the robot's grip and roll under the table. There is currently no robot which can account for and deal with such unexpected events. This observation relates to Moravec's paradox [2], which states that computation for abstract reasoning is much lower than for sensorimotor interaction with the environment, even though we think of the first as being much more involved than the latter.

In other words, the abstract thought and reasoning of a sequence of actions may be simpler than executing the action. While the sequence of actions involves logic and a finite number of events in an abstracted environment, the action itself is an operation taking place in continuous space, continuous time, in an uncertain environment consisting of a myriad of influencing factors. Such a setting where many parts are interacting with each other and form a global behaviour is subject to *complexity*. Complexity in a dynamical system is often characterised by nonlinearities, non-smoothness of the behaviour, and high dimensionality. Even though we are well aware of the optimal control of robots that are governed by linear dynamical systems–an abstraction of reality avoiding nonlinearities and non-smoothness–the same tools have only limited success when applied to robots operating in real environments. A robot operating in the real world needs to learn the rules of complexity before being able to purposefully act in it.

Animals living and operating on our planet need to have learned these rules and it is possible that the tools of nature to deal with complexity can be reverse-engineered. Indeed, scientists have recognised that the brain is the likely source of cognition and abstract thought, which inspired engineers to design systems equipped with a central computing unit that controls and coordinates entire systems. However, the identification of the central nervous system as the sole source of computation and coordination is only a hypothesis and need not be correct. There exist views of autonomy and intelligence that emphasises the role of the body for computation and coordination in animals, stating that motion control is decentralised and distributed in the body and the brain. The design of a centralised processing unit for computation and the one of decentralisation is reflected in the two philosophical views of *computationalism* [3], which states that thinking is a form of computing, and *embodiment* [4], which assumes that cognition can only be understood in the context of a physical body.

Instead of simplifying the nonlinearities in the robot, embodiment advises to exploit these effects to achieve a desired behaviour. Although the concept appears abstract and hard to quantify with our current tools, it deeply connects to engineering ideologies which use the morphology of the body to simplify the control problem. As will be discussed later, the ideas of *global entrainment* [5], *morphological computation* [6], *synergetics* [7], and *self-stability*

[8] address the idea of embodiment and will be useful in developing new theories for design and control of robots.

Embodiment is exemplified in animals and machines by locomotion – the ability to move around in an environment. Without a body that interacts with its surroundings, locomotion is impossible, which shows that locomotion is not solved by computation alone. The interaction of the nervous system, the body, and the environment give rise to complexity, which, as discussed previously, renders the use of standard engineering approaches problematic. Furthermore, locomotion exploits nonlinearities and non-smoothness that arise in the dynamic interaction with the environment, to the extent that the linearised dynamics of the system cannot give rise to the phenomenon of locomotion. The necessity for locomotion to exploit complexity makes it a hard problem to engineer, but at the same time provides a motivation to study and develop novel tools for design and control of systems that can deal with the complexity of reality.

The state of understanding complex systems is reached once we can unambiguously define *cause* and *effect* of an observed property. However, in reality it is often hard to define a cause, especially in a complex system where many properties need to hold for a particular effect to occur. Take for example a running human. What is the cause that effects the running behaviour? There is most likely no single satisfying answer to this question, as cause and effect are not graspable on this level of inquiry. The behaviour arises due to an intricate relationship between the morphology, actuation, control laws, and the environment. In the next section, the concept of *discrete actuation* is introduced which addresses the problem of defining a *cause* in locomotion.

1.1 Discrete Actuation

An actuator is a component of a robot which can exert forces to the bodies it is connected to. The closest equivalent of a robotic actuator in biology is a muscle, which analogously exerts forces on the ends it is connected to. In this thesis we will use the terms actuator and actuation in a more general context by meaning a mechanism in a dynamical system with which the system states can be influenced and which acts upon the instructions of a control law. This of course includes robotic actuators and muscles, where the control law is generated by the central processing unit and the brain, respectively. Actuators generally exert finite forces on the system over a period of time, which causes a change in the velocity and posture of the system. We would like to explore the subset of actuation which can change velocity and posture in a time instant rather than over an extended time interval. We state the following definition

Definition 1.1.1. Discrete actuation. A *discrete actuation* in a dynamical system is an actuation that can influence the system states only at a finite number of instants in time and that is impulsive in these instants.

This implies that the actuation can induce events where velocity and posture states are discontinuous. We will mostly consider discontinuous velocity changes due to discrete actuation, but will come back to discontinuous posture changes in Chapter 6 where we consider instantaneous foot shape changes in a robot. As an example of a discontinuous velocity change, take for instance the dynamics of a bouncing ball on an actuated paddle: the dynamics are governed by the equation of motion of the ball in the gravitational field, and the ball is actuated through the collision with the moving paddle at which point its velocity is reversed. The actuation in this system is discrete, as it is zero almost all the time and only changing at the singular instance of the impulsive ball-plate collision. We are interested in translating dynamical systems as observed in reality by a discretely actuated equivalent model because the complexity of the discretised system can often be drastically reduced while preserving many aspects of the original dynamics. Most importantly, the effect of an actuation can be uniquely attributed to a cause in time, which is paramount to understand complex dynamical systems. One of the first success stories of modelling through discrete actuation is due to Holmes [9]. In his 1982 paper, Holmes shows the dynamical richness of the bouncing ball on a vibrating plate, which is described by only one difference equation. Depending on the system parameters, the behaviour of the bouncing ball can vary from a stable period-1 behaviour all the way to chaotic motion. This example beautifully shows the power of discrete actuation by capturing the complex dynamics of a real system by a single difference equation which represents the richness of the infinite number of existing solutions.

The importance of impulsive events is also evident in the study of terrestrial locomotion, where repetitive collisions of the legs with the ground occur. Theoretical locomotion models underlying impulsive events are helpful tools in understanding fundamental principles of animal and robot locomotion. For example, the study of the "simplest walking model" by Kuo as presented in [10] describes walking with two rigid legs that are linked together at the hip and actuated through impulsive events at the feet. Impulsive actuation is applied to the hind foot exactly during the impact of the front foot during the step-to-step transition. In the non-impulsive phases of the gait cycle the system is purely passive and following its natural dynamics which is defined through its morphology and the surrounding environment. Two observations can be made from the simplest walking model. First, that the morphology of the walking system enables large portions of the gait to be uncontrolled to generate a stable interaction with the environment, and second, that impulses are the source of energetic changes. Using impulses to account for energetic changes might seem an unnecessary

introduction of non-smoothness in the system, and Kuo contrasted this actuation method by a spring-like hip torque actuation. Surprisingly, the investigation showed that the energetic cost of walking is only minimised when impulsive actuation is used and the spring-like hip torque actuation always generated a higher energetic cost.

It may be surprising that a disruption of the natural dynamics and an abrupt change of the system states can be energetically advantageous over other control inputs. A computational investigation of legged locomotion by Srinivasan and Ruina as presented in [11], however, supports this observation: the authors stated the problem of finding a controller for locomotion as an optimal control problem in a simple model, and asked which actuation, given a telescopic actuator, will minimise the energetic cost of transport of the system. Remarkably, the optimisation algorithm not only identified walking and running as energy minimising out of an infinite number of possible actuations and gaits, but also that the actuation to achieve these gaits is consistently converging to an *impulse*.

In this thesis we argue that the use of discrete actuation is the correct tool to model terrestrial legged locomotion. Besides revealing causal relationships between the complex interaction of morphology, control, and the environment, discrete actuation also appears to be the energy-optimal solution. One may argue that the use of discrete actuation is prone to produce non-smooth locomotion trajectories and jerky motions, but, surprisingly, we observe in our models a natural tendency to minimise the discontinuity and push the system towards a continuous output.

We argued earlier that the important aspect of *understanding* is a clear causality between action and effect. Discrete actuation can induce a discontinuous change in velocity in the system which qualitatively changes the behaviour. In the case of hopping locomotion, as studied in this thesis, the discrete actuation is directly resulting in a transition from stance to flight phase, two completely distinct dynamical states. The transition from flight to stance phase emerges through a collision of the body with the environment - another discrete event. As will become apparent in the subsequent chapters, the causality enables quantitative definitions of energetics for locomotion and the study of stability and control laws.

Discrete actuation is related to other fields that study and model complex systems. Simplest control inputs are converted through the complex system-environment interaction to desired behaviour, showing properties of *morphological computation* in the sense that morphology simplifies control. The function of the passive phase relies on the *self-stability* properties of the system which allows for disturbance rejection and locally attractive behaviour. Discretised actuation also relates to *central pattern generators*, when the impulse is generalised to an impulsive signal: a CPG is commonly excited by a constant signal which defines the motion of the underlying neuromechanical system. In discrete actuation,

such a behaviour is obtained when adding a dynamical element which integrates this signal and releases it to induce repetitive impulsive events, which maintain periodic behaviour without sensory feedback. Such an element could be an integrate-and-fire model - one of the oldest models to describe the behaviour of a neuron. In this broad sense, the discrete actuation system is interpreted as the effect of a central pattern generator. Discrete actuation furthermore relies on *self-organisation* and touches the field of *synergetics*, as the discrete inputs drive the system from an unordered state to an ordered one. As will be discussed in the subsequent chapters and Appendix C, for certain cases, self-organisation occurs for particular impulse properties that can be quantitatively defined. With these connections to complex systems in mind, the next section will present how locomotion dynamics of a system can be predicted using a model that uses the concept of discrete actuation.

1.1.1 The Process of Discretisation

The simplification of actuation input through discrete actuation necessarily outsources the complexity of dynamics to the morphology of the system. As actuation can only be applied at a finite number of instants in time, the mechanical (or neuromechanical) system needs to guarantee for a stable behaviour in the passive phases. There are no general design guidelines which allow for a systematic generation of morphology, but principles of self-stability come in handy for this task. The importance of morphology for the design of models with discrete actuation comes from the fact that it strongly influences the system-environment interactions. Hence, The shape of the foot is a main determinant of the locomotion behaviour. In this thesis, we will thus exclusively focus on the role of rigid foot shapes and their interaction with the environment. Not only is the effect of rigid shapes on stability easy to grasp, but they naturally fit in the framework of discrete actuation: interactions of rigid shapes can be modelled through collision mechanics, whose main focus is the study of discrete events. Collision mechanics also provides a simple way to dissipate energy which facilitates the study of energy effectiveness of locomotion, often disregarded in simple models like the basic spring-mass model [12].

The simplest walking model as presented by Kuo in [10] provides an example for a walking system with discrete actuation. We would like to generalise the process of discretisation of a locomotion system and we will do so by imposing model constraints as required by discrete actuation. Since the actuation is only allowed at few instants in time, the model's passive behaviour is crucial for the overall dynamics. As stated above, we will focus our attention on rigid shapes, which implies that the information of the required locomotion trajectory has to be stored in the shape of the model and the rule of interaction with the environment. Once the shape and environment interaction is defined, the control law needs

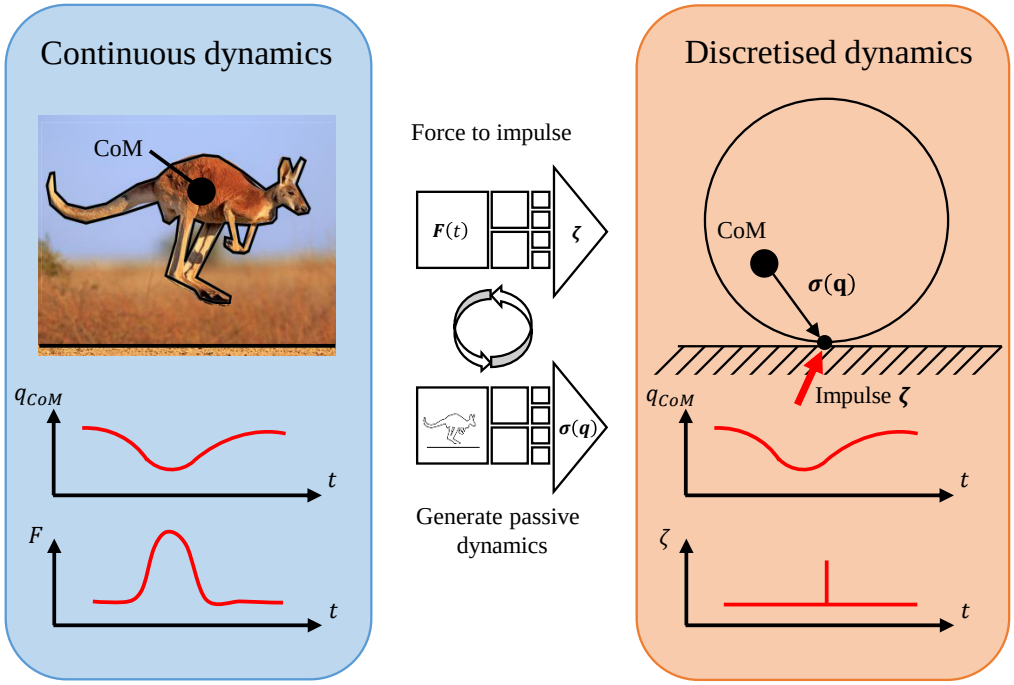

Fig. 1.1 **Discretised actuation**. The discretisation of the locomotion system is accomplished by finding a discrete actuation and a shape which can generate the original locomotion dynamics. Actuation is discretised by integrating the effect of the force $\boldsymbol{F}(t)$ and replacing it with an impulsive event with impulse $\boldsymbol{\zeta}$. The discretised shape ensures that the centre of mass (CoM) to contact point vector $\boldsymbol{\sigma}$ is predefined for every system state $\boldsymbol{q}$.

to be stated. This can either be open-loop, in which case the impulsive actuation is applied as a function of time, or closed-loop, where the impulsive actuation is applied as a function of state.

To clarify the process of discretisation we will demonstrate it for the case of hopping locomotion such as presented in Figure 1.1 for a kangaroo. The desired locomotion trajectory consists of a flight phase and a stance phase. While the flight phase is ballistic due to the passivity of our model, it is the stance phase that needs to be modelled carefully. We found that a cycloid, i.e. the trajectory of an eccentric point on a wheel rolling over a flat surface, mimics the trajectory of a hopping or running animal well depending on the radius of the wheel and its eccentricity. The stance phase trajectory is thus encoded in the shape of the body and the environment interaction rule, which are the eccentric wheel and rolling without slip, respectively. If we apply an impulsive actuation at the system-environment interaction, we find that a flight phase is induced which is followed by a ground collision and subsequent stance phase. Depending on the control mode (open- or closed-loop) and system parameters, the discretely actuated model will converge to a stable hopping behaviour. As will be discussed in detail in Chapter 3, this model robustly predicts locomotion characteristics of hopping robots and animals.

One important insight of our modelling approach is that hopping and running trajectories can be encoded in the rolling of a rigid shape. This adds a new hopping model that complements the commonly used spring-mass model for hopping and running locomotion. In the case of walking, rigid shapes have already been exploited in the passive dynamic walking models [13], which use a rigid leg that pivots around its ground contact point to mimic the walking stance phase.

Modelling is the standard tool to test causal relationships, and predictions to the original system can be tested given the obtained insights. In locomotion, models are extensively used and have been successfully employed to study animal motion and to develop design and control tools for robots. In the next section, the locomotion modelling approaches and insights are presented and put into context with the mentioned concepts. We focus mainly on terrestrial legged locomotion and present the main body of modelling literature in that field.

1.2 Modelling Terrestrial Locomotion

Finding cause and effect in a complex system is not trivial. What is the cause that makes animals energy effective in locomotion? What is the cause that makes them agile in natural environments? Models simplify the system and target specific domains of the original question to show causality. The most studied aspects of terrestrial locomotion are *morphology*,

actuation, and *control*. Focus is commonly placed on one of the three aspects to reveal causality, but a complete model requires to define all of them to a certain degree. For instance, actuation can only be studied given a control law and the effect of the actuation is a function of the morphology. Nevertheless, as the following three subsections will show, it is possible to highlight one aspect over another by appropriate model choice and technique.

1.2.1 Morphology

Morphology is the study of shape and body properties in the context of functional behaviour. In terrestrial locomotion, this includes mainly the form and shape of the structure which interacts with the environment and its compliant property. We will start with the latter aspect first, as one of the two important energy-saving mechanisms in legged animals is attributed to the compliance of legs, or, more precisely, the stiffness and its property to enable elastic energy storage. While one of the applications of stiffness in animals is to temporarily store kinetic energy during stance phase [14], it is also used to save energy in the leg-swing phase and in foot pads to prevent *chatter* [15]. It is observed that larger animals can be modelled with stiffer leg properties than small ones [16], and that the stiffness increases with running speed [17].

One of the most studied models in running and hopping locomotion for stiff leg morphology is the spring-mass model [12], [18]. It consists of a point mass which is attached to a massless spring that can interact with a rigid ground. The model was found to predict traits of human hopping and running remarkably well. Stability of this system has been studied in detail in the past [19], and it has also been used for walking to explain experimental observations which were not matched with more simplistic models [20]. It has also been used to model robot locomotion such as in [21].

Due to the success of the spring-mass system, many extensions have been developed to study different aspects of leg morphology. In [22], a model with two telescopic legs with springs is studied to explain observations in bipedal animals. A similar model was employed to test if there exists a passive limit cycle for the telescopic leg system [23]. The effect of segmented legs on stability of the spring-mass model is studied in [24], finding that stability regions are significantly increased in the segmented case. Spring-based modelling has not only facilitated the understanding of biological system, but also the development of hopping robots [25], [26], [27]. The model has further been used to model hexapedal locomotion as observed in insects [28]. Unconventional gaits like skipping are another topic which was studied with an extension of the spring-mass model [29].

Hopping and running robots are often based on the spring-mass analogy. The one-legged hopping robot by Raibert [30] can hop around in three dimensions, and the robot *ATRIAS*

[31] was designed to mimic the spring-mass model, with the goal to improve also energy economy of the system. The robot *Kenken* [32] mimics the behaviour of the hind limb of a dog and the authors find that one-legged planar hopping was possible with this design. A simpler design for human running with biarticular springs was used in [33]. The bow leg hopping robot [34] uses a curved beam to pre-load a spring and releasing it at the right time to induce hopping. Analogously, the authors in [35] employ a curved beam, but exploit the resonance frequency of the resulting spring-mass system to induce locomotion. When the right frequency is chosen, the authors find that the system can move in a hopping or bounding gait. The principles of this type of locomotion were studied and generalised in a rigid configuration in [36]. The system has further been extended and improved in terms of actuation [37], payload carrying capabilities [38], and high energy effectiveness [39].

Another aspect of morphology is the structure and shape of the body in contact with the environment. With the appropriate choice of body shape, an important phenomenon called *self-stability* can be observed in mechanical systems. As stated in their paper "Intelligence by mechanics" [8] the authors show how the mechanical design can *self-stabilise* locomotion, meaning that a system exhibits attractive behaviour on a desired state without actively sensing the disturbances. Ringrose shows in his paper [40] that a curved foot can contribute to a hopping robot's stability when designed with the appropriate radius for the system, to the extent that no sensory feedback is required for stable hopping. This self-stabilising effect was used in [41], where hopping in place is extended to forward hopping – still without any sensory feedback. A quick divergence to the control of juggling shows that indeed stabilisation can occur without the use of any sensors but just by the right choice of morphology [42], [43]. We will see in the next chapter how the morphology, and in particular the foot shape in combination with actuation, can improve several aspects of locomotion.

The principle of self-stability is deeply connected to the phenomenon called *passive dynamic walking*, which describes how walking-like gaits are possible without any control or actuator. The principle was introduced by McGeer and shows a system that can continuously and independently walk down a shallow slope [13], given the right initial conditions and morphology. Stability of these systems have been studied in detail, and can be reduced to a model which is regarded as the "simplest walking model" [44]. There are many physical robots which exploit properties of this model to exhibit walking, and there are theoretical models which are specifically created for these physical models [45]. Models which account for mass of the leg walk with a *compass-like gait* [46], [47]. Morphology and mass distribution of passive dynamic walking has indeed been explored in detail. The work in [48], [49] and [50] study the effect of kneed versus straight legged walkers and also contrast point feet to curved feet. The influence of foot shape on the collision loss is thereby emphasised.

As described in [49], a flat foot that exhibits heel and toe collisions is associated with less energetic losses, as already predicted by [51]. The effect of mass distribution in the passive dynamic walker on walking stability was studied in [52]. Passive dynamic walking has also been investigated for quadrupedal systems in [53]. Morphology has a significant influence on walking down a slope, but also on walking on non-inclined surfaces. In [54] and [55], the authors study the effect on foot shape in walking on level-ground, and show that curved feet provide energy saving mechanisms due to the reduced collision loss during the step-to-step transition. More complex models of level-ground walking extend the system to include knees and the trunk [56], or model the lateral motion [57].

Passive dynamic walking has not only been studied theoretically, but also in many experiments, first through the investigations of McGeer [13]. Passive dynamic walking robots initially had stiff legs such as in a toy walker that cannot stand still [58]. The shape of the foot has soon been identified as a crucial component to walk in three dimension with stiff legs, and this was exploited in the work of [59]. The authors in this paper also implemented the first kneed passive dynamic walkers. So far, the walkers were relying on the gravitational pull to walk down a shallow slope, but the extension to level-ground walking was soon achieved through robots such as in [60].

The idea of using morphology to perform or simplify control tasks is in the spirit of the philosophy of *morphological computation* [6], which states that the body is not just a means to execute action, but that the burden of control is offloaded–at least partially– to the morphology. The study of a soft silicone arm [61], for instance, showed how the nonlinearities of the soft structure can be used as a computational resource storing short term information. The use of smart morphology thus opens up new possibilities to simplify actuation and control laws and can help to establish a clear causality between the complex parts required for terrestrial locomotion.

1.2.2 Actuation

Wherever an actuator is placed in a robot, the possibility to exert forces and moments between adjacent bodies is possible. Forces enter the equations of motion as second-order terms, requiring integration to yield velocities and another integration to obtain positions. Causality of a force is hard to grasp, as it only induces a quantitative effect when acting over a period of time. Even a constant force can have complex effects in a dynamically system. One way to promote causality is to use *impulses* instead of forces.

Mathematically, an impulse is defined as the integral of a force over time, i.e. $\boldsymbol{p} = \int_{t_0}^{t_1} \boldsymbol{F}(t)dt$. It summarises the temporal effect of a force and defines a velocity change of a

body with given inertial properties. This restores causality at least on the velocity level, as an impulse applied at a point in time causes a well-defined velocity state, and the problem of integrating a differential equation over time is transformed to the problem of solving a mere algebraic equation. Forces which are well approximated with an impulse occur when the foot strikes the ground during walking and running, and they account to a large extent for the energetic costs of walking [62]. This impulse–being dissipative in its nature–is also called *impact*. The role of impact for bipedal locomotion was found to be crucial to achieve stable locomotion [63].

One of the simplest models to understand locomotion through an impulse-based model was presented in [51]. The studied locomotion system is reduced to a point mass and a massless leg, which showed that pseudo-elastic collisions are more energy effective than other types of collisions, irrespective of the presence of elastic elements. Furthermore, multiple collisions per stride length are also found to be more energy effective, which matches the observation of sequenced collisions in galloping horses. The same model has been applied to explain the differences in hopping of kangaroo rats and tammar wallabies, showing that kangaroo rats have only 69-71% the mechanical cost of transport of the wallaby for equivalent hopping velocities [64].

As introduced in Section 1.2.1, the passive dynamic walking model uses gravity as a source of actuation, but walking normally occurs on flat terrain. Even though there exist peculiar theoretical models which require no energy input to walk [65], this is never the case in a real system, which makes actuation an important aspect of theoretical modelling of locomotion on even ground. The energetic costs of level-ground walking are commonly ascribed to collisions during step-to-step transitions [66], [67]. The *inverted pendulum model* for walking thereby explains why the centre of mass position in human walking moves up and down instead of staying at the same vertical position [68]. Impulse-based modelling has not only been applied to describe passive impacts, but impulses have been used to model actuation forces. In [10], the author shows that toe-off impulses at the step-to-step transition can reduce the energetic cost of actuation as compared to a hip torque actuated system. The impulsive actuation was also described in [69] and [70], where the latter predicts the speed–step length relationship in human walking.

One of the most impressive walking robots based on impulsive actuation and that walks on flat ground is presented in [71]. The toe acts as the actuator as it exerts toe-off impulses to propel the robot forward. Not only did this robot remarkably demonstrate stable walking on level-ground, but it also achieved a world record in endurance walking in 2006[2].

[2]http://ruina.tam.cornell.edu/research/topics/locomotion_and_robotics/ranger/Ranger2011/

Impulse-based modelling is not confined to legged locomotion, but has been used in many other applications of biomechanics and engineering. For instance, in arboreal locomotion the brachiation of gibbons has been studied using collision-based models [72], [73]. Another example is juggling, which is characterised by repetitive collisions well modelled with impulses. The underlying principles of juggling are indeed closely related to hopping, as has been underscored in several publications [74], [75].

Robots that are designed to study the effect and benefit of impulsive actuation have shown to be highly useful in tasks like jumping and overcoming rough terrain. Designed for forward jumping, the robot *Grillo* can jump at 30 body lengths per second [76]. Similarly in [77], a small jumping robot is designed that can hop over 27 times its own size. The time to recharge the impulsive actuation unit is however too slow to continuously hop. The robot *Salto* [78] was built on a similar design, but improved in its capability to recharge in a short period of time. The authors show how this system can jump off the ground and redirect its legs to bounce off a wall immediately after. The cited systems exploit impulsive actuation for locomotion, but there exist systems which use impacts to alter their locomotion gaits. In [79], a hopping robot was designed capable of changing its foot shape, thereby controlling the impact behaviour of the robot. When the passive impacts were timed correctly, the locomotion speed of the system increased.

1.2.3 Control Laws

Given a morphology and an actuator, how do we decide on the actuation timings to achieve a desired behaviour of the overall system? Cause and effect become difficult to grasp and mathematical tools are being employed to design control laws which guarantee stability. As we will see, there are some genuine ideas which lead to an intuitive understanding of the resulting behaviour.

The mainstream approach in control synthesis of underactuated robotic systems is to solve an optimal control problem through computational methods. These models do not *a priori* depend on human intuition as they offload the task of modelling to an optimisation algorithm. The algorithm has the advantage of solving problems that are potentially high dimensional and not directly comprehensible for the human mind. The only objective is to either match experimental data, or minimises a defined quantity such as energy consumption. In a simple point mass model with telescopic legs, Srinivasan and Ruina [11] describe how such a computer optimisation with energy-optimality objective prefers walking at lower speeds and running at higher speeds. The results were later derived analytically through the minimisation of work [80]. The assumption that humans are using constrained optimisation to choose their walking speed and frequency has been suggested in [81]. A real life implementation of a robot

that is computationally optimising its locomotion capabilities is demonstrated by Tedrake in [82]. He uses a policy gradient reinforcement learning algorithm on a mechanical biped that is based on a passive dynamic walker. After one minute of learning, the robot is capable of moving forward, and after 20 minutes, it converges to the desired walking trajectory. Stochasticity has also been in the centre of attention of Byl and Tedrake's investigations [83]. It hypothesises that stochasticity needs to be taken into account in order to design control laws that perform well in real life situations. Walking modelled as a metastable process changes the optimal control policy. Another study which includes uncertainty in the model was presented in [84] where the authors use model predictive control for a compass-gait system to overcome uneven terrain. The theory of hybrid zero dynamics as presented in [85] uses a 5-link biped to show how zero dynamics can be used to synthesise an exponentially stable walking controller for an underactuated system.

Even though optimal control approaches can robustly generate control laws which work, the use of intuitive control laws still has an edge over optimal control approaches especially in dynamic locomotion tasks. Take for instance the hopping controller by Raibert [86]. The control strategy was first applied to 3D hopping monopods, and separates the hopping motion into three domains: height stabilisation, forward speed, and body attitude. Each law summarises a simple cause-and-effect relationship and turns out to work remarkably well on the actual system. The extension of the controller with the principle of virtual legs [87] expands the control method to the class of multi-legged robots. Another intriguing approach was proposed by [88]. The authors suggest to build a virtual frame made of springs and dampers around the robot which supports and prevents it from falling over. If the robot has actuation in some joints, a method is presented to map the forces induced by the virtual mechanical components to joint torques. The actuators can then be controlled by the calculated torques and the system will act as if the springs and dampers were actually there. This method can deal with complex control problems, but requires precise state feedback and actuation in order to map the virtual forces to the correct joint torques. One of the most prominent techniques to stabilise bipedal locomotion was introduced by Vukobratovic in the late 60's [89]. By calculating and measuring the centre of pressure on the foot, dynamic equilibrium conditions were derived, given the forces and moments that are acting on the foot ankle. Another intuitively derived feedback control method for the compass gait biped model is presented by Spong in [90]. Spong demonstrated that the potential energy could be shaped by a feedback control law that renders the equations of motion rotation invariant. This enabled the controlled compass gait biped to walk over different inclined surfaces.

The above examples emphasise that intuitive control laws work remarkably well for complex dynamical tasks. However, they depend on the fact that the system's state can be

measured and used to compute the actuator action. There exist control laws which do not rely on state feedback and use open-loop control such as in [91], [92], where actuation is sent to actuators by a predefined, clocked signal. These systems generally rely on self-stabilising properties of the robot, where the clocked actuation merely injects energy to the system with a predefined rate in time. Although simple conceptually, such robots can exhibit remarkable feats such as the robot *RHex* [93] which impresses with its robust locomotion over rough terrain. It uses six elastic curved beams that rotate in synchrony and with an open-loop control law. The system exploits the self-stabilising properties of the spring-mass model, for which evidence in this robot has been presented in [94]. Another study shows how quadrupedal bounding can emerge through a simple sinusoidal open-loop locomotion controller in a quadruped [95].

These examples hint towards the fact that complexity of the control law can be reduced by designing an appropriate body. Based on this philosophy, Taga showed in his seminal paper [5] how an appropriate neuromechanical design of the body can lead to stable locomotion which can switch from walking to running and back by a simple change in control gain. The term *global entrainment* thereby captures the idea of synchronisation of the interacting nonlinear elements in the system, through which a meaningful behaviour emerges. Evidence of such mechanisms in animals was suggested with so-called central pattern generators (CPGs) [96], where locomotion emerges as an interaction of self-sustained neural oscillations that are influenced through feedback loops from the environment and neighboring oscillators. CPGs have been extensively used in robotics [97], notably the study of central pattern generators in a salamander-like robot due to Ijspeert et al. [98] showed how walking and swimming are induced through a mere change in oscillator gain factor. Oscillation in a CPG is self-sufficient, meaning that it needs no external sensory input. On the other side of the spectrum are models which have no internal clock or pattern generators, but which are purley reflex based. In [99], the authors show how walking locomotion can emerge through reflex-based control and the interaction of the mechanical system with the environment in a human model.

Reflex-based control, CPGs, and self-stability share the property of self-organisation, which states that order can arise through interaction of the system's parts from an initially disordered state. Haken [7] introduces the field of *synergetics* which studies the conditions under which systems undergo self-organisation. The open-loop, CPG, and reflex based control laws exploit this concept and the idea is related to discrete actuation which will be introduced in Section 1.1.

1.2.4 Other Modelling Aspects

The previous sections have introduced the bottom-up approach of modelling for terrestrial locomotion, but causality can also be established on a general level using statistical tools. This section aims as an extension of these and other modelling methods and will be revisited in some of the chapters of this thesis.

One example is the use of empirical power laws which are often used in biology. In [100], the authors describe the energetic cost of locomotion as a power law, depending on body mass. This modelling technique has also been used in [101] to predict the locomotion speed of dinosaurs, based on data of living animals, and [102] for the case of fast running insects.

Locomotion has been studied on a most fundamental basis in terms of the physical conditions under which the system operates. If walking is assumed to be accurately described with the inverted pendulum analogy, there is a limit at which the system can travel due to the unilateral ground constraint. Assume the system moves at velocity v and the leg length be r, then the acceleration due to the centripetal force of the inverted pendulum is v^2/r. If this value exceeds the gravitational acceleration g, i.e. $v^2/r > g$, then the leg would lift off the ground. Applying this method to a human adult in an inverted pendulum model, we find that the maximal walking speed is around $3ms^{-1}$, roughly corresponding to the observed gait transitions to running. This method of analysis has not only been employed for walking and running [103], [104], but also for jumping [105].

Some models specialise only on aspects of the locomotion gait, such as in [106] and [107] where the swing phase during walking is analysed. The authors argue that walking requires energy to establish the initial conditions for stance phase, and the rest of the cycle is purely "ballistic", i.e. only influenced by gravity.

1.3 Objectives

This thesis argues that, through the discretisation of actuation, the basic principles of dynamic locomotion can be understood and explored. The argument is supported by the subsequent thesis chapters where the *discretised actuation* is studied for the case of hopping locomotion. Among other things, the benefit of this approach is brought forward for the prediction of locomotion trajectories, the understanding of self-stabilising and energetic principles, actuation, and control in real-world robots. The implications and benefits of the theory will be analysed theoretically in a model, computationally in simulation, and physically in robot implementations. The following three objectives state the specific targets to be achieved with this work.

O1 **Mathematical formulation of locomotion with discretised actuation**. To develop a mathematical framework for discretised actuation. This thesis focuses predominantly on hopping locomotion in animals and robots.

O2 **Implications of discretised actuation**. To study the implications of the results derived from the mathematical model. Insights for energy effectiveness, stability, and control of hopping locomotion are of primary interest.

O3 **Robot implementation of discretised actuation**. To approximate discretised modelling in robots. This involves primarily to find real-world representations of impulses and impulsive actuation, such that the theoretical concept of impulses can be used in real systems.

Objective **O1** will be addressed in the beginning of Chapter 3, Chapter 5 and Appendix C. The mathematical tools of discretised actuation are then applied to tackle Objective **O2** in Chapter 3 and Chapter 4. Real-world implementations of discretised actuation as required by Objective **O3** are developed in Chapter 5 and Chapter 6. The outcome of the presented work with respect to the objectives and the impact will be discussed in the conclusion in Chapter 7. The concrete contributions as a result of the broad objectives stated here, are summarised next.

1.4 Contributions

As has been discussed previously, this work aims to study the merit of discretised actuation to improve our understanding of complex systems by establishing clear causality between actuation and its effect on dynamics. Based on the case of terrestrial legged locomotion we provide contributions to theoretical modelling, the understanding of locomotion physics, robot actuation and control, and self-organisation in a complex system. The following subsections will provide a more detailed picture of the contributions of this thesis and the fields they relate to.

1.4.1 Physics of Locomotion

The idea of using impulses and rigid shapes to model legged locomotion has been successfully used in the past to model human and animal locomotion (see Section 1.2.2), but is commonly studied in the context of impulses which induce a velocity change only in the translational components of the system. In Chapter 3, we show that the effect of an impulse on the rotational degree of freedom can result in perpetual forward hopping locomotion. The simple

model was used to predict robot and animal locomotion properties, and helps add a novel modelling approach to the field of locomotion.

A thorough analysis of the impulsive model reveals that physical effects give rise to stable locomotion. More precisely, the effect of an impulse is sensitive to the mass distribution in the system, opening up the possibility to alter the dynamics by changing the mass distribution. We show in Chapter 4 and Appendix A how these effects arise and how they contribute to locomotion energetics and behaviour. The analysis further allows for an analytic energy comparison between different locomotion strategies in terrain with obstacles, which we use to find advantages of hopping over rolling locomotion. The results show that hopping is energetically advantageous for higher Froude numbers, rolling is preferred for lower ones. This analysis reveals the importance of swing-leg retraction, moment of inertia in locomotion, and addresses the question why there are only few rolling gaits found in nature.

1.4.2 Locomotion Actuation and Control

The implementation of impulse-like events for actuation purposes in robots poses a challenge due to multiple reasons. Most importantly, impulsive actuation mechanisms commonly need to charge and store energy, which is reflected in the gradual change in one of the system states. For instance, the use of a flywheel to induce a rotational impulse requires to increase kinetic energy, which is reflected in the angular velocity state of the flywheel. The charging process is often temporally expensive and is accompanied by parasitic effects, e.g. the charging of the flywheel creates a torque. Rather than preventing this effect, we built the robot *Robbit* as presented in Chapter 5 to take advantage of it. The mechanism uses the induced torque to accelerate during stance phase, and the subsequent impulses is used to induce the flight phase, resulting in a forward hopping motion. The exploitation of such effects shows how robots can be designed to work with their natural dynamics instead of forcing an unnatural behaviour, which relates to the ideology of passive dynamics, decentralised control, and self-stability.

Another naturally occurring effect in locomotion are inelastic impacts due to the robot-environment interaction. Impacts are commonly considered to hamper the locomotion performance due to their energy-dissipating effect. However, impacts can alter the dynamics in a way which most actuators can't in that they change the system velocity in an instant. Though energy is being lost, the latter may be beneficial in tasks where directionality is important for performance of the system, which is the case in the task of locomotion. To study the potential benefit of impacts, we built the robot *CaneBot* as presented in Chapter 6 which can alter its foot shape and can thus induce impacts at desired instants in time. We found that for certain control schemes of the induced impact, the resulting locomotion speed

is increased by up to 40% as compared to locomotion without artificially induced impacts. The results suggest that, although lossy, impacts can defy intuition and increase locomotion performance, which opens up new paradigms and methods for control of legged robots.

1.4.3 Self-Organisation

The emergence of organised behaviour in an initially disorganised state is often observed in complex systems and appears to be an important and recurring process in nature. We study this self-organisation in our case of discrete locomotion actuation, where repetitive impulses are applied to the system that drive the initially resting robot to a steady and stable locomotion behaviour. The emergence of this phenomenon can be attributed to the intricate interaction of the impulse with the mechanical shape of the robot and the environment. The shape or body thereby contributes distinctly to the successful motion of the robot, which relates to the field of morphological computation. In Chapter 5 we show the effect of strictly convex foot shapes on the locomotion performance, clearly indicating its influence on the quantitative locomotion dynamics, but also showing that a wide range of morphologies lead to the same qualitative behaviour. The thesis thus contributes to the study of morphology and suggests quantifiable ways to determine when self-organisation can occur.

The process of self-organisation is difficult to comprehend, as an analytic expression of the dynamics is often not possible and prevents the definition and assignment of cause and effect. In some simplest cases, however, the nonlinear equations can provide great insights into the underlying mechanisms of self-organisation. In Appendix C, we show how our impulsive model can be simplified such that analysis of stability becomes analytically tractable. The results show that impulses can lead to stable locomotion if they are chosen in a given range of magnitude and open-loop control frequency. The study presents a simplest model that displays the power of self-stability and defines concrete design choices to achieve such a behaviour. The model provides a tool and approach to study emergence of self-organisation through the study of stability, and adds an analytically tractable example that can be used for educational purposes in courses on nonlinear dynamics and underactuated control.

1.5 Structure of Dissertation

After having introduced the concept of discretised actuation and the main body of literature related to the topic, this chapter is followed by an introductory chapter to rigid body contact dynamics and four case studies where the concept is applied to model the case of hopping

locomotion, to understand the energetics of overcoming obstacles through hopping, to build a robotic system that uses discretised actuation for locomotion, and to exploit passive impacts to improve locomotion dynamics in a robotic system.

Chapter 2 summarises the required theory of planar rigid body contact dynamics for the subsequent technical chapters. While we tried to make the technical chapters self-contained, this chapter is intended to provide an extension and reference to the used methods.

Chapter 3 presents the impulsive eccentric wheel model, which uses discretised actuation to model hopping locomotion of robots and hopping animals. The theory of the model will be explained in detail and will be used to model locomotion trajectories of real-world systems.

Chapter 4 presents the use of discretised actuation to understand the energetics of hopping and rolling in terrain with obstacles. After explaining the detailed model and considered locomotion strategies, theoretical results are presented which give a quantitative rule at which hopping outperforms rolling for given locomotion characteristics. The results are applied to mimic hopping and running animals to see how hopping compares to rolling for animal-related parameters. The results of the theoretical predictions are largely verified in an experimental test platform and are presented in detail.

In Chapter 5, the discretised actuation approach is implemented in a real-life robot to test its power to improve performance of impulse-actuated robots. The concept of rotational impulses is therefore introduced and stability considerations of the design are discussed in theory and simulation. The concept and design of the hopping robot *Robbit* is then presented followed by the experimental conditions and results.

Chapter 6 studies the effect of discrete foot shape changes on the hopping performance in the hopping robot *CaneBot*. The chapter discusses the timing of impacts which are induced through the shape change. Though dissipative in its nature, the impacts can increase locomotion speed when applied at the right time during the gait cycle. Experimental results are shown and analysed using a quantitative discretised model to understand the observations.

Chapter 7 discusses the impact of the presented work and puts the results of the individual chapters in the framework of discrete actuation. The concept of discrete actuation opens up several paths and ideas for future work, which are also presented in that chapter.

Chapter 2

Planar Rigid Body Contact Dynamics

This thesis studies the role of discrete actuation in locomotion systems operating in a terrestrial environment. To appreciate the effects of discrete actuation on locomotion performance such as cost of transport and stability, we want to use theoretical models that can quantitatively define such a performance metric. Here we argue that rigid body contact dynamics is an adequate framework to this end, as it not only allows to efficiently predict the motion of multibody systems, but also for an energetic assessment of the locomotion performance. Take for instance the bouncing ball as discussed in the last chapter: rigid body contact dynamics allows for the prediction of the continuous flight phase, can compute the impulsive velocity change at paddle collision, and define the energetic loss that occurred during the collision. We thus have a powerful tool with which we can compare discretely actuated systems quantitatively.

This chapter will introduce the basic equations of contact dynamics as required for this thesis. Wherever possible, we will make use of simple impact laws without modelling friction, as the resulting equations offer a clearer insight into the basic energetic principles of the studied systems. However, where an accurate description of the system dynamics is preferred over the lucidity of the dynamics, we will model collisions with unilateral impact laws and Coulomb friction. We tried to keep the technical chapters of this thesis as self-contained as possible and added this chapter mostly to offer a consistent description and reference of the contact dynamics, and to extend the mathematical details of the used methods.

One word of caution has to be said about contact dynamics. The combination of rigid body dynamics with geometric and kinematic constraints can lead to inconsistencies in the predicted system energies, which is why the model parameters have to be chosen carefully. In particular, it was shown that the combination of impact laws and friction laws can lead to an increase in the total system energy over a dissipative collision, which is obviously a physically erroneous solution. However, the error depends on the chosen restitution laws

at collision, and it was shown that energetic consistency in Newtonian kinematic impact laws coupled with Coulomb friction is guaranteed if all coefficients of restitution are close to zero [108]. In this thesis, we will use a completely inelastic impact law, which implies that the coefficients of restitutions are equal to zero and thus consistency is given in all the subsequent models.

This chapter is structured as follows. Section 2.1 defines basic rigid body kinematics required for the subsequent sections, which is followed by the procedure to define constrained rigid body dynamics in Section 2.2. Section 2.3 presents the impact equations for a single rigid body colliding with a static environment. The methods to include discrete impulsive actuation in the equations of motion are presented in Section 2.4. Finally, Section 2.5 presents the multi-contact dynamics model with impacts and friction.

2.1 Planar Rigid Body Kinematics

The state of a rigid multibody system is described by the generalised coordinates $\boldsymbol{q}(t)$ and its derivative $\dot{\boldsymbol{q}}(t) = \boldsymbol{u}(t)$. We will omit the notation of the independent variable t from now on for convenience. We will only consider the planar case, which means that every rigid body has three degrees of freedom with respect to an inertial frame of reference, for instance horizontal position, vertical position and angular position. For a single rigid body this would imply the generalised coordinates

$$\boldsymbol{q} = [x, y, \phi]^T \tag{2.1}$$

and the generalised velocity

$$\boldsymbol{u} = [\dot{x}, \dot{y}, \dot{\phi}]^T, \tag{2.2}$$

where x is the horizontal displacement with respect to the inertial frame of reference, y is the vertical displacement with respect to the inertial frame of reference, and ϕ is the angular position with respect to the inertial frame of reference. Figure 2.1 shows the case of an eccentric disc where x and y point to the position of the centre of mass of the body and ϕ indicates the rotation of the eccentric disc. The inertial frame of reference has unit vectors $\boldsymbol{e}_x$, $\boldsymbol{e}_y$, and $\boldsymbol{e}_\phi$

One important kinematic measure for collision dynamics is the gap function $g_N(\boldsymbol{q})$ which measures the closest distance between the environment and any potential contact point on the rigid body. For the eccentric disc as illustrated in Figure 2.1, the gap function is

$$g_N(\mathbf{q}) = y + a\cos(\phi) - R, \tag{2.3}$$

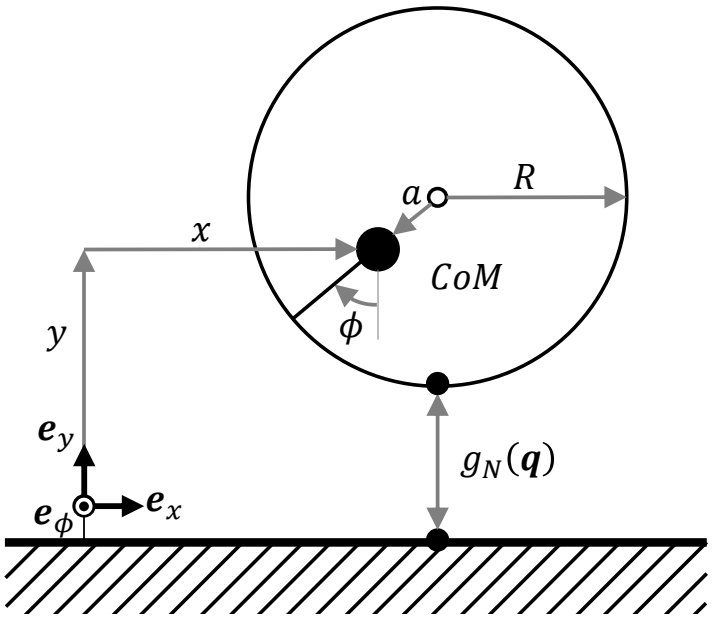

Fig. 2.1 Sketch of planar rigid disc with radius R, eccentricity a, and generalised coordinates $\boldsymbol{q}$ with respect to an inertial frame of reference. x and y point to the centre of mass CoM of the rigid body. $g_N(\boldsymbol{q})$ is the gap function and indicates the smallest distance between the environment and any potential contact point on the rigid body.

with R the radius and a the eccentricity of the eccentric disc.

In case of collision, an important measure is the relative velocity between the approaching rigid bodies. In the case of a static environment, the relative velocity of contact point c is defined as

$$\boldsymbol{\gamma} = \mathbf{J}_c \boldsymbol{u}, \tag{2.4}$$

where $\mathbf{J}_c = [\boldsymbol{w}_T^T; \boldsymbol{w}_N^T]$ is a matrix consisting of the tangential and normal generalised contact force direction $\boldsymbol{w}_T$ and $\boldsymbol{w}_N$, respectively. We will refer to $\mathbf{J}_c$ as contact Jacobain. For the case of the eccentric disc colliding with a flat static environment, the contact Jacobian is

$$\mathbf{J}_c = \begin{bmatrix} 1 & 0 & R - a\cos\phi \\ 0 & 1 & -a\sin\phi \end{bmatrix}, \tag{2.5}$$

The generalised force directions in this example are thus

$$\boldsymbol{w}_T = \begin{bmatrix} 1 & 0 & R - a\cos\phi \end{bmatrix}^T, \tag{2.6}$$

and

$$\boldsymbol{w}_N = \begin{bmatrix} 0 & 1 & -a\sin\phi \end{bmatrix}^T. \tag{2.7}$$

The generalised force directions define how a planar force $\boldsymbol{F}$ enters the equations of motion. The transformation of the planar force $\bar{\boldsymbol{F}}$ acting on the contact point to the generalised force $\tilde{\boldsymbol{F}}$ is done using the contact Jacobian, i.e. $\tilde{\boldsymbol{F}} = \mathbf{J}_c^T \boldsymbol{F}$.

2.2 Constrained Rigid Body Dynamics

The unconstrained equations of motion of the generalised coordinates are defined by

$$\mathbf{M}\dot{\boldsymbol{u}} - \boldsymbol{h}(\boldsymbol{q}, \boldsymbol{u}, t) = \mathbf{0}, \tag{2.8}$$

where $\mathbf{M}$ is the mass matrix, and $\boldsymbol{h}$ is the vector of external forces and gyroscopic accelerations. We would like to impose geometric and kinematic constraints on the system without having to redefine it. This can be done by first defining the constraints on position or velocity level and then take their derivatives such that they are defined on acceleration level. We can then use Gauss' principle to enforce the constraints via Lagrange multipliers in the equations of motion. The Lagrange multipliers then have the interpretation of the forces which are required for the constraints to hold in the equations of motion.

Without loss of generality, we will use this method to enforce a rolling constraint of the eccentric disc in Figure 2.1. The constraint on position level is a geometric property as a function of the generalised coordinates which has to be equal to zero, e.g. in the case of the eccentric disc

$$\boldsymbol{g}(\boldsymbol{q}) = \begin{pmatrix} x - a\sin\phi + R\phi \\ y + a\cos\phi - R \end{pmatrix} = \mathbf{0}. \tag{2.9}$$

Note that the second entry of this constraint is equal to the gap function $g_N(\boldsymbol{q})$, which implies that no penetration of the ground is allowed. The first entry states that the disc rolls over the ground without slip. This definition of ground constraint will later on lead to dynamics without friction as the no-slip condition will be enforced regardless of whether the forces can physically be generated by the ground or not. The derivative of the geometric constraint is

$$\dot{\boldsymbol{g}}(\boldsymbol{q}, \dot{\boldsymbol{q}}) = \begin{pmatrix} \dot{x} - a\dot{\phi}\cos\phi + R \\ \dot{y} - a\dot{\phi}\sin\phi \end{pmatrix} = \mathbf{J}_c \boldsymbol{u} = \mathbf{0}. \tag{2.10}$$

We see that $\dot{\boldsymbol{g}} = \boldsymbol{\gamma}$ from Equation (2.4). Finally we obtain on acceleration level

$$\ddot{\boldsymbol{g}}(\boldsymbol{q}, \dot{\boldsymbol{q}}, \ddot{\boldsymbol{q}}) = \begin{pmatrix} \ddot{x} - a\ddot{\phi}\cos\phi + a\dot{\phi}^2\sin\phi \\ \ddot{y} - a\ddot{\phi}\sin\phi - a\dot{\phi}^2\cos\phi \end{pmatrix} = \mathbf{J}_c\dot{\boldsymbol{u}} + \boldsymbol{\xi} = \mathbf{0}, \tag{2.11}$$

where we summarise all terms that do not depend on a second derivative in the vector $\boldsymbol{\xi}$. Next, we define the dynamics of the constrained system by

$$\mathbf{M}\dot{\boldsymbol{u}} - \boldsymbol{h}(\boldsymbol{q},\boldsymbol{u},t) = \tilde{\boldsymbol{F}}_c \tag{2.12}$$

where we have added the generalised vector $\tilde{\boldsymbol{F}}_c$ that represents the forces that enforce the kinematic constraint. As already indicated in the last section, the transformation of a planar force to a generalised force is accomplished using the contact Jacobian and we hence obtain

$$\mathbf{M}\dot{\boldsymbol{u}} - \boldsymbol{h}(\boldsymbol{q},\boldsymbol{u},t) = \mathbf{J}_c^T\boldsymbol{\lambda} \tag{2.13}$$

where $\boldsymbol{\lambda}$ is now the Lagrange multiplier which enforces the constraint, or in this case the planar contact force at ground contact. Equations (2.11) and (2.13) combined give an expression for the ground contact force $\boldsymbol{\lambda}$

$$\boldsymbol{\lambda} = -\left(\mathbf{J}_c\mathbf{M}^{-1}\mathbf{J}_c^T\right)^{-1}\left(\mathbf{J}_c\mathbf{M}^{-1}\boldsymbol{h}+\boldsymbol{\xi}\right). \tag{2.14}$$

Substitution of (2.14) into (2.13) leads to the constrained equations of motion of the system.

The resulting equations will enforce the rolling constraint, and they will do so irrespective of the magnitude of the required ground contact forces. This means that it would render a bad model for a system which is largely influenced by friction, as slip can not occur. Furthermore, it is a bilateral constraint, meaning that the ground contact will pull the system down in the case of detachment and force it to stay on the ground. This is not a physically correct behaviour in terrestrial locomotion systems, as the ground can in general only create repelling reaction forces, not attracting ones. Section 2.5 will present a method that allows for unilateral constraints, which resolves the problem. Despite the shortcoming of the bilateral constrained equations of motion as presented in this section, we have used them in several instances in this thesis due to their simplicity and transparency. To avoid errors of an attracting ground reaction force in these cases, we have monitored the ground reaction forces at all times to assure that our model is operating in a valid range.

2.3 Inelastic One-Contact Collision without Friction

The transition between unconstrained and constrained dynamics is often not smooth, meaning that system states have to jump in order to comply with the constrained dynamics. This transition is achieved through the impact equations. In this section, we only consider inelastic one-contact collisions without friction, which can be used, for instance, in the case of the

eccentric disc as it transitions from a gap function $g_N > 0$ to $g_N = 0$ where the dynamics are governed by the unconstrained and constrained equations, respectively. The impact equations of a contact c with a static environment are

$$\mathbf{M}(\boldsymbol{u}^+ - \boldsymbol{u}^-) = \mathbf{J}_c^T \boldsymbol{\Lambda}, \tag{2.15}$$

with $\mathbf{M}$ the mass matrix, $\boldsymbol{u}^+$ the post-impact generalised velocity, $\boldsymbol{u}^-$ the pre-impact generalised velocity, $\mathbf{J}_c$ the contact Jacobian as defined in Section 2.1, and $\boldsymbol{\Lambda}$ the impulse transferred at collision.

Next, an impact law needs to be defined. In this thesis we exclusively use inelastic impact laws as they capture the contact dynamics in real terrestrial locomotion systems well. In addition, this avoids problems with energetic consistency during the collisional event [108]. The inelastic impact law is a kinematic law and hence defined on velocity level. It states that the post-collision velocity of the contact point is equal to zero, in other words

$$\boldsymbol{\gamma}^+ = \mathbf{J}_c \boldsymbol{u}^+ = \mathbf{0}. \tag{2.16}$$

Combining Equations (2.15) and (2.16) we get

$$\mathbf{J}_c \boldsymbol{u}^+ = \mathbf{J}_c \mathbf{M}^- 1 \mathbf{J}_c^T \boldsymbol{\Lambda} + \mathbf{J}_c \boldsymbol{u}^- = \mathbf{0}, \tag{2.17}$$

which we can solve for the transferred impulse during collision

$$\boldsymbol{\Lambda} = -\left(\mathbf{J}_c \mathbf{M}^- 1 \mathbf{J}_c^T\right)^{-1} \mathbf{J}_c \boldsymbol{u}^-. \tag{2.18}$$

Using this definition of transferred impulse and inserting it in Equation (2.15) leads to the post-collision generalised velocity

$$\boldsymbol{u}^+ = \left(\mathbf{I} - \mathbf{M}^{-1} \mathbf{J}_c^T \left(\mathbf{J}_c \mathbf{M}^{-1} \mathbf{J}_c^T\right)^{-1} \mathbf{J}_c\right) \boldsymbol{u}^-. \tag{2.19}$$

This equation relates the pre-impact generalised velocity to the post-impact generalised velocity. It is valid in a multibody system for one-contact collisions with inelastic coefficient of restitution and no friction. We will make extensive use of this equation to model the system-environment interaction of our discretely actuated systems.

Another quantity we will exploit is what we call the *collision matrix* $\mathbf{M}_c$ defined as

$$\mathbf{M}_c = -\mathbf{J}_c^T \left(\mathbf{J}_c \mathbf{M}^{-1} \mathbf{J}_c^T\right)^{-1} \mathbf{J}_c. \tag{2.20}$$

The collision matrix is a useful tool to study energetics of an inelastic collision, as it provides the dissipated energy during collision when used in the quadratic form

$$\Delta E = \frac{1}{2}(\boldsymbol{u}^-)^T \mathbf{M}_c \boldsymbol{u}^-, \tag{2.21}$$

which can easily be shown to hold when subtracting the post-collision energy from the pre-collision energy.

2.4 Impulsive Actuation

Impulses are induced in collision dynamics to account for the collisional system-environment interactions, but they can also be imposed on the system dynamics as an impulsive actuation which changes the system velocities in an instant. The computation of the post-actuation velocities is analogous to the case of inelastic one-contact collisions without friction as presented in the last section. Assume we are applying a planar impulse $\boldsymbol{\zeta}$ at a point i to our system. The post-actuation velocity is

$$\boldsymbol{u}^+ = \mathbf{M}^{-1}\mathbf{J}_i^T \boldsymbol{\zeta} + \boldsymbol{u}^-, \tag{2.22}$$

where $\mathbf{J}_i$ is the Jacobian at the point of attack of the impulse. This equation assumes that the impulse can be transferred without any restrictions to the system velocities at point i. In real systems this won't always be possible as for instance the transmission of the impulse might be restricted due to the effects of friction. For such cases we will use a more detailed model that includes frictional impulses as will be presented in the next section. In Chapter 5 we will use rotational impulses instead of translational ones, in which case the Jacobian in Equation (2.22) will be the rotational Jacobian for the body at which the impulse is applied.

2.5 Multi-Contact Collision with Friction

In the case where multiple contacts are closed at the same time, the previously presented methods can't be used as they may result in solutions which are physically implausible. For example, if two instead of one contacts close on a single rigid body, the system would instantly come to a rest after collision as this is the only solution when the methods presented in Section 2.3 are used. The sudden halt is not what we would observe in a real physical system. Rather, one or both of the contacts will open over the impact. We mostly avoid multi-contact problems in this thesis as we would like to focus on using the more transparent

methods presented so far. For certain cases, however, it makes sense to use a multi-contact formulation, especially because the effects of friction can be elegantly included in it to form a more realistic model.

We will use the modelling method as presented by Glocker and Studer [109] which is based on an LCP (linear complementarity problem) formulation of the contact dynamics and which will be elaborated in the next few subsections. This method will lead to physically accurate collision dynamics while also considering the limitations of force transmission due to friction. First, the set-valued functions are introduced which will be used to express the unilateral impact and friction laws.

2.5.1 Set-Valued Functions

Instead of assigning a one-to-one correspondence of an element in the codomain to an element in the domain of a function, a set-valued function can assign sets to an element in the domain. The two set-valued functions we will need are the unilateral primitive (Upr) and the set-valued signum function (Sgn), not to be confused with the sign function (sgn) which is zero for sgn(0). The functions are defined as

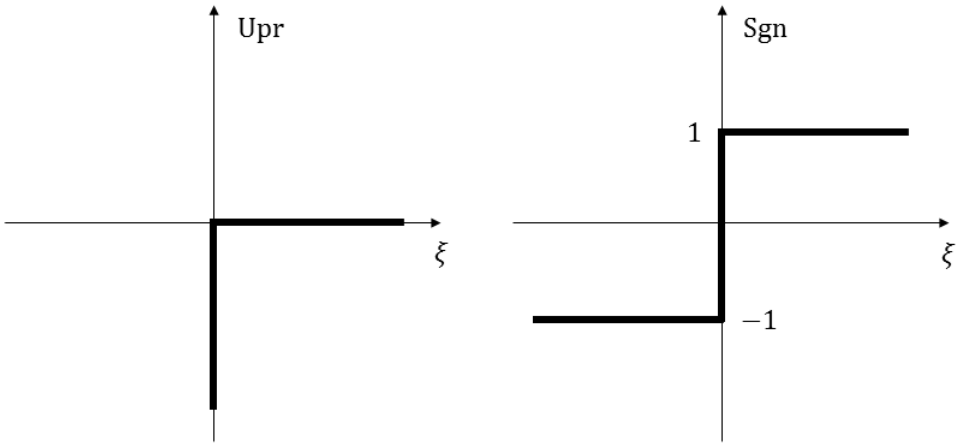

Fig. 2.2 Unilateral primitive (Upr) and set-valued relay function (Sgn).

$$\mathrm{Upr}(\xi) = \begin{cases} (-\infty, 0] & \text{if } \xi = 0 \\ 0 & \text{if } \xi > 0 \end{cases}, \tag{2.23}$$

and

$$\mathrm{Sgn}(\xi) = \begin{cases} -1 & \text{if } \xi < 0 \\ [-1, 1] & \text{if } \xi = 0 \\ 1 & \text{if } \xi > 0 \end{cases}. \tag{2.24}$$

These two functions, for which their graph is depicted in Figure 2.2, will be used to define the kinematic laws for hard contact and friction. The Upr function has the property that it is set-valued at Upr(0) between $-\infty$ and 0, and is 0 for positive values. The Sgn function is -1 for negative values, 1 for positive values, and set-valued between -1 and 1 for Sgn(0).

2.5.2 The Linear Complementarity Problem

In a multi-contact problem with frictional impulsive events and unilateral constraints, contacts can be open or close and in the state of sticking or slipping. An impulsive event can cause a transition from one state to another in the set of closed contacts, which poses a combinatorial problem. It turns out that this combinatorial problem can be stated as a linear complementarity problem (LCP). An LCP is defined as follows. Given a linear system of equations

$$\boldsymbol{y} = \mathbf{A}\boldsymbol{x} + \boldsymbol{b} \tag{2.25}$$

with the conditions

$$\boldsymbol{y} \geq \mathbf{0}, \qquad \boldsymbol{x} \geq \mathbf{0}, \qquad \boldsymbol{y}^T\boldsymbol{x} = 0, \tag{2.26}$$

where $\mathbf{A} \in \mathbb{R}^{n\times n}$ and $\mathbf{b} \in \mathbb{R}^{n\times 1}$, find $\boldsymbol{x} \in \mathbb{R}^{n\times 1}$ and $\boldsymbol{y} \in \mathbb{R}^{n\times 1}$. Defining $\mathbf{E} := (\boldsymbol{e}_1, ..., \boldsymbol{e}_n)$ the identity matrix and $\mathbf{A} := (\boldsymbol{a}_1, ..., \boldsymbol{a}_n)$, the LCP can be rewritten as

$$(\boldsymbol{e}_1, ..., \boldsymbol{e}_n, -\boldsymbol{a}_1, ..., -\boldsymbol{a}_n) \begin{pmatrix} \boldsymbol{y} \\ \boldsymbol{x} \end{pmatrix} = \boldsymbol{b}, \tag{2.27}$$

$$y_i \geq 0, \qquad x_i \geq 0, \qquad y_i x_i = 0 \quad \forall i = (1, ..., n)\,. \tag{2.28}$$

Now be $\boldsymbol{c}_i \in \{\boldsymbol{e}_i, -\boldsymbol{a}_i\}$ the i-th complementary pair of vectors, and $z_i \in \{\boldsymbol{y}_i, \boldsymbol{x}_i\}$ the i-th complementary pair of variables such that

$$z_i = \begin{cases} y_i & \text{if } \boldsymbol{c}_i = \boldsymbol{e}_i \\ x_i & \text{if } \boldsymbol{c}_i = -\boldsymbol{a}_i \end{cases}. \tag{2.29}$$

There are 2^n possible matrix-vector combinations $\mathbf{C}_k := (\boldsymbol{c}_1, ..., \mathbf{c}_n)$ and $\boldsymbol{Z}_k := (z_1, ..., z_n)^T$ which can potentially solve $\mathbf{C}_k\boldsymbol{Z}_k = b$. As n will increase with increasing number of closed contacts, the solution of the LCP will become more difficult to find the more contacts are involved in the collision dynamics.

2.5.3 The Multi-Contact LCP with Friction and Impacts

The derivation of the LCP for the multi-contact problem with friction is done in detail in Glocker's work [109], and we will only mention the basic concepts and main results in this section.

An elegant way to combine the impact-free motion (2.8) with the impact equations (2.15) is by using measure differential inclusions [110]. Say there are currently n contacts closed, then the measure differential inclusion reads

$$\mathbf{M}\mathrm{d}\boldsymbol{u} - \boldsymbol{h}\mathrm{d}t - \sum_{i=1}^{n} \mathbf{J}_i \mathrm{d}\boldsymbol{\Lambda}_i = 0 \tag{2.30}$$

where $\mathrm{d}\boldsymbol{u} = \dot{\boldsymbol{u}}\mathrm{d}t + (\boldsymbol{u}^+ - \boldsymbol{u}^-)\mathrm{d}\eta$ and $\mathrm{d}\boldsymbol{\Lambda}_i = \dot{\boldsymbol{\lambda}}_i \mathrm{d}t + (\boldsymbol{\Lambda}^+ - \boldsymbol{\Lambda}^-)\mathrm{d}\eta = \dot{\boldsymbol{\lambda}}_i \mathrm{d}t + \boldsymbol{\Lambda}_i \mathrm{d}\eta$ are differential measures for the velocity $\boldsymbol{u}$ and percussion $\boldsymbol{\Lambda}$. The measure $d\eta$ is a Dirac point measure and its integral is equal to 1 only at the impulsive event and vanishes during non-impulsive phases. Therefore, at the instance of the impact, the equality of measure yields the impact equations, and the constrained or unconstrained equations of motion otherwise. The percussions are the sum of their normal and tangential components over the set $\mathbb{H}$ of all closed contacts, i.e.

$$\mathrm{d}\boldsymbol{\Lambda} = \sum_{i \in \mathbb{H}} \mathbf{w}_N \, \mathrm{d}\Lambda_N + \mathbf{w}_T \, \mathrm{d}\Lambda_T, \tag{2.31}$$

where $\mathbf{w}_N$ and $\mathbf{w}_T$ are the generalized normal- and tangential force directions, respectively.

The kinematics of the contacts are defined by the relative velocities of the contact point and the static environment as presented in Section 2.1. We define the velocity difference before and after impact by

$$\xi_N := \gamma_N^+ + \varepsilon_N \, \gamma_N^-, \qquad \xi_T := \gamma_T^+ + \varepsilon_T \, \gamma_T^-, \tag{2.32}$$

where we set the coefficients of restitution $\varepsilon_N = \varepsilon_T = 0$ to model inelastic impacts. The γ are as defined in Equation (2.4), but split into normal and tangential direction, hence

$$\gamma_N = \mathbf{w}_N^T \, \mathbf{u}, \qquad \gamma_T = \mathbf{w}_T^T \, \mathbf{u}. \tag{2.33}$$

With the derived set-valued functions in Section 2.5.1, it is possible to define an inelastic kinematic impact- as well as a Coulomb frictional law for our system:

$$-\mathrm{d}\Lambda_N \in \mathrm{Upr}(\xi_N), \qquad -\mathrm{d}\Lambda_T \in \mu \, \mathrm{d}\Lambda_N \, \mathrm{Sgn}(\xi_T), \tag{2.34}$$

where μ is the dynamic friction coefficient of the system. The above equations can be combined to define a LCP which needs to be solved to provide the contact forces that comply with the kinematic contact laws (2.34) in this multi-contact problem. This step is not trivial and we refer the reader once again to the paper of Glocker [109].

$$\begin{pmatrix} \boldsymbol{\xi}_N \\ \boldsymbol{\xi}_R \\ \boldsymbol{\Lambda}_N \end{pmatrix} = \begin{pmatrix} \mathbf{W}_N^{\mathrm{T}} \mathbf{M}^{-1} (\mathbf{W}_N - \mathbf{W}_T \boldsymbol{\mu}) & \mathbf{W}_N^{\mathrm{T}} \mathbf{M}^{-1} \mathbf{W}_T & 0 \\ \mathbf{W}_T^{\mathrm{T}} \mathbf{M}^{-1} (\mathbf{W}_N - \mathbf{W}_T \boldsymbol{\mu}) & \mathbf{W}_T^{\mathrm{T}} \mathbf{M}^{-1} \mathbf{W}_T & \mathbf{I} \\ 2\boldsymbol{\mu} & -\mathbf{I} & 0 \end{pmatrix} \begin{pmatrix} \boldsymbol{\Lambda}_N \\ \boldsymbol{\Lambda}_R \\ \boldsymbol{\xi}_N \end{pmatrix} + \begin{pmatrix} \mathbf{W}_N^{\mathrm{T}} \mathbf{M}^{-1} \mathbf{h} \Delta t + (\mathbf{I} + \boldsymbol{\varepsilon}_N) \boldsymbol{\gamma}_N^A \\ \mathbf{W}_T^{\mathrm{T}} \mathbf{M}^{-1} \mathbf{h} \Delta t + (\mathbf{I} + \boldsymbol{\varepsilon}_T) \boldsymbol{\gamma}_T^A \\ 0 \end{pmatrix},$$

$$\begin{pmatrix} \boldsymbol{\xi}_N \\ \boldsymbol{\xi}_R \\ \boldsymbol{\Lambda}_N \end{pmatrix} \succeq 0 \qquad \begin{pmatrix} \boldsymbol{\Lambda}_N \\ \boldsymbol{\Lambda}_R \\ \boldsymbol{\xi}_N \end{pmatrix} \succeq 0 \qquad \begin{pmatrix} \boldsymbol{\xi}_N \\ \boldsymbol{\xi}_R \\ \boldsymbol{\Lambda}_N \end{pmatrix}^{\mathrm{T}} \begin{pmatrix} \boldsymbol{\Lambda}_N \\ \boldsymbol{\Lambda}_R \\ \boldsymbol{\xi}_N \end{pmatrix} = 0. \tag{2.35}$$

Equations (2.35) form the linear complementarity problem needed for the ground contact forces where,

$$\boldsymbol{\Lambda}_R := \boldsymbol{\mu} \boldsymbol{\Lambda}_N + \boldsymbol{\Lambda}_T, \tag{2.36}$$

$$\boldsymbol{\xi}_T := \boldsymbol{\xi}_R - \boldsymbol{\xi}_L, \tag{2.37}$$

$$\boldsymbol{\xi}_R := \mathbf{W}_N^{\mathrm{T}} \mathbf{u}^E + \boldsymbol{\varepsilon}_T \boldsymbol{\gamma}_T^A, \tag{2.38}$$

where the superscript A in $\boldsymbol{\gamma}_T^A$ refers to the initial point of the numerical step, and E as in $\mathbf{u}^E$ to the end point as will be discussed in more detail shortly, and

$$\mathbf{W}_N := (\mathbf{w}_{Ni_1}, ..., \mathbf{w}_{Ni_k}), \qquad \mathbf{W}_T := (\mathbf{w}_{Ti_1}, ..., \mathbf{w}_{Ti_k}) \in \mathbb{R}^{f \times k}$$

$$\boldsymbol{\Lambda}_N := (\Lambda_{Ni_1}, ..., \Lambda_{Ni_k})^{\mathrm{T}}, \qquad \boldsymbol{\Lambda}_T := (\Lambda_{Ti_1}, ..., \Lambda_{Ti_k})^{\mathrm{T}} \in \mathbb{R}^k$$

$$\boldsymbol{\gamma}_N^A := (\gamma_{Ni_1}^A, ..., \gamma_{Ni_k}^A)^{\mathrm{T}}, \qquad \boldsymbol{\gamma}_T^A := (\gamma_{Ti_1}^A, ..., \gamma_{Ti_k}^A)^{\mathrm{T}} \in \mathbb{R}^k$$

$$\boldsymbol{\xi}_N := (\xi_{Ni_1}, ..., \xi_{Ni_k})^{\mathrm{T}}, \qquad \boldsymbol{\xi}_T := (\xi_{Ti_1}, ..., \xi_{Ti_k})^{\mathrm{T}} \in \mathbb{R}^k$$

$$\boldsymbol{\varepsilon}_N := \mathrm{diag}(\varepsilon_{Ni_1}, ..., \varepsilon_{Ni_k}), \qquad \boldsymbol{\varepsilon}_T := \mathrm{diag}(\varepsilon_{Ti_1}, ..., \varepsilon_{Ti_k}) \in \mathbb{R}^{k \times k}$$

$$\boldsymbol{\mu} := \mathrm{diag}(\mu_{i_1}, ..., \mu_{i_k}) \in \mathbb{R}^{k \times k},$$

where f is the number of generalised coordinates and k the number of closed contacts.

2.5.4 Time Stepping Algorithm

The integration of measure differential inclusions is done here by time stepping methods which account for a combined evaluation of impact- and impact-free motion. The procedure is using a mid-point rule and can be summarised as follows. See also [109] for a more detailed description.

1. After choosing a time interval Δt, define the midpoint time $t^M := t^A + \frac{1}{2}\Delta t$, and end time $t^E := t^A + \Delta t$, where t^A is the initial time of the current iteration.

2. Define the midpoint displacement $\boldsymbol{q}^M := \boldsymbol{q}^A + \frac{1}{2}\Delta t\, \boldsymbol{u}^A \in \mathbb{R}^f$.

3. Calculate matrix properties at midpoint time

(a) $\mathbf{M}(\boldsymbol{q}^M, t^M) \in \mathbb{R}^{f\times f}$, $\boldsymbol{h}(\boldsymbol{q}^M, \boldsymbol{u}^A, t^M) \in \mathbb{R}^f$

(b) Out of $i = 1, ..., n$ contact points, set up the index set $\mathbb{H}$ of all k contacts $i_1, ..., i_k$ that are currently closed

(c) Then, combining all $i \in \mathbb{H}$, calculate $\mathbf{W}_N(\boldsymbol{q}^M, t^M) \in \mathbb{R}^{f\times k}$, as well as $\mathbf{W}_T(\boldsymbol{q}^M, t^M) \in \mathbb{R}^{f\times k}$

4. Solve the linear complementarity problem (2.35) in order to get $\boldsymbol{\Lambda}_N$ and $\boldsymbol{\Lambda}_R$

5. Compute the end velocity of the iteration step $\boldsymbol{u}^E$

$$\boldsymbol{u}^E = \mathbf{M}^{-1}(\mathbf{W}_N - \mathbf{W}_T\,\boldsymbol{\mu})\boldsymbol{\Lambda}_N + \mathbf{M}^{-1}\,\mathbf{W}_T\,\boldsymbol{\Lambda}_R + \mathbf{M}^{-1}\,\boldsymbol{h}\,\Delta t + \boldsymbol{u}^A$$

6. Compute the final state of the iteration $\boldsymbol{q}^E := \boldsymbol{q}^M + \frac{1}{2}\Delta t \cdot \boldsymbol{u}^E \in \mathbb{R}^f$

This concludes the used contact dynamics methods in this thesis. The multi-contact method due to Glocker as presented in this section was used in Chapter 5, where we model a multi-body system with two contacts that can potentially be closed at the same time. In the next chapter, the impulsive eccentric wheel model is introduced and analysed using the methods presented in this chapter.

Chapter 3

The Impulsive Eccentric Wheel Model[1]

The last chapter has introduced planar rigid body contact dynamics as a tool to model systems with discrete actuation. In this chapter, we develop a mathematical model based on contact dynamics for hopping locomotion which uses discrete actuation and rigid body shapes. We use the model to predict locomotion properties of hopping animals and robots and show that the model can produce a variety of locomotion trajectories as a function of control law and morphology.

3.1 Introduction

It has been reported that kangaroos use up less energy for hopping locomotion when moving faster due to the elastic energy storage in tendons and muscles [111]. This unique property and the fact that hopping on a small support polygon requires distinguished balance and poses hence a demanding control challenge, has urged engineers to design machines that reproduce animal like hopping behaviour. Significant contribution to the balance problem of hopping was due to Raibert [86], by introducing an intuitive control method for the hopping problem. Inspired by Raibert, many others have investigated hopping behaviour of monopod robots [112]. Energy efficiency of hopping motion has been demonstrated in [38], where

[1]This chapter presents the collaborative work with my supervisor F. Iida. I have initiated the problem statement, derived the theoretical equations, set up and conducted the simulation, prepared the figures in the experiment section, and wrote the paper. F. Iida helped revising the paper. The peer-reviewed publication which forms the basis of this chapter is

- Fabio Giardina and Fumiya Iida. Simulation of forward hopping dynamics in robots and animals using a template with a circular foot and impulsive actuation. In *Biomedical Robotics and Biomechatronics (BioRob), 2016 6th IEEE International Conference on*, pages 7–12. IEEE, 2016.

the simple robot Cargo (Figure 3.2) showed not only highest energy efficiencies, but also flexibility in hopping with different payloads.

Mathematical modelling has proven to be valuable for the analysis of animal behaviour. Some models are strong enough to explain locomotion dynamics in biological systems in a simplified way, such as the walk to run transition observed in humans [11]. In [113] it was proposed that general traits of locomotion should be analysed by building a "template" (mathematical model) that focuses on the desired aspects to analyse. One of the most widely used templates in legged locomotion is the spring loaded inverted pendulum model (SLIP), first introduced in [12]. Locomotion is modelled with a point mass and a massless spring representing the leg. Several properties of animal locomotion could be explained with SLIP For example the leg-adjustment strategy during flight phase of human running [114]. Scientists soon realised that using curved feet in templates, as opposed to pin pointed feet, can have beneficial influences on stability of the dynamical hopping motion [40]. When extending the SLIP model with a curved foot, stability regions can be widened [115]. A hybrid robot that uses a wheeled configuration with an off-centred mass was presented in [116]. The design promises stable locomotion and the robot is capable of traversing obstacles and ditches. Another demonstration of how a simple design can generate stable and efficient hopping locomotion using a rigid curved foot was also demonstrated in [36]. The authors used a numerical model to define hopping behaviour of a two body system with a curved foot and joint actuation and predicted stable and efficient locomotion, which was demonstrated to hold in a realisation of the model.

The template presented here is modelled using rigid body dynamics with collisions and impulsive actuation forces. There are no joints, springs or dampers in the system. The template focuses on the physical interaction of the foot with the rigid ground, as opposed to the compliance of the leg as is analysed in the SLIP model. Furthermore, due to the dissipation of energy at ground collision, energy needs to be injected into the system. Rather than adding energy evenly during the stance phase, the template reduces the energy injection time to an instant and alters the energy at take-off by applying an impulse.

The model is reduced to the described level of abstraction as locomotion is assumed to be influenced by three main factors: The shape of the system and the environment, the collisional forces, and the forces applied at the switching point from stance to flight phase. The implications of these assumptions are that the stance and flight phase becomes completely passive and the sequence of motion is predetermined by the mechanical shape, requiring no control. The downside is that stability can only be influenced by the impulse parameters at transition between stance and flight phase, and needs to rely on the self-stabilising mechanics of the system to reach a stable limit cycle. Nevertheless, this template

aims at understanding the interplay between mechanical stability and minimalistic control to achieve stable locomotion, rather than using high bandwidth feedback control.

The chapter is structured as follows. In the next section, the mathematics needed for the modelling of the template are introduced. Section III presents the simulation set-up for the analysis and comparison with the real world systems. Section IV shows the results, and finally Section V concludes the chapter.

3.2 Template

The hopping template is described as a planar rigid body with mass m and moment of inertia around the centre of mass I that is interacting with a flat and rigid ground. The foot of the rigid body is circular with radius R and the mass is lumped inside the foot and rigidly attached to it with a radial leg distance of l, as illustrated in Figure 3.1. Note that the eccentricity a is related to this parameter by $a = R - l$. The state of the lumped mass is completely described by the generalised coordinates

$$\boldsymbol{q}^T = [x, y, \phi]$$

and the generalised velocity

$$\boldsymbol{u}^T = [\dot{x}, \dot{y}, \dot{\phi}].$$

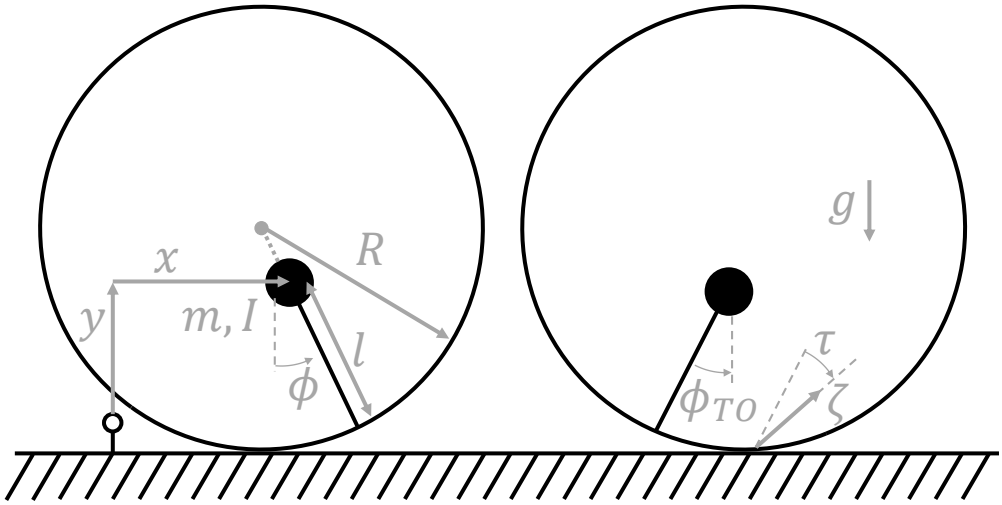

Fig. 3.1 Sketch of template. The left hand side illustrates the template at touchdown with system states $\boldsymbol{q}^T = [x, y, \phi]$ and design parameters R, l, m, and I, and the right hand side shows the control parameter take-off angle ϕ_{TO}, the force tilt angle τ, gravity g, and the impulse $\boldsymbol{\zeta}$.

Gravity is acting upon the rigid body with gravitational acceleration $\mathbf{g}$. The energy input to the system comes from an impulse $\boldsymbol{\zeta}$ acting at the contact point between the border and the ground. The force direction is parallel to the connecting bit with length l from the border to the lumped mass, deviating by an angular tilt of τ. This force can be thought of as a very stiff spring connecting the foot and the lumped mass, that is preloaded and released in an instant and extending infinitesimally. The magnitude of $\boldsymbol{\zeta}$ is chosen such that the kinetic energy of the rigid body is altered from its take-off state $\boldsymbol{q}_{TO}$ by ΔE.

The ground contact forces are defined by a Newtonian kinematic impact law with coefficient of restitution of $\varepsilon = 0$ and a no slip condition for the foot when in contact with the ground, which guarantees that pure rolling is achieved.

3.2.1 Derivation of Template Equations

The impulse is applied when the system reaches a predefined state $\boldsymbol{q}_{TO}$ with angle ϕ_{TO} during stance phase. There are four main events that map a take-off state to the next one, namely impulse, flight phase, touchdown, and rolling.

As briefly mentioned above, the impulse is applied such that the kinetic energy of the body is increased by a defined energy ΔE. This can be formulated mathematically

$$\Delta E = \frac{1}{2}(\boldsymbol{u}_{TO}^{+})^{T}\mathbf{M}\boldsymbol{u}_{TO}^{+} - \frac{1}{2}(\boldsymbol{u}_{TO}^{-})^{T}\mathbf{M}\boldsymbol{u}_{TO}^{-}, \tag{3.1}$$

where $\boldsymbol{u}_{TO}^{+}$ is the derivative of the take-off state after, and $\boldsymbol{u}_{TO}^{-}$ before the impulse is applied, and $\mathbf{M}$ is the mass matrix of the system. The dynamics over the impulsive event are stated as in Section 2.4.

$$\mathbf{M}(\boldsymbol{u}_{TO}^{+} - \boldsymbol{u}_{TO}^{-}) = \mathbf{J}_c^{T}\boldsymbol{\zeta}, \tag{3.2}$$

with $\mathbf{J}_c$ the contact Jacobian of the body with respect to the ground contact point on the foot, as also defined in Section 2.1. Solving for the post-impulse velocity one obtains

$$\boldsymbol{u}_{TO}^{+} = \mathbf{M}^{-1}\left(\mathbf{J}_c^{T}\boldsymbol{\zeta}\right) + \boldsymbol{u}_{TO}^{-}. \tag{3.3}$$

Combining Equations (3.1) and (3.3) one can see that

$$\Delta E = \frac{1}{2}\boldsymbol{\zeta}^{T}\mathbf{J}_c\mathbf{M}^{-1}\mathbf{J}_c^{T}\boldsymbol{\zeta} + \boldsymbol{\zeta}^{T}\mathbf{J}_c\boldsymbol{u}_{TO}^{-}. \tag{3.4}$$

Since we know the take-off angle ϕ_{TO} and the force direction of $\boldsymbol{\zeta}$ we can define

$$\boldsymbol{\zeta} = ||\boldsymbol{\zeta}|| \begin{pmatrix} -\sin(\phi_{TO}+\tau) \\ \cos(\phi_{TO}+\tau) \end{pmatrix} =: ||\boldsymbol{\zeta}||\boldsymbol{\rho}, \tag{3.5}$$

with τ the tilt angle of the impulse direction from the leg angle. Equations (3.4) and (3.5) provide the magnitude for the impulse

$$||\boldsymbol{\zeta}|| = \frac{-\boldsymbol{\rho}^T \mathbf{J}_c \boldsymbol{u}_{TO}^- + \sqrt{\left(\boldsymbol{\rho}^T \mathbf{J}_c \boldsymbol{u}_{TO}^-\right)^2 + 2K\Delta E}}{K}, \tag{3.6}$$

with $K = \boldsymbol{\rho}^T \mathbf{J}_G \mathbf{M}^{-1} \mathbf{J}_G^T \boldsymbol{\rho}$. The mapping from the state before the impact to the take-off state is now defined by

$$\boldsymbol{u}_{TO}^+ = \mathbf{M}^{-1} \mathbf{J}_c^T \boldsymbol{\rho} ||\boldsymbol{\zeta}|| + \boldsymbol{u}_{TO}^-. \tag{3.7}$$

The mapping from flight phase to touchdown can easily be derived from the take-off state, once the flight time is known. To define the distance between the foot and the ground a gap function g_N is introduced

$$g_N = y + (R-l)\cos\phi - R \tag{3.8}$$

The kinematic motion of the flight phase is simply defined by

$$\begin{pmatrix} y_F \\ \phi_F \end{pmatrix} = \begin{pmatrix} y_{TO} + \dot{y}_{TO} t_F - \frac{1}{2} g t_F^2 \\ \phi_{TO} + \dot{\phi} t_F \end{pmatrix} \tag{3.9}$$

where $t_F \in [0, t_{TD}]$ is the flight time from take-off to touchdown and g is the gravitational acceleration. As soon as the gap function becomes equal to zero after take-off, the touchdown state has been reached. Combining Equations (3.8) and (3.9) yields

$$y_{TO} + \dot{y}_{TO} t_{TD} - \frac{1}{2} g t_{TD}^2 + (R-l)\cos\left(\phi_{TO} + \dot{\phi} t_{TD}\right) - R = 0. \tag{3.10}$$

After solving this implicit equation for t_{TD}, one can simply find the pre-impact state where the body touches the ground

$$\boldsymbol{u}_{TD} = \boldsymbol{u}_{TO} - \begin{pmatrix} 0 \\ g t_{TD} \\ 0 \end{pmatrix} \tag{3.11}$$

$$\boldsymbol{q}_{TD} = \boldsymbol{q}_{TO} + \boldsymbol{u}_{TO} t_{TD} - \begin{pmatrix} 0 \\ \frac{1}{2} g t_{TD}^2 \\ 0 \end{pmatrix}. \tag{3.12}$$

To calculate the post impact state we need to take into account the impact event, which is modelled by a Newtonian kinematic impact law with a coefficient of restitution of $\varepsilon = 0$. Analogously to the impulse equations (3.3), we have that

$$\boldsymbol{u}_{TD}^{+} = \mathbf{M}^{-1}\left(\mathbf{J}_c^T \boldsymbol{\Lambda}\right) + \boldsymbol{u}_{TD}^{-}. \tag{3.13}$$

where $\boldsymbol{\Lambda}$ is the impact at touchdown. The impact condition requires that $\mathbf{J}_c \boldsymbol{u}_{TD}^{+} = 0$, which together with Equation (3.13) and after some manipulation (see Section 2.3) leads to the mapping

$$\boldsymbol{u}_{TD}^{+} = \left(\mathbf{I} - \mathbf{M}^{-1}\mathbf{J}_c^T\left(\mathbf{J}_c\mathbf{M}^{-1}\mathbf{J}_c^T\right)^{-1}\mathbf{J}_c\right)\boldsymbol{u}_{TD}^{-}. \tag{3.14}$$

The final step is to derive a mapping from the post-impact state to the pre-take-off state which happens during stance phase. Since pure rolling is assumed, no energy is lost during the stance phase and the sum of the kinetic and potential energies of the touchdown and take-off postures will be equivalent.

$$\frac{1}{2}(\boldsymbol{u}_{TO}^{-})^T\mathbf{M}\boldsymbol{u}_{TO}^{-} + mgy_{TO} = \frac{1}{2}(\boldsymbol{u}_{TD}^{+})^T\mathbf{M}\boldsymbol{u}_{TD}^{+} + mgy_{TD}. \tag{3.15}$$

The rolling condition also provides a fixed relation between the lumped mass velocity vector and the angular velocity, namely that $(\dot{x}_S \quad \dot{y}_S \quad 0)^T = \dot{\boldsymbol{\phi}}_S \times \boldsymbol{r}$, where the subscript S tags the stance phase, $\dot{\boldsymbol{\phi}}_S = (0 \quad 0 \quad \dot{\phi}_S)^T$, and $\boldsymbol{r}$ is the vector pointing from the current ground contact point to the lumped mass. Hence we have for the generalised velocity state

$$\boldsymbol{u}_S = \dot{\phi}_S \begin{pmatrix} (R-l)\cos\phi_S - R \\ (R-l)\sin\phi_S \\ 1 \end{pmatrix} =: \dot{\phi}_S \boldsymbol{\xi}. \tag{3.16}$$

Equations (3.15) and (3.16) can then be combined to read

$$\frac{\dot{\phi}_S^2}{2}\boldsymbol{\xi}^T\mathbf{M}\boldsymbol{\xi} = E_{TD}^{+} - mgy_{TO}, \tag{3.17}$$

with $E_{TD}^{+} := \frac{1}{2}(\boldsymbol{u}_{TD}^{+})^T\mathbf{M}\boldsymbol{u}_{TD}^{+} + mgy_{TD}$.

Therefore, the take-off angular velocity of the predefined take-off angle ϕ_{TO} is

$$|\dot{\phi}_{TO}^{-}| = \sqrt{\frac{2(E_{TD}^{+} - mgy_{TO})}{\boldsymbol{\xi}^T\mathbf{M}\boldsymbol{\xi}}}, \tag{3.18}$$

and hence the take-off velocity state

$$\boldsymbol{u}_{TO}^{-} = \text{sign}(\dot{\phi}_{TO}^{-})|\dot{\phi}_{TO}^{-}|\boldsymbol{\xi}. \tag{3.19}$$

Note that the sign of $\dot{\phi}_{TO}^{-}$ can be retrieved by checking the touchdown angle and the touchdown angular velocity. Since no energy is added during stance phase, once the predefined take-off angle is reached, the system switches to the impulse event. Also, it may happen that the dissipative impact causes the system energy to drop below the potential energy required to reach the take-off angle. In this case, the system configuration needs to be considered unstable.

3.3 Simulation Set-Up

The template was tested and examined with various parameter settings. In the first simulation, a parameter search was conducted using properties of the hopping robot Cargo [38]. A range of take-off angles and foot radii were chosen to examine the template's response to locomotion speed and efficiency. The parameter settings can be found in Table 5.1. Two motion tracking measurements of Cargo were used to compare the centre of mass position of the template with the robot. Finally, data from two hopping animals were used to investigate the predictability of locomotion features by the template.

As Table 5.1 indicates, it is sufficient for the template to adapt to a new type of setting by changing seven parameters, namely foot radius R, leg length l, mass m, take-off angle ϕ_{TO}, energy input per hop ΔE, impulse tilt τ, and moment of inertia I. The hopping states are then derived by using the equations presented in the previous section. Initial conditions were set to a resting state during stance phase just before take-off at position ϕ_{TO}, with $\boldsymbol{u} = \boldsymbol{0}$. The simulation is then expected to converge to a steady state hopping behaviour after 100 iterations per case. Once initialised, the post take-off state is derived by (7). The flight time given by the implicit Equation (10) is computed by numerical methods using Matlab's root search *fzero*. Pre-touchdown states are then determined using (11) and (12). The post touchdown conditions are defined by (14), and finally, the pre take-off state of the next iteration is given by (19), which concludes a hopping cycle. Note that the energy inputs for the template as shown in Table 5.1 do not correspond to the energy inputs of the real robot. The values are higher than in the robot, as the payload suspension with springs enables the robot to restore energy which is not the case in the template.

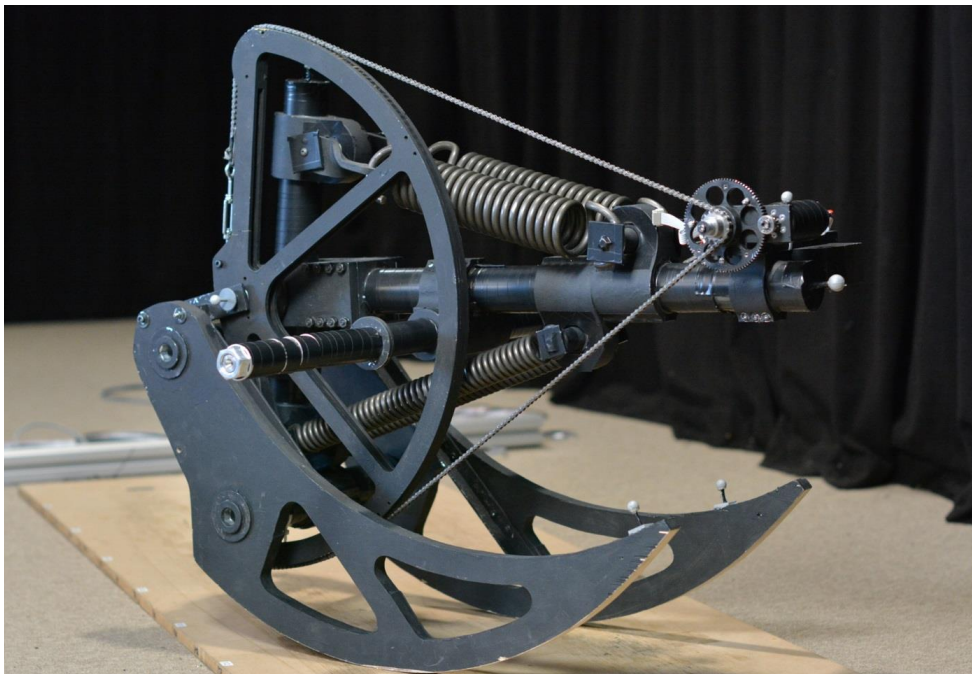

Fig. 3.2 Cargo robot as first presented in [38].

3.4 Results

The results generated according to the set-up described in the last section are presented here. First, the template results over a range of the parameter space are presented and we later apply the Cargo robot parameters to the template to predict two real-world trajectories of the robot. Data from tammar wallaby and kangaroo rats presented in [64] are then analysed and compared with the template predictions.

3.4.1 Template behaviour

To illustrate the template behaviour, we assign parameter values of the robot Cargo as per Table 5.1 to the template and vary the foot radius and take-off angle in a defined parameter space. The result for the simulation is shown in Figure 3.3. Figure 3.3 (a) shows the prediction of the template of the energetic cost of transport (CoT), which is defined as the energy used per body weight and distance travelled as defined in [117]. As can be seen, the cost of transport varies gradually with changing leg length to foot radius ratio. A large foot radius compared to the leg length results in more efficient locomotion and a smaller foot radius shows a higher cost of transport. Areas where no colour is plotted (white spaces) indicate that the template did not converge to a fixed point in the simulation. This means on the other hand, that all the coloured spaces demonstrated self-stable properties, or in other

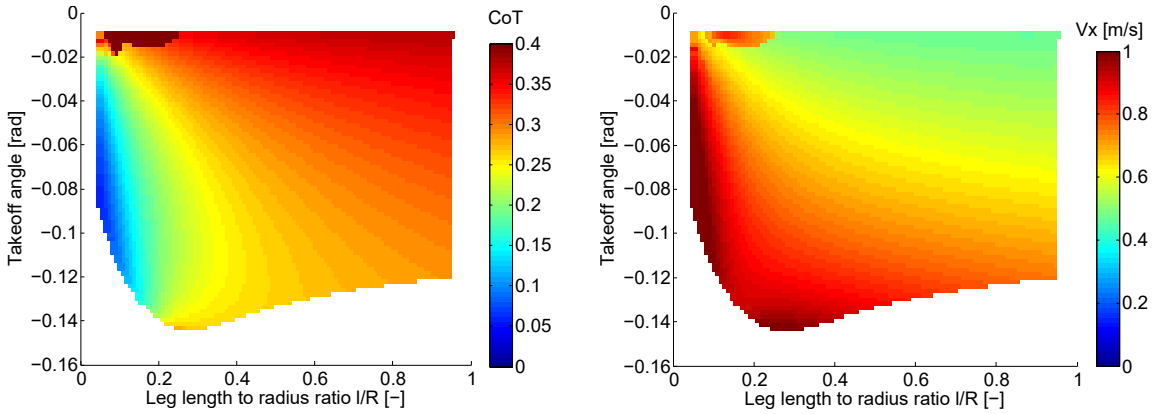

(a) Cost of transport (CoT) for travelled distance of last 10 hops of simulation

(b) Locomotion velocity of average last 10 hops of simulation

Fig. 3.3 Coloured efficiency and velocity plots of parameter search of the template with parameter settings derived from the robot Cargo. The abscissa shows the leg length to radius ratio l/R and the ordinate shows the defined take-off angle ϕ_{TO}.

words, converge to a constant touchdown angle. Furthermore, stable hopping regions are found for larger take-off angles in the region of $l/R = 0.25$. In the top left region of the figure, a small area with large cost of transport appears abruptly. This motion varies from the other stable parameter choices in its gait by changing direction of locomotion after every iteration and rolling over a long portion of the foot. For the other more efficient stable solutions, the gait looks as illustrated in Figure 3.4. The course of motion of this particular pattern is as follows. First, the robot experiences an impulse and lifts off. Due to the offset of the point of attack of the force the robot or template is forced into a turning motion as the impulse occurs, and the foot is therefore moving ahead of the centre of mass during flight phase. After the flight phase an impact slows the system down and cause a moment into the opposite direction as the impulsive take-off force. Therefore and with the friction of the ground, the system rolls over the foot until the next take-off position is reached.

Figure 3.3 (b) shows the average hopping velocity over the last 10 hops of the simulation of the same parameter conditions as in Figure 3.3 (a). The velocity tends to increase with smaller ratio of leg length to foot radius l/R, which corresponds to the cost of transport values as the velocity is inversely proportional to the cost of transport for constant locomotion power. For the smallest stable take-off angles, the locomotion speed increases and reaches similar values at $l/R = 0.25$ as it does at $l/R = 0.05$. This indicates that the energy loss due to impact is larger at smaller take-off angles that reach the same locomotion speed. In the top left part of the figure, the small area with a different locomotion gait as described in the CoT

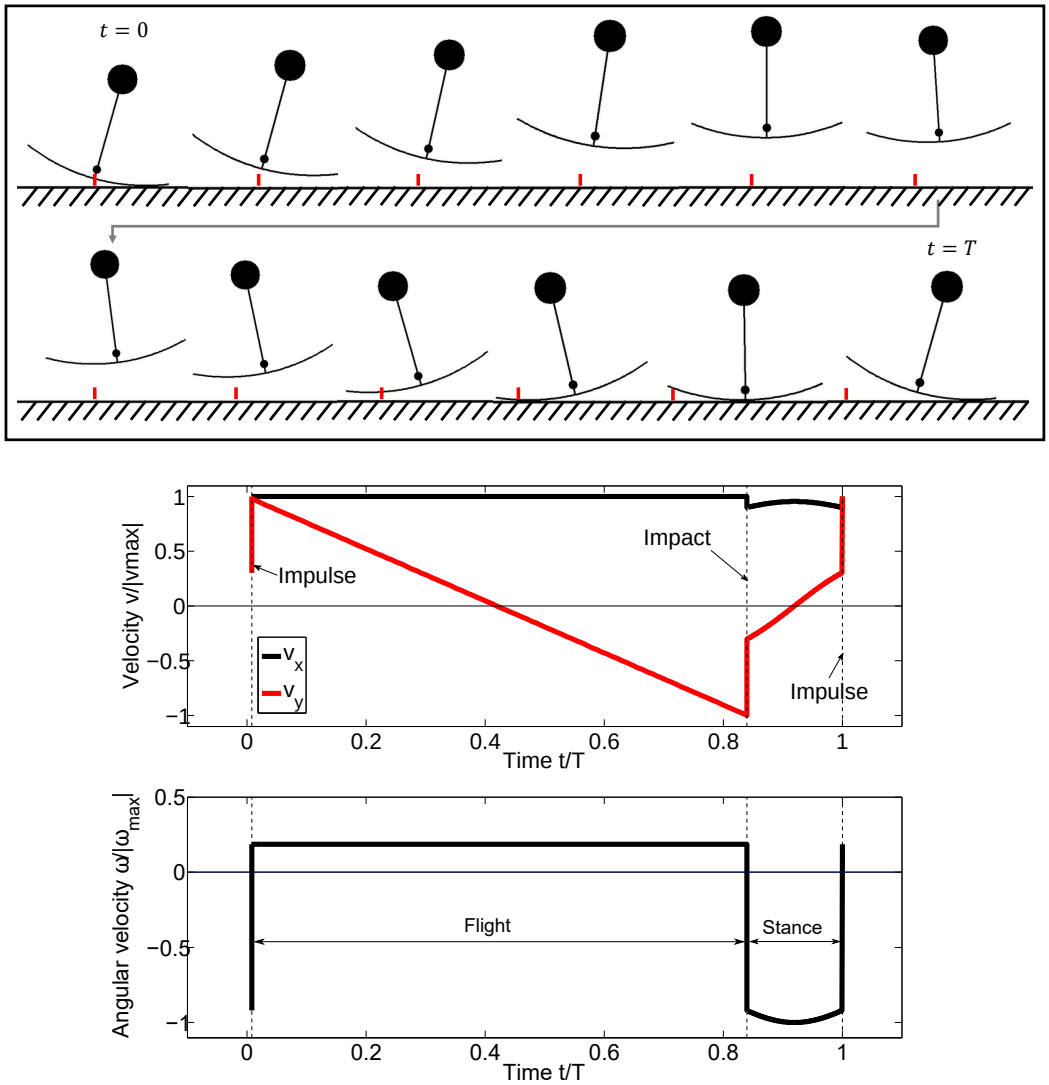

Fig. 3.4 Template time series of a hopping cycle of a Cargo like motion with take-off, flight phase, touchdown and rolling during stance phase. State velocities of motion are shown in the lower two figures with $[v_x, v_y, \omega] = [\dot{x}, \dot{y}, \dot{\phi}]$.

Table 3.1 Parameter ranges of template for simulated cases.

	Parameter	Symbol	Value
Cargo Param. Search	Foot radius	R	$[0.3, 5.8]\,m$
	Leg length	l	$0.288\,m$
	Mass	m	$130\,kg$
	Takeoff angle	ϕ_{TO}	$[-0.01, -0.2]\,rad$
	Energy input	ΔE	$35\,J$
	Impulse tilt	τ	$-0.2\,rad$
	Moment of inertia	I	$4.1\,kg\,m^2$
Cargo Trajectory 1	Foot radius	R	$0.42\,m$
	Leg length	l	$0.288\,m$
	Mass	m	$130\,kg$
	Takeoff angle	ϕ_{TO}	$-0.07\,rad$
	Energy input	ΔE	$33.6\,J$
	Impulse tilt	τ	$-0.15\,rad$
	Moment of inertia	I	$4.1\,kg\,m^2$
Cargo Trajectory 2	Foot radius	R	$0.42\,m$
	Leg length	l	$0.288\,m$
	Mass	m	$130\,kg$
	Takeoff angle	ϕ_{TO}	$-0.1\,rad$
	Energy input	ΔE	$37.6\,J$
	Impulse tilt	τ	$-0.22\,rad$
	Moment of inertia	I	$4.1\,kg\,m^2$
Tammar wallaby	Foot radius	R	$1.39\,m$
	Leg length	l	$0.305\,m$
	Mass	m	$6.6\,kg$
	Takeoff angle	ϕ_{TO}	$[-0.01, -0.24]\,rad$
	Energy input	ΔE	$[5.66, 10.3]\,J$
	Impulse tilt	τ	$0\,rad$
	Moment of inertia	I	$0.19\,kg\,m^2$
Kangaroo rat	Foot radius	R	$0.35\,m$
	Leg length	l	$0.063\,m$
	Mass	m	$0.11\,kg$
	Takeoff angle	ϕ_{TO}	$[-0.09, -0.12]\,rad$
	Energy input	ΔE	$[3.1, 4.3]\,mJ$
	Impulse tilt	τ	$0\,rad$
	Moment of inertia	I	$1.35 \cdot 10^{-5}\,kg\,m^2$

case is visible. Although the velocity seems to be high, the effective travelled distance is low, as the absolute value of the velocity per hop is illustrated.

3.4.2 Cargo Trajectory Comparison

As described in the simulation set-up section, two real world trajectories of the hopping robot Cargo were stored and compared to the template centre of mass trajectory. Figure 3.5a presents the results for a motor torque amplitude of $T_M = 20.1\,Nm$ and a hopping frequency of $f = 2.58\,Hz$. The figure shows the template trajectory of the centre of mass and the motion of the lower leg of Cargo projected to the average centre of mass position of Cargo. The experimental results were shifted in the horizontal direction to maximally match the pattern of the predicted template trajectory. Although the transient phase to a stable hopping pattern is not matching, the average hopping height and stride length are overlapping well. The deviations can be explained by the large oscillating hopping mass of Cargo, which is absent in the template. Furthermore, the stance phase in the experimental data is not as clearly visible as in the template. The deviation may arise due to the strong springs that are acting on the lower body of Cargo. The trajectories of Cargo also seem skewed towards the left which is not visible in the template results and may also be due to the springs and the fact that the centre of mass and the moment of inertia in Cargo is constantly oscillating.

For the second case shown in Figure 3.5b where $T_M = 29.5\,Nm$ and the hopping frequency of $f = 2.52\,Hz$, similar observations can be made. The template is capable of predicting the resulting hopping speed of $0.27\,m/s$, the stride length, and the hopping height. There is again an oscillation of the robot trajectory around the predicted value, which we attribute to the oscillating mass on Cargo.

3.4.3 Hopping Animal Comparison

Next to the comparison of the robot Cargo, locomotion data from hopping animals have been applied to the template and the characteristics of both template and animals were compared. In particular, data from tammar wallabies and kangaroo rats presented in [64] are used for analysis. Using the energy input and take-off angle the animal uses to achieve a certain hopping speed, and a leg length to foot radius ratio of $l/R = 0.22$ and $l/R = 0.18$ for the tammar wallaby and kangaroo rat case, respectively, certain characteristic locomotion properties could be reproduced with the template. Figure 3.6 shows the comparison of stride length for both animals with the template predictions for various dimensionless animal velocities. The dimensionless velocity is the square root of the froude number $\hat{s} = \sqrt{Fr} = \bar{v}/\sqrt{g/l}$, where $\bar{v}$ is the average forward velocity and l is the leg length of the animal. It is

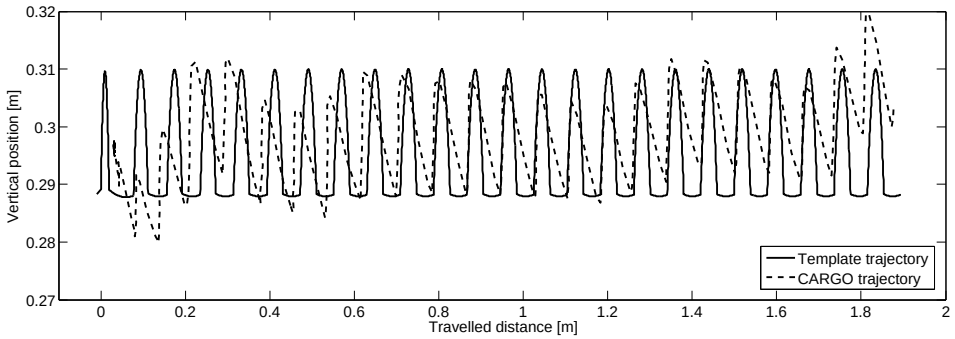

(a) Template and Cargo at sinusoidal motor torque in the joint with amplitude $T_M = 20.1\,Nm$ and frequency $f = 2.58\,Hz$

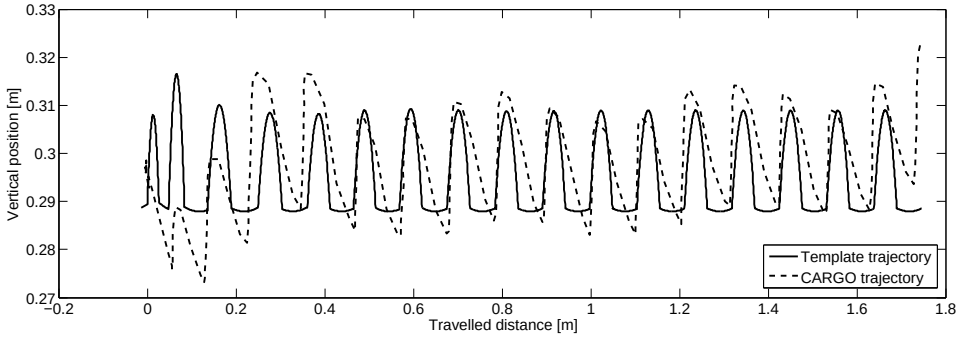

(b) Template and Cargo at sinusoidal motor torque in the joint with amplitude $T_M = 29.5\,Nm$ and frequency $f = 2.52\,Hz$

Fig. 3.5 Centre of mass trajectory comparison of two parameter sets between Cargo and the template. The first case a) is at a locomotion speed of roughly $0.2\,m/s$ and case b) $0.27\,m/s$.

important to note that the dimensionless velocity is only assigned for the animal curves, and the template was run with the animal parameters (energy input and take-off angle) at these particular velocities. The template velocities tend to be significantly slower than observed in both kangaroo rat and tammar wallaby, which may arise due to unmodelled adaptability of legs like energy saving mechanisms and leg angle of attack at touchdown.

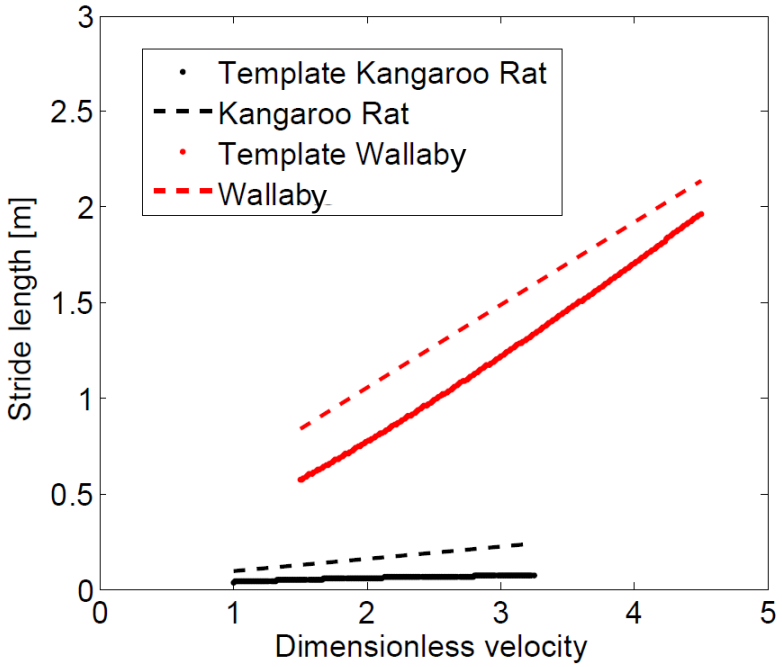

Fig. 3.6 Comparison of stride length between the template predicions and data from tammar wallabies and kangaroo rats for various dimensionless velocities v/l.

3.5 Conclusion

The template presented in this chapter shows that it is capable of imitating locomotion traits found in a real hopping robot such as locomotion speed, hopping height, hopping frequency, and stride length. Template results are not yet at the level of correspondence with animal data such that confident conclusions can be drawn. However, the template reproduces some locomotion characteristics found in tammar wallabies and kangaroo rats that seem promising and are encouraging to elaborate the presented template. In the next chapter, the results of the impulsive eccentric wheel are presented in a broader context. By studying the energetics of locomotion as predicted by the model, we will aim to find principles for locomotion in general as opposed to focusing on individual representation of animal and robot trajectories.

Chapter 4

Energetics of Surpassing Obstacles[1]

The last chapter introduced the impulsive eccentric wheel model with which hopping trajectories can be generated based on discrete actuation. In this chapter, we neglect the dynamics of periodic locomotion and focus on a single hop to study the theory of energetics in the framework of discrete actuation. Again, we examine the case of hopping locomotion but add an obstacle as an additional element to the system. The obstacle allows for an energetic analysis as energy has to be expended to overcome it, and this allows locomotion strategies like rolling to be compared energetically to hopping.

4.1 Introduction

Rolling wheels are designed to operate in flat environments and are optimised for this specific domain. The economic costs for transportation drive the design of wheeled vehicles towards ever less fuel consumption, defining energy expenditure as one of the main objectives to be minimised. While a rolling strategy is undoubtedly dominating flat terrains in terms of energy expenditure, the strategy should be reconsidered in more complex environments. Wheeled locomotion in natural terrain has been extensively studied in the field of terramechanics [118], which employs empirical and computational tools to model and predict the soil-vehicle interaction. Terramechanics has aided the design of off-road vehicles ever since cars left roads, and with the advent of planetary exploration rovers which need to operate

[1]This chapter presents the collaborative work with my supervisor F. Iida. I have initiated the problem statement, derived the theoretical equations, made the allometric model, conducted, planned and prepared the experiments, and wrote the paper. F. Iida helped discussing and revising the paper. The manuscript which is published in *PLOS ONE* and which forms the basis of this chapter is

- Fabio Giardina and Fumiya Iida. Collision-based energetic analysis of rolling and hopping over obstacles. *PLOS ONE*, 13(3): e0194375, 2018.

in surroundings with loose soil and variable terrain conditions [119], more challenging terrain-wheel interactions are being analysed.

Alternatives to rolling are readily displayed by nature's crawling, hopping and running animals, but can these gaits compete with the energy effective rolling motion? In a study where cyclists compete against runners in an off-road track, it was found that their energy expenditure is comparable [120], but cyclists finished significantly faster. This implies that even when rolling and running strategies are compared on an equal footing, the rolling strategy still outperforms the running one in terms of its speed. This comparison, however, is commonly done in environments which lack an important element of natural terrain: obstacles. The energetic cost of a wheel colliding with obstacles is a classical problem in mechanics [121], yet it is generally only studied for rolling collisions.

The study of the rimless wheel [13], [122] calls attention to the similarities of rolling and walking collisions, and links wheeled locomotion to legged locomotion. Collision mechanics is a commonly used tool for analysis of legged locomotion, as repetitive leg-ground interactions are typical in this form of locomotion. The simplest models reduce the analysed system to a single body with point mass, and look at the momentum balance of the collision such as in [51], where the authors explain observed locomotion behaviour in the walk to run transition, and the elastic behaviour in stance phase during running. An analogous approach studies collisional behaviour of quadrupedal animals [123] and shows that walk and gallop provide collision reduction strategies in stance phase. Collisional analysis of gaits is not confined to legged locomotion, but has also been used to study arboreal locomotion, such as brachiation in gibbons, to explain the observed overshoot during swinging motion [124]. Other collision-based models study two-bodied locomotion, such as in [10] where toe-off impulses acting on a two-legged system are investigated. A similar system is introduced in [44], where the concept of passive dynamic walking is studied in a collisional context. Extensions of the two-legged models also investigate the effect of mass distribution on stability as described in [47] and [52]. Collision-based models have not only led to the advancement of our theoretical understanding of locomotion, but also facilitated the creation of dynamic walking robots [125]. Even though collision-based models have been studied extensively in the past, the effect of mass distribution on the energetic cost of actuation and collision have not been investigated in depth, which we deem crucial for the study of a rotating and hopping wheel.

In this work, we make use of the collision-based modelling approach to analyse energy expenditure of three strategies in a wheeled system in the task of overcoming an obstacle, and explicitly emphasise the role of mass distribution in the energetic analysis of actuation and collision. We quantify mass distribution by the wheel's moment of inertia around the

centre of mass, which uniquely defines the inertial properties of the rigid body. We find a new way of overcoming the obstacle which is associated with low energetic costs in the case of a small moment of inertia. The model thus underscores the importance of moment of inertia and centre of mass position in locomotion with collisional events and suggests a new perspective to understand and induce hopping. Other than the quantitative analysis of energetic advantage of hopping and rolling, this model can provide useful insights to the study of moment of inertia-dependent dynamics in locomotion such as in swing-leg retraction [92], posture control during flight phase [126], and balance during stance phase [127].

We test and compare the energetic cost of three distinct strategies for a rigid wheel to overcome an acute and rigid obstacle of given height, as illustrated in Figure 1. We use the result of this comparison to find conditions for which hopping is energetically advantageous to rolling. We then take the theoretical result and use it to study its prediction on animal-related locomotion conditions. The three strategies we analyse are governed by different physical effects to overcome the obstacle. The rolling strategy shown in Figure 1c is characterised by a wheel with centred mass colliding with the obstacle and subsequently rolling over it. In the trivial hopping strategy as shown in Figure 1b, the kinetic energy of the system is increased in vertical direction by the potential energy required to overcome the obstacle ($\Delta E_{TH} = mgh$). We introduce a third strategy with the rotational hopping strategy as shown in Figure 1a. This strategy exploits rotation to overcome the obstacle and–as we will see–not only surpasses the trivial hopping strategy in terms of energy effectiveness, but also displays characteristics of legged hopping locomotion. The wheel's mass distribution in this strategy is such that the centre of mass is off-centred, due to which the centre of mass velocity will eventually have a component in vertical direction as the wheel rolls over the ground. At a point where the velocity is directed away from the ground, an induced rotation causes the wheel to revert its angular velocity. This forces the boundary of the wheel to move away from the ground, which thus leads to a change from rolling to a ballistic flight phase. The cost of this strategy is composed of the energetic cost of reverting the rotation at take-off and the energetic cost of collision at touchdown.

The model for all strategies is completely described with its wheel radius R, its eccentricity a (for the rotational hopping strategy), the mass located in the centre of mass m, the moment of inertia around the centre of mass I, the obstacle height h, and the approach velocity u_x. We will first analyse locomotion strategies without specifying mass-size relationships before we apply an allometric scaling law derived from hopping, running and trotting animals. This relates mass, radius and moment of inertia to animal properties, and invokes the question of whether animals would prefer to roll or hop in given environmental conditions.

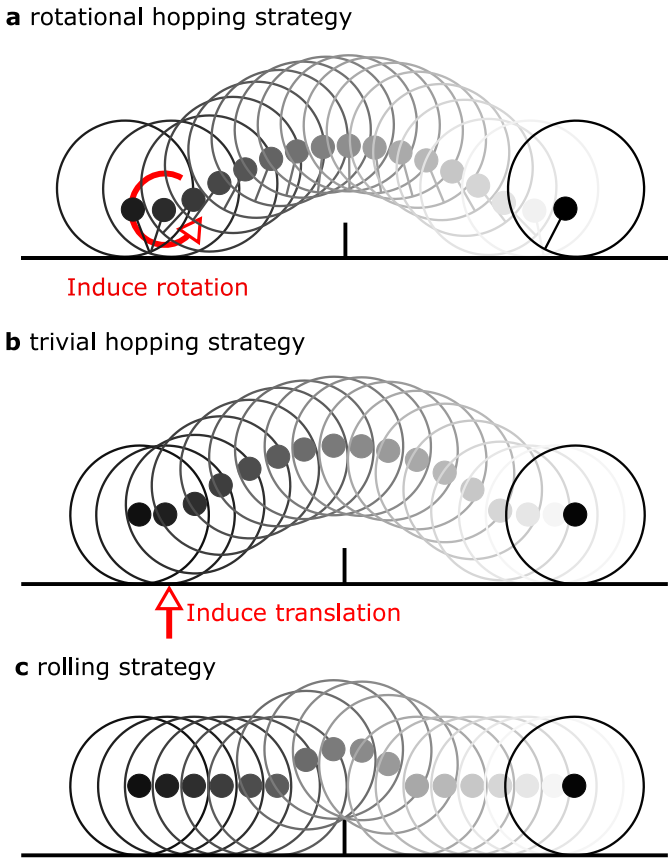

Fig. 4.1 **Locomotion strategies**. The motion progression of the three studied strategies to overcome an obstacle. Energetic cost of collision is derived and completely defined for each strategy by wheel radius R, eccentricity a of the wheel, the mass located in the centre of mass m, the moment of inertia around the centre of mass I, the obstacle height h, and the approach velocity u_x. **a**, Motion progression of the rotational hopping strategy using an off-centred wheel. Hopping is induced by reverting the rotation during stance phase. **b**, Motion progression of the trivial hopping strategy using a wheel with centred mass. Hopping is induced by an increase of the kinetic energy in vertical direction. **c**, Motion progression of the rolling strategy. The obstacle is overcome by a wheel with centred mass colliding and rolling over it.

The next section gives a detailed description of the used model and methods, followed by the results of the strategy comparison and the study of the theoretical model for allometric (animal related) scaling laws. We then verify the energetic collision losses of rolling and hopping in an experimental setup of a wheel-obstacle test platform, before we discuss the results of the strategy comparison.

4.2 Methods

4.2.1 Model Assumptions

The subsequent theoretical analysis uses standard assumptions of planar rigid body mechanics. The body inertia is given by the centre of mass with the point mass m, and the mass distribution represented by the moment of inertia I around the centre of mass. Collision of the rigid body with the environment takes place at its boundary, which is a circular shape in all cases. Note that forces acting on the boundary not only accelerate the centre of mass, but, depending on their direction and point of attack, also induce a moment around the centre of mass according to the moment of inertia I. We model environment interactions with a Newtonian kinematic impact law with inelastic collisions. This relates the pre-collision generalized velocity $\boldsymbol{u}^-$ to the post-collision velocity $\boldsymbol{u}^+$ by

$$\boldsymbol{u}^+ = \left(\mathbf{I} - \mathbf{M}^{-1}\mathbf{J}_c^T \left(\mathbf{J}_c\mathbf{M}^{-1}\mathbf{J}_c^T\right)^{-1}\mathbf{J}_c\right)\boldsymbol{u}^-, \tag{4.1}$$

with $\mathbf{I}$ the identity matrix, $\mathbf{M}$ the generalised mass matrix, and $\mathbf{J}_c$ the contact Jacobian (see also Chapter 2). Note that Equation (4.1) does not allow for slippage between the wheel and the environment, meaning that we do not have to model energetic losses due to friction. We will make extensive use of the collision matrix $\mathbf{M}_c$, which is used to map the pre-collision generalised velocities to the dissipated energy by

$$\Delta E = \frac{1}{2}(\boldsymbol{u}^-)^T\mathbf{M}_c\boldsymbol{u}^-, \tag{4.2}$$

with

$$\mathbf{M}_c = -\mathbf{J}_c^T \left(\mathbf{J}_c\mathbf{M}^{-1}\mathbf{J}_c^T\right)^{-1}\mathbf{J}_c. \tag{4.3}$$

4.2.2 Rotational Hopping Strategy

Figure 4.2 shows the off-centred wheel model for the rotational hopping strategy with the generalized coordinates $\boldsymbol{q} = [x, y, \phi]^T$ with respect to an inertial frame of reference, with x the horizontal position of the centre of mass, y the vertical position of the centre of mass, and ϕ the angular position of the body. The radius of the wheel is denoted by the parameter R and its eccentricity by a. Note that for all the calculations in this work, the eccentricity was set to half the radius $a = 0.5R$. The ground contact Jacobian is then

$$\mathbf{J}_c = \begin{bmatrix} 1 & 0 & R - a\cos\phi \\ 0 & 1 & -a\sin\phi \end{bmatrix}, \tag{4.4}$$

and the generalized mass matrix

$$.\mathbf{M} = \begin{bmatrix} m & 0 & 0 \\ 0 & m & 0 \\ 0 & 0 & I \end{bmatrix} \tag{4.5}$$

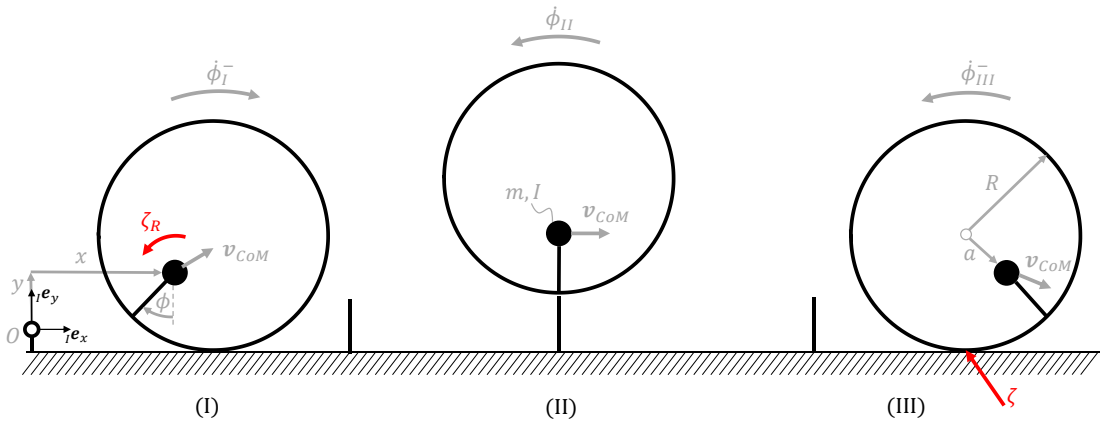

Fig. 4.2 **Rotational hopping model**. Generalised coordinates $\boldsymbol{q} = [x, y, \phi]^T$ with x the horizontal displacement from origin O, y vertical displacement from origin O, angular position ϕ, and system parameters mass m, moment of inertia I, wheel radius R, eccentricity a, and obstacle height h. (I) State just before impulsive actuation. The angular velocity of the system is reverted in a collisional event with angular impulse ζ_R from $\dot{\phi}_I^-$ to $\dot{\phi}_{II}$. The velocity v_{CoM} dictated by the rolling motion then leads to a ballistic flight phase. (II) Ballistic flight phase. (III) State just before impulsive energy loss due to impact ζ. Note that $\dot{\phi}_{II} = \dot{\phi}_{III}^-$

We now describe the mode of locomotion of this system as also shown in Figure 4.2. Given a forward speed u_x of our system at an angle ϕ, the generalized pre-take-off velocity is

$$\boldsymbol{u}_{TO}^- = k \begin{pmatrix} a\cos\phi - R \\ a\sin\phi \\ 1 \end{pmatrix}, \tag{4.6}$$

where $k = u_x/(a\cos\phi - R)$. Figure 4.2 (I) indicates that the centre of mass velocity $\boldsymbol{v}_{CoM}$ during rolling can point away from the ground, which we exploit for a ballistic flight phase. A flight phase is induced if the angular velocity is reverted in its direction in an instant, as this interrupts the rolling motion and causes the boundary of the robot to move away from the ground rather than staying on it. We induce this change by in impulsive angular event, gauged such that the wheel reaches the angle $\phi = 0$ at apex point. This condition is fulfilled, if the angular speed after impulse is exactly $\dot{\phi}^+ = -\phi^*/t_A$, where t_A is the flight time to apex

and ϕ^* is the take-off angle. The angular impulse does not influence the translational speed of the centre of mass at take-off, which means that a ballistic motion of the centre of mass with initial velocity as given in (4.6) provides $t_A = u^-_{TO,y}/g$. We now find an expression for the energetic cost to change the angular speed from pre-take-off to post-take-off speed by

$$\Delta E_R = \frac{I}{2}\left(\left(\dot{\phi}^+\right)^2 + \left(\dot{\phi}^-\right)^2\right) = \frac{I}{2}\left(\left(\frac{\phi^* g}{u^-_{TO,y}}\right)^2 + k^2\right). \tag{4.7}$$

The first term in the above equation is the cost to induce the required angular speed during flight phase, while the second term accounts for the braking energy required to stop the rolling motion. The impulsive actuation causes the wheel to hop over the obstacle without colliding with it. The only dissipative collision is the ground collision at touchdown. Since the ground is assumed to be flat and the flight phase symmetric, we have for the touchdown angle $\phi_{TD} = -\phi^*$, and the generalised velocity at touchdown

$$\boldsymbol{u}^-_{TD} = \begin{pmatrix} k(a\cos\phi - R) \\ -ka\sin\phi \\ -\frac{\phi^* g}{u^-_{TO,y}} \end{pmatrix}. \tag{4.8}$$

The energy loss at ground collision ΔE_C is then calculated using (4.2), where $\mathbf{J}_c(\phi = -\phi^*)$ is used for the Jacobian in (4.3) and $\boldsymbol{u}^-_{TD}$ for the generalised velocity. The total energy consumed to overcome the obstacle is the sum of energy required to induce the backward rotation at take-off plus any energy deficit of the final energy after touchdown as compared to the initial energy. We therefore write for the total energy consumed to overcome the obstacle with the rotational hopping strategy

$$\Delta E_H = r(E_0 - E_1) + \Delta E_R, \tag{4.9}$$

with $r(.)$ the ramp function, $E_0 = 1/2(\mathbf{u}^-_{TD})^T \mathbf{M}\mathbf{u}^-_{TD}$, and

$$\Delta E_1 = \frac{1}{2}(\boldsymbol{u}^-_{TD})^T \mathbf{M}\boldsymbol{u}^-_{TD} + \frac{1}{2}(\boldsymbol{u}^-_{TD})^T \mathbf{M}_c(-\phi^*)\boldsymbol{u}^-_{TD}, \tag{4.10}$$

In our analysis, we will require the wheel to overcome an obstacle of height h. This will influence the required take-off angle of the rotational hopping strategy. The obstacle will be surpassed if the ballistic motion of the wheel is such that the wheel rim won't touch the

obstacle, which is formulated with the following implicit equation

$$0 = 2g(1-a)\cos\phi + (ka\sin\phi)^2 - 2gh. \tag{4.11}$$

The solution will lead to the minimal take-off angle ϕ^* leading to a symmetric hopping strategy which surpasses the obstacle.

Note that we assume the wheel is horizontally placed at take-off such that it is exactly above the obstacle at apex point. This placement can lead to cases where the boundary of the wheel overlaps with the obstacle at take-off in the case of slow locomotion speeds. For the sake of simplicity, we do not model these interactions, and we assume that the obstacle has no effect on the hopping process.

4.2.3 Rolling Strategy

The collision of a rigid wheel with an obstacle is a classic problem in collision mechanics. We use the generalised rolling velocity before impact $\boldsymbol{u}_R = u_x[1,0,-1/R]^T$ which corresponds to a wheel with centred mass rolling on flat ground. The energy loss at collision can simply be obtained from the collision matrix with the Jacobian of the collision point

$$\mathbf{J}_c = \begin{bmatrix} 1 & 0 & R-h \\ 0 & 1 & -\sqrt{2Rh-h^2} \end{bmatrix}, \tag{4.12}$$

We assume the coefficient of restitution to be negligible, thus allowing for inelastic collisions. This gives the collision loss

$$\Delta E_{RC1} = \frac{1}{2}\boldsymbol{u}_R^T \mathbf{M}_c \boldsymbol{u}_R = -\frac{mu_x^2}{2}\frac{h(2mR^2 - Rhm + 2I)}{R(mR^2+I)}. \tag{4.13}$$

The impact on the flat ground after rolling over the obstacle is also considered in the theoretical prediction. Theoretical energy loss is easily obtained with the post-obstacle collision velocity $\boldsymbol{u}_p$ as

$$\Delta E_{RC2} = \frac{1}{2}\boldsymbol{u}_p^T \mathbf{M}_c^* \boldsymbol{u}_p, \tag{4.14}$$

With $\boldsymbol{u}_p$ given by (4.1) using $\mathbf{J}_c$ as defined in this section and $\boldsymbol{u}_R$, and $\mathbf{M}_c^*$ is formed by using a contact Jacobian for flat ground. This leads to the total energy loss of the rolling collision

$$\Delta E_R = \Delta E_{RC1} + \Delta E_{RC2}. \tag{4.15}$$

4.2.4 Trivial Hopping Strategy

For the trivial hopping strategy of the centred wheel, we apply a vertical impulse just before the obstacle, such that the wheel hops over it. The energy required for this strategy is equal to the potential energy to lift the wheel onto the obstacle

$$\Delta E_{HW} = mgh. \tag{4.16}$$

This energy is exactly lost during ground collision, so that the post-obstacle speed is identical to the initial speed. As in the case of the rotational hopping strategy, the wheel is horizontally placed at take-off such that it will hop over the obstacle at apex point. We do not model obstacle overlap due to this placement in the case of slow locomotion speeds.

4.2.5 Allometric Scaling Laws

The relation between hip height in running and hopping mammals and birds has been established using biological data [15],[111],[128]. The relation for radius to mass was found using linear regression in the logarithmic scales of mass and hip height. The residual least squares solution is

$$R = 0.2063\, m^{0.3720}, \tag{4.17}$$

with a coefficient of determination $r^2 = 0.821$. The result closely corresponds to findings for quadrupeds in [129]. We therefore employ the radius of gyration and leg mass found in [129] to deduce the moment of inertia of the leg around the hip joint. The radius of gyration is

$$R_{gy} = 0.047\, m^{0.33}, \tag{4.18}$$

and the leg mass

$$m_L = 0.107\, m^{1.03}, \tag{4.19}$$

which leads to a moment of inertia of one leg with respect to pivot point

$$I = 2 m_L R_{gy}^2 = 0.0004726\, m^{1.69}, \tag{4.20}$$

The factor 2 accounts for two legs swinging in the same direction as in the case of quadrupedal animals, from which the data was retrieved.

4.2.6 Experimental Set-Up

The model was tested using a simple experimental setup as is illustrated in Figure 4.3. The wheel consists of two wooden discs with a radius of $R = 0.2m$ and $5mm$ thickness which were rigidly connected with an $230 \times 13mm$ aluminium rod in the centre of the wheel. A payload was added on the centre of the rod to improve the mass to moment of inertia ratio, resulting in a mass of $m = 1.417kg$ and a moment of inertia of $I = 0.008kgm^2$. To realize the off-centred mass, the payload was transferred to a second rod placed at a distance of $R/\sqrt{2}$ from the centre of the wheel. This shifted the overall centre of mass roughly to $R/\sqrt{8}$ from the centre of the wheel. The modification led to a change in mass and inertia of $m_l = 1.495kg$ and $I_l = 0.01kgm^2$, respectively. Four reflective markers were placed on the outer face of one disc for the purposes of tracking the wheel motion. The wheel was then placed on one of four different heights on an aluminium ramp and released, which would accelerate the wheel to four pre-impact velocities before reaching a flat wooden track leading to the obstacle. Rubber sheets were fixed to the wooden flat track and metal ramp to guarantee the no-slip condition. The obstacle consisted of wood of 6mm thickness and was covered with a thin rubber sheet to reduce slip between the wheel and obstacle. Two obstacle heights ($3.6cm = 0.2R$ and $7.8cm = 0.4R$) were investigated as shown in Figure 4.8. After the obstacle, the flat wooden track covered with rubber strips continued to provide space for the collision after the obstacle was surpassed. For the hopping strategy, an impulse generator was installed, which consisted of a lever under the wooden track before the obstacle which would push against the track from below and lift a part of the track. To activate the lever, a weight of $1.5kg$ was dropped on the far end from a height no higher than the initial ramp position of the system. The dropping height was optimised manually until the required energy was achieved to overcome the obstacle at the tested speed. To track the motion of the wheel and to get an indication of the obstacle position an OptiTrack motion capturing system was used with 12 cameras placed around the testbed. Position data was tracked at a rate of $250Hz$ with a precision of around $1.5mm$ and velocities were derived numerically from position data. Pre-collision, flight phase, and post-collision states were obtained from the raw data to retrieve energy conditions and losses. Each pre-collision velocity – obstacle height combination was repeated until five successful samples were recorded.

In the experimental validation of the rotational hopping strategy, we only verify the ground impact energy loss, not the impulsive event at take-off. This is because the ground impact energy loss may be distorted by effects of ground-wheel interactions such as friction, which is not the case in the impulsive take-off event. We test the ground collision loss by throwing the wheel by hand and induce a retracting motion to overcome the obstacle. The energy loss over the impulsive event is then compared to the theoretical prediction according

to Equation (4.2), given the pre-touchdown velocity and touchdown angle. The position during flight phase, collision, and rollout phase were again tracked using the motion capturing cameras. The results are shown in Figure 4.9, where the prediction error is normalised with the total energy at touchdown and plotted as a function of the total energy at touchdown.

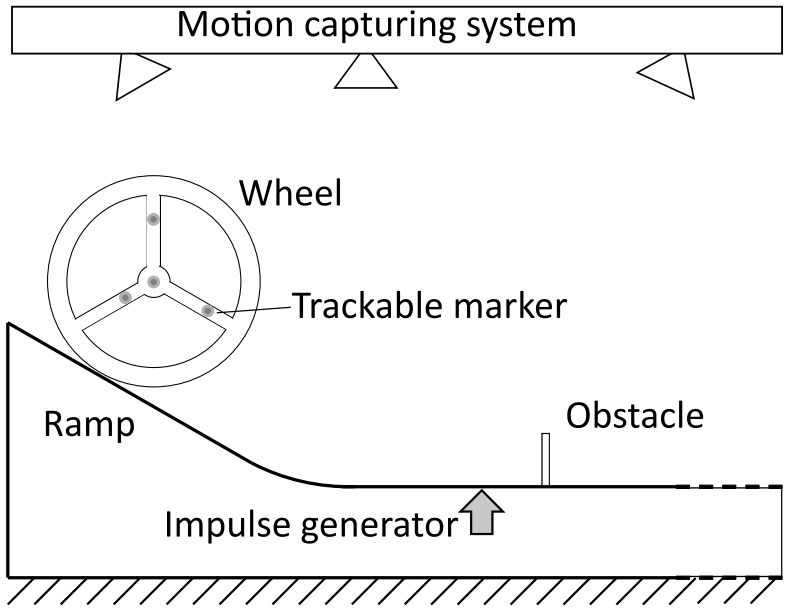

Fig. 4.3 **Experimental set-up**. Sketch of the experimental conditions. A wooden and rigid wheel-axle system is placed on top of a ramp, released, and guided towards an obstacle. Depending on the locomotion strategy, the system is either passively negotiating the obstacle or hopping over it by an impulse. The motion is recorded with a motion capturing system using four trackable markers placed on one face of the wheel.

4.3 Results

4.3.1 Theoretical Results of the Rotational Hopping Strategy

As shown in the methods section, hopping with the rotational hopping strategy as per Figure 4.2 comes with two energetic costs of different nature. The first cost is associated with the energy required to induce a retracting motion of the wheel according to eq. (4.7). This cost increases for short flight phases, as the required rotation velocity scales with the flight phase time. The second cost is due to the collision with the ground, which depends on the posture of the off-centred wheel and its velocity at touchdown. Figure 4.4 shows the two

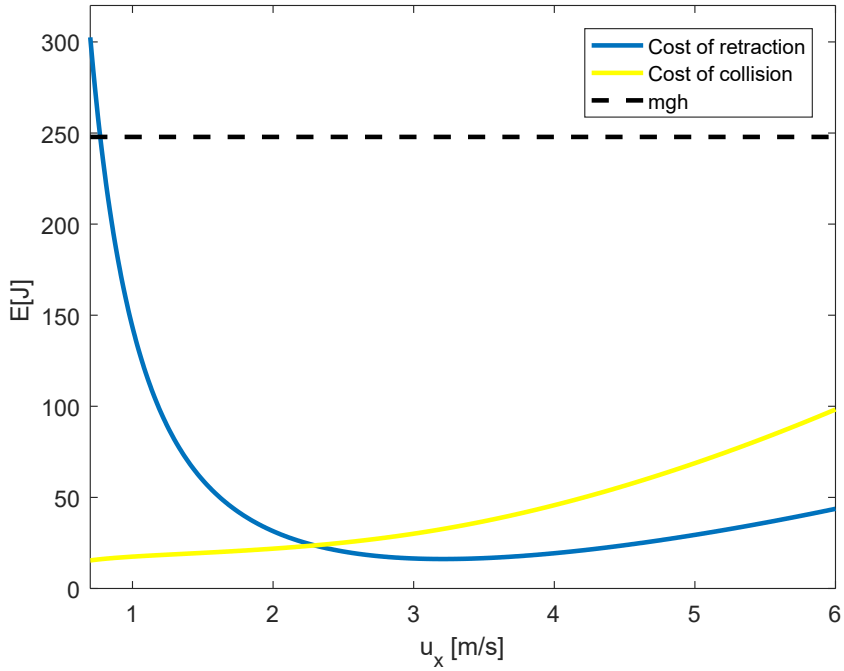

Fig. 4.4 **Costs for rotational hopping strategy**. The two terms of the energetic collision loss in Equation (4.9) as a function of forward speed. The blue line corresponds to the cost of retraction or rotation at take-off, and the yellow line corresponds to the cost associated with the collision at touchdown. The black dashed line indicates the trivial hopping strategy's collision loss, equal to mgh. The parameters are: mass $m = 80kg$, obstacle height of $h = 0.3R$, Radius $R = 1.05m$, moment of inertia $I = 0.78kgm^2$, and the take-off angle $\phi^* = -0.43rad$.

energetic costs of the hopping locomotion of an off-centred wheel as a function of locomotion speed. The wheel properties are defined for a mass of $m = 80kg$ and an obstacle height of $h = 0.3R$, Radius $R = 1.05m$, moment of inertia $I = 0.78kgm^2$, and the take-off angle which was found to be $\phi^* = -0.43rad$ by solving the implicit Equation (4.11). The parameters roughly correspond to a human subject and serve as an example. We see for the cost of retraction that a high cost occurs for low locomotion speeds, which is explained by the short flight phase time and take-off angle, increasing the first term of Equation (4.7). For higher speeds, this term becomes smaller, but the second term which accounts for the energy loss due to the required rolling-deceleration increases quadratically with locomotion speed. The presence of these two terms causes a minimum for the cost of retraction, slightly above $3m/s$. For the cost of collision, we see an increase towards higher locomotion speeds, which is explained by the dependency of collision loss with the quadratic form $\Delta E = \boldsymbol{u}^{-}\mathbf{M}_c\boldsymbol{u}/2$ in Equation (4.2). The collision loss is significantly lower in the displayed range than for the case of a wheel with centred mass which requires the potential energy mgh to overcome the

obstacle. This is due to the off-centred position of the wheel, and can be comprehended as follows: If the moment of inertia around the centre of mass was zero in the off-centred wheel, we could find a landing angle which causes no energy loss during collision. This angle is such that the touchdown velocity of the centre of mass is perpendicular to the vector pointing from centre of mass to ground contact point. In the case of systems with smaller moments of inertia as compared to their masses, this effect can reduce the collision losses as compared to a wheel with centred mass.

Figure 4.4 shows that for speeds higher than $3m/s$, the rotational hopping strategy predicts a cost of retraction of roughly $1/3$ of the energetic cost of collision, and collisional energy loss is $2/3$. In accordance with these findings, studies of running guinea fowls report swing leg costs of 26% of the total energy used for locomotion irrespective of locomotion speed [130], and a study for walking in humans predicts a cost of roughly 30% [131].

4.3.2 Mass-Independent Theoretical Results

The rotational hopping strategy depends on a low moment of inertia to exploit its advantages over other strategies. Surprisingly, we find that only if the moment of inertia scales with $I = \alpha m R^2$, i.e. the square of the radius, where we refer to the mass independent quantity $\alpha \neq \alpha(m)$ as the moment of inertia factor, the ratio of energy loss of rolling and hopping is independent of the mass, and solely depending on the Froude number $Fr = u_x^2/(gR)$ for legged locomotion (which is the square of the Froude number used in continuum mechanics) and the obstacle height h. Figure 4.5 shows regions of optimality as a function of the factor α, the Froude number, and obstacle heights between $h = 0.1R$ and $h = 0.5R$. We see that hopping is more efficient for higher Froude numbers and low values of α, while rolling dominates at low Froude numbers and a larger moment of inertia. The relative improvement of rotational hopping for higher Froude numbers and low moment of inertia factors is explained by the different costs associated with overcoming the obstacle. While the rolling strategy loses kinetic energy when colliding with the obstacle, the rotational hopping strategy has no costs associated with obstacle collisions. On the other hand, while the rotational hopping strategy requires the rotation of the wheel to be reversed to hop over the obstacle, the rolling strategy passively rolls over it. The energetic costs in the strategies scale differently as a function of Froude number and moment of inertia factor, which results in the depicted transition lines. These lines represent the section at which rolling and rotational hopping strategy have an equal energetic cost to overcome the obstacle. The effect of obstacle height on the optimal Froude number is more prominent for larger values of α, and appears to lose significance for lower values. The optimality transitions as a function of h also change their

shape first in favour of the rotational hopping strategies for $h = 0.1R$ to $0.2R$, and then in favour of the rolling strategy from $h = 0.3R$ to $0.5R$.

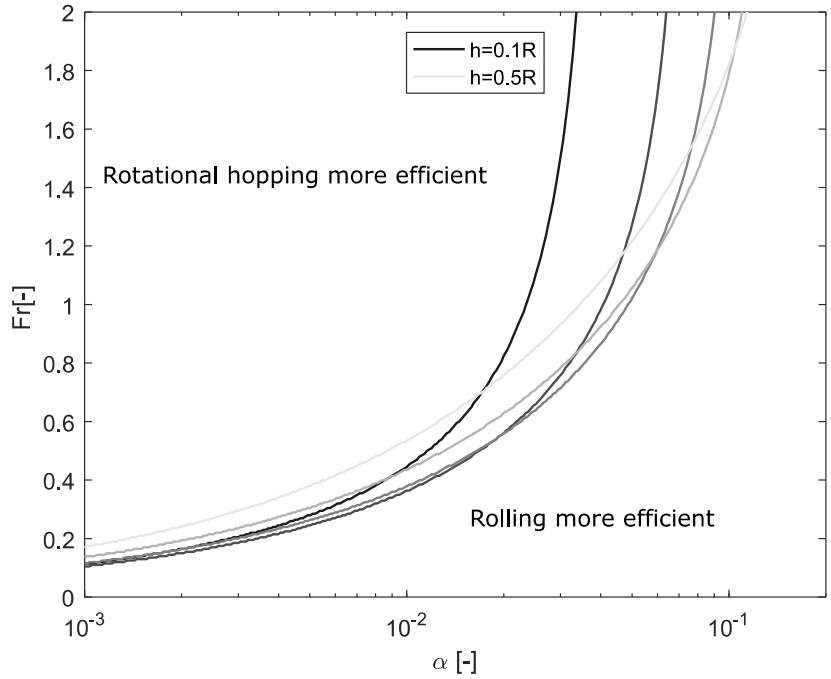

Fig. 4.5 **Comparison of rotational hopping strategy and rolling strategy**. Regions of strategies with least energy loss to overcome an obstacle of height h as a function of the moment of inertia factor $\alpha = I/mR^2$, and the Froude number $Fr = u_x^2/(gR)$. The results shown are independent of the mass of the wheel.

Note that Figure 4.5 provides results independent of wheel mass. It thus defines, depending on the wheel properties, whether it is better to roll or to hop over an obstacle of height h with locomotion velocity u_x.

4.3.3 Animal-Related Theoretical Results

Before we present the animal-related results in this section, the similarities of our model and legged animal locomotion need to be explained as they are not obvious. Legged locomotion is characterised by repetitive stance and possibly flight phases. The transition from one stride to the next is often accomplished over an impulsive event, in which energy is dissipated in the leg-ground collision. The leg is doing work to compensate for the collisional energy loss (and other losses) during the stance phase. The legs need to be swung back during the gait cycle to allow for a repetitive motion. Our rotational hopping model accounts for all the above as follows: flight and stance phase are both modelled; collisional energy loss is

modelled at flight-stance transition through inelastic collisions; energy deficit at the end of the cycle accounts for the work that needs to be done to reaccelerate to the initial wheel state; rotational motion is induced during flight to reset wheel posture. For the rolling strategy, the wheel-obstacle collision is identical to collisions as in the rimless wheel model for walking, which becomes obvious by drawing spikes from centre of mass to ground contact and obstacle contact in the rolling strategy obstacle collision. There are, of course, limitations of our simple collisional models to capture the complex energetics of legged locomotion. Many effects add to the complexity of legged locomotion, e.g. terrain properties, leg morphology and compliance, friction with the ground, etc., which are not captured by our simple model. The results presented in this section assume that legged animals are underlying the same physical laws of overcoming an obstacle as our wheel model and need to be interpreted with the above limitations in mind.

We now study the energetic costs for the three strategies to overcome an obstacle between $h = 0.1R$ and $h = 0.5R$. We assign animal properties to the wheel, by setting R to the animal leg length, m to its body mass, and I to the leg moment of inertia around the hip. The exact scaling laws are presented in the methods section. As the moment of inertia does not scale proportionally to the square of the radius as follows from Equation (4.20) (radius of gyration scales differently from leg length), the results now depend not only on the locomotion speed, but also on the mass. The energetics of the respective strategies are computed as described in the method section, with Equation (4.15) for rolling, (4.16) for trivial hopping, and (4.9) for rotational hopping. Figure 4.6a shows regions of optimal strategy as a function of body mass, locomotion speed, and obstacle height for the trivial hopping and rolling in terms of energy required to overcome an obstacle. We see that rolling dominates lower speeds and performs better at higher body masses. The lower the obstacle height, the better the hopping strategy performs. Indeed, we can study the limit case for which the obstacle height vanishes, and find that optimality transition from rolling to hopping occurs at a Froude number of 1, with $Fr = u_x^2/(gR)$. A simulation study of gait transitions with energy optimality objective [11] reached a similar conclusion, stating that running is preferred over walking for vanishing step lengths at a Froude number larger than one. Vanishing step lengths would correspond to infinitesimal obstacle heights in our model.

Figure 4.6b shows the rotational hopping strategy and its optimality transitions from rolling to hopping for the same obstacle heights and mass/locomotion speed as in 4.6a. We see that even though rolling is still superior to hopping for low locomotion speeds, the rotational hopping strategy takes over optimality at lower speeds than in the trivial hopping case. Figure 4.4 already hinted toward this observation, by the rotational strategy's lower energetic losses. We would like to point out that the improved performance is dependent

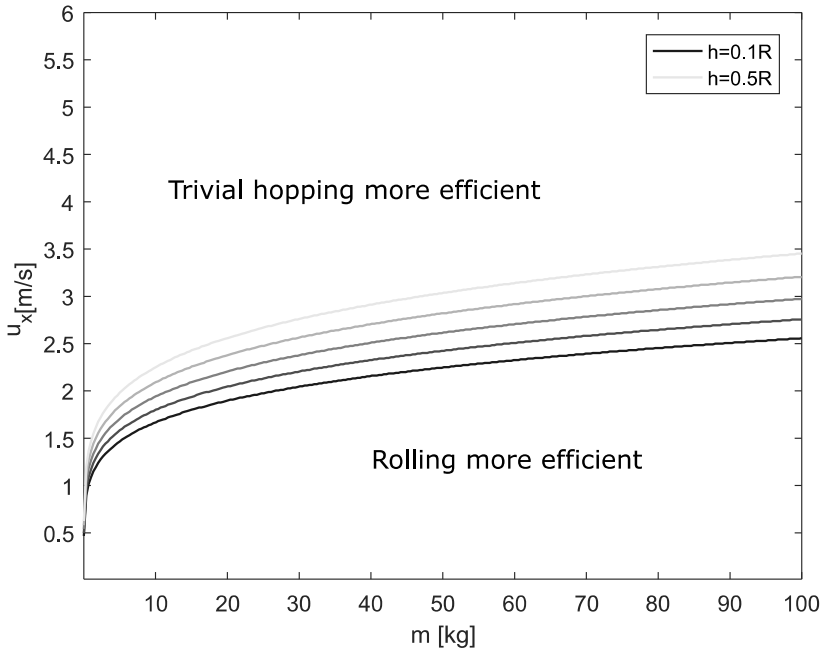

(a)

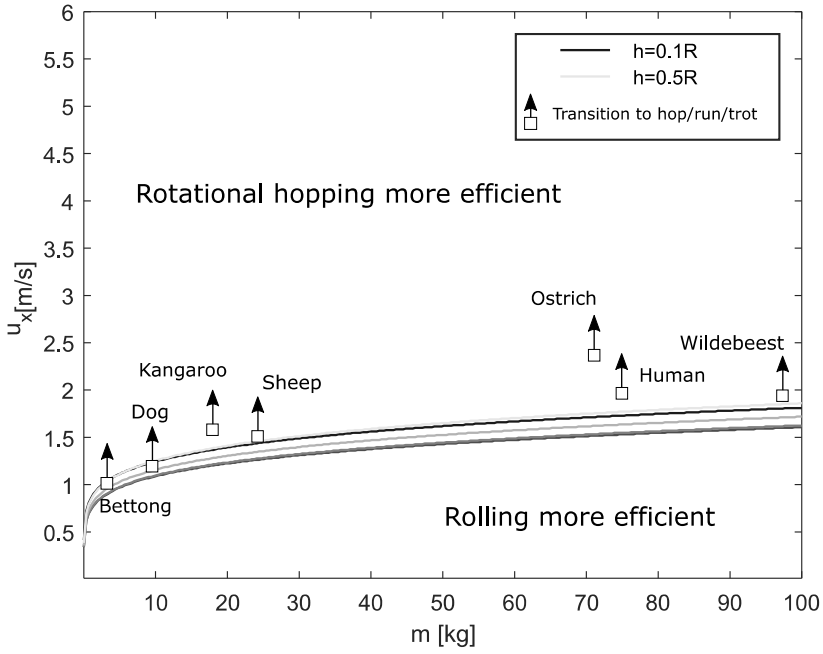

(b)

Fig. 4.6 **Strategy comparison for animal related parameters**. Regions of optimal strategies as a function of body mass m, locomotion speed u_x, and obstacle height h. Parameters are set using the allometric relations (4.17)-(4.20), which scale the wheel radius R such that it corresponds to the animal leg length, the point mass m corresponds to animal body mass, and the moment of inertia around the centre of mass I corresponds to leg moment of inertia around the hip. **a**, Rolling strategy compared to trivial hopping strategy and their optimal regions. **b**, Rolling and rotational hopping strategy and their optimal regions. Walk to hop/run/trot gait transitions for various animals are indicated [132], [133], [134] [135].

on our allometric scaling law of moment of inertia with body mass m. As we have seen in Figure 4.5, the optimality transitions are independent of mass if the moment of inertia factor α is of the form I/mR^2. Since this is not the case in the allometric relations (4.17)-(4.20), this is not exactly true. We find, however, that for the allometric scaling law of leg moment of inertia (4.20), the optimality transition happens above a Froude number of $Fr = 0.3$, only slightly varying with body mass. This is in close correspondence with experimental findings in quadrupedal animals [136]. As we scaled the moment of inertia of the wheel with the moment of inertia of animal's legs, we indicated transition speeds from walking gaits to hopping, running, or trotting for various animals, and we observed that they seem to follow the optimality transition.

4.3.4 Experimental Results

For validation of our model assumptions, we constructed an experimental test platform as shown in Figure 4.3 and explained in detail in the methods section. Figure 4.7 shows the motion progression for the three locomotion strategies in experiment. In the simple case of

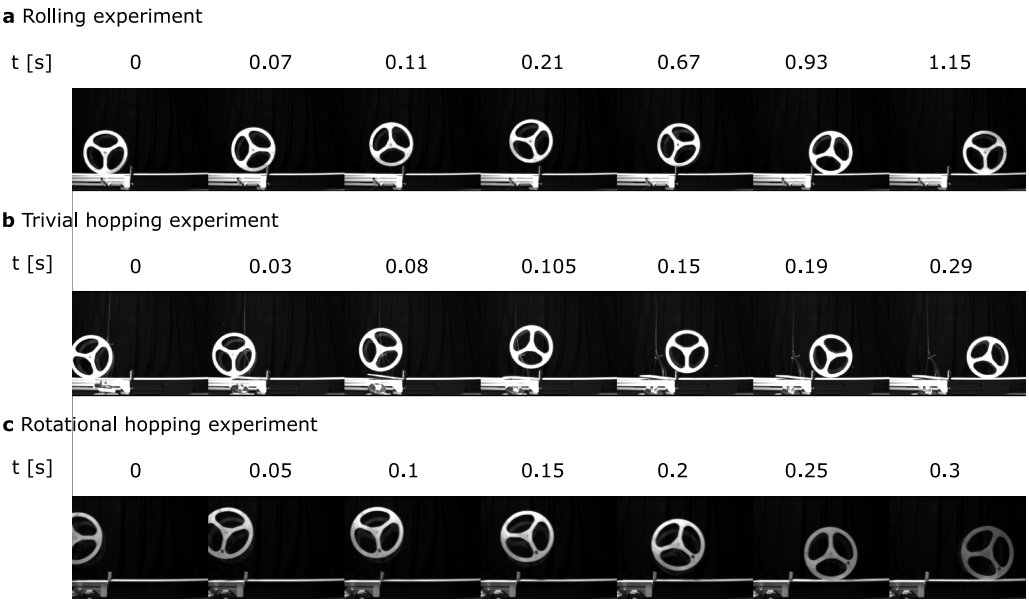

Fig. 4.7 **Motion progression of experimentally tested strategies**. **a**, motion progression of the rolling experiment at an approach speed of $1.8m/s$. **b**, motion progression of the trivial hopping experiment at an approach speed of $1.9m/s$. **c**, motion progression of the rotational hopping experiment by throwing the wheel. Approach speed corresponds to $2m/s$.

the centred wheel, we performed a controlled set of experiments to assess the collisional energy losses as explained in detail in the methods section. The results for two different

obstacle heights as a function of the kinetic and potential energy before the obstacle collision are shown in Figure 4.8, along with the theoretical predictions of the model. The variance arises mainly due to noise in the measurements and the numerical derivative to obtain system velocity, but may also stem from ignored effects such as damping, friction, and the omitted lateral dimension. The impulse generator created variations in hopping heights, which was accounted for in post-processing by subtracting the gap potential energy arising due to the distance between wheel apex height in flight phase and obstacle height. Measurement noise and possible elastic restitution at touchdown may have caused the energy loss to fall under the predicted value in some cases. The results show that optimality transition of both theory and experiment occur at around the same initial energy, i.e. approach speed, which validates our model assumption that collisions are the dominant energetic loss during the process of overcoming the obstacle. For the case of the off-centred wheel, we assessed the accuracy

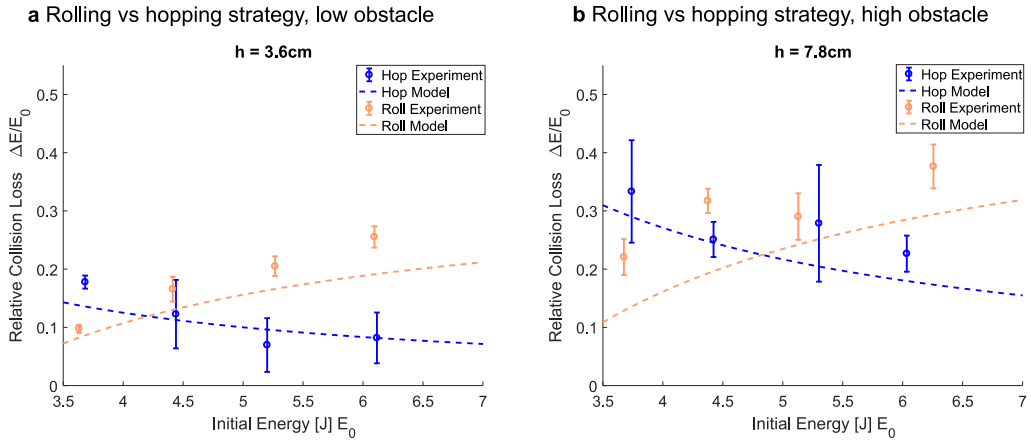

Fig. 4.8 **Experimental collision loss for rolling and trivial hopping strategies**. **a**, Energy loss of rolling strategy and trivial hopping strategy as a function of pre-collision energy for an obstacle height of $0.18R$. Error bars indicate one standard deviation over five experiments. **b**, Energy loss of rolling strategy and trivial hopping strategy as a function of pre-collision energy for an obstacle height of $0.39R$. Error bars indicate one standard deviation over five experiments.

of the energy saving mechanism at collision as predicted by the quadratic form (4.2). The simplest validation is to throw the wheel to land at different touchdown angles and speeds, and comparing the experimental losses with the theoretical prediction. Figure 4.9 shows the relative error of the predicted energy loss at collision divided by the total energy at touchdown, as a function of the total energy at touchdown. The total energy is the sum of kinetic and potential energy, and the relative error is the theoretical predicted energy loss minus the experimental energy loss. As shown by the results, the experimental losses tend to

be larger than the theoretical prediction, which we explain by non-modelled internal losses in the system and friction. The results show that the collisional model of the off-centred wheel can provide accurate predictions of energy loss in experimental conditions. This ensures that the predictions in Figure 4.4, where we claimed that the off-centred wheel can significantly reduce energetic collision losses as compared to the case of the centred wheel, are valid.

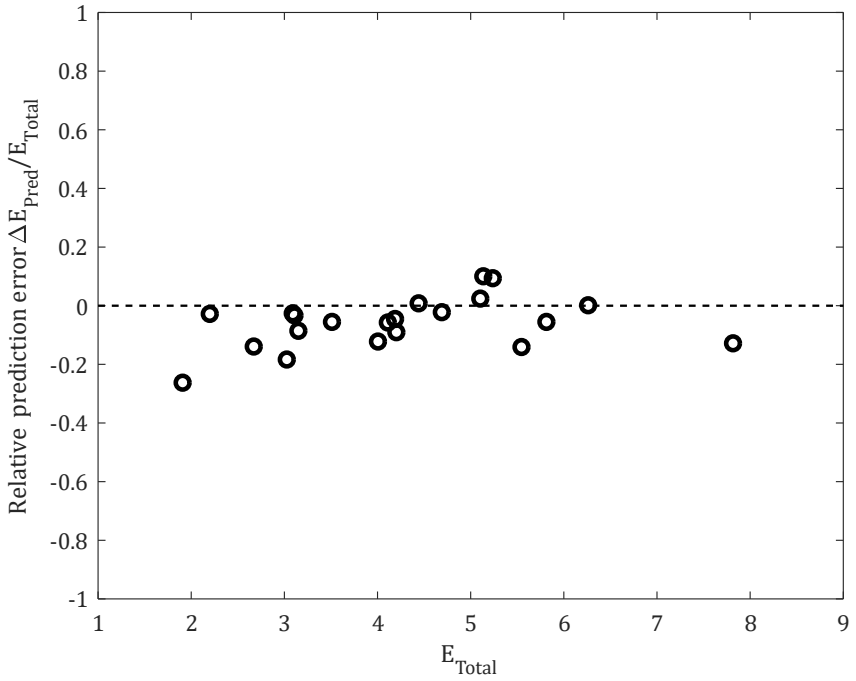

Fig. 4.9 **Prediction error of energetic collision loss for rotational hopping strategy**. The off-centred mass wheel was thrown over the obstacle, and the touchdown position and velocity state was used to predict theoretical loss ΔE_{Theor}, which was compared to the experimental loss ΔE_{Exp} to give the prediction error ΔE_{Pred}. The value is normalized with the total energy at touchdown $E_{Total} = E_{Kin} + E_{Pot}$.

4.4 Discussion

In this work, we have studied the task of a wheel overcoming an obstacle. Because wheels are generally studied in the context of rolling, we aimed to find out if strategies like hopping can be energetically advantageous in this context. Based on collisional mechanics, we have analysed three strategies, namely the rolling strategy, the trivial hopping strategy, and the rotational hopping strategy. Collision based models which study impulsive transitions of the centre of mass [51], [123], [124], [10], are powerful tools to understand the underlying

physical principles of locomotion, but more complex models might explain effects which are not covered by the simple representation [113]. In this spirit, the inclusion of mass distribution represented by the moment of inertia around the centre of mass, as presented here, was a necessary model extension to find the rotational hopping strategy. Due to this enhancement of the model, we found that the trivial hopping strategy (which is unaffected by the moment of inertia) is not necessarily the most energy-effective in the task of overcoming an obstacle, but, as shown in Figures 4.4 and 4.6, that the rotational hopping strategy is superior over a wide range of parameter values.

We provided quantitative results that show at which point a wheel better hops than rolls over an obstacle as a function of the Froude number, of the ratio $\alpha = I/(mR^2)$, and of the obstacle height. The three tested locomotion strategies underlie different sources of energetic cost. The passive rolling strategy collides with the obstacle, the trivial hopping strategy requires the fixed energy mgh to be lifted over the obstacle, and the rotational hopping strategy uses a backward rotation to retract its boundary to clear the obstacle and has a reduced collision at touchdown due to the eccentricity of the wheel. Although the strategies are different, a comparison of the collisional losses reveals that the advantage of hopping over rolling as shown in Figure 4.5 is independent of mass m, and can distinctly be determined by only the Froude number and moment of inertia factor α for a given obstacle height h. The energetics of the three strategies therefore uniquely determine the best way to overcome an obstacle given wheel size, speed, mass distribution, and obstacle height.

The results shown in Figure 4.6 presented velocity regions of advantages for hopping over rolling strategies for a wheel with the same size, mass, and mass distribution as hopping and trotting animals have. The results show that animal gait transitions from walking to hopping locomotion occur around the boundary from advantages in hopping to rolling. These results point to similarities between the wheel roll-hop transition and gait transitions in legged animals. One aspect which relates to both systems is the cost to retract the wheel or leg. During flight phase of the wheel model, as seen in Figure 4.4, the cost to induce the retracting motion at higher locomotion speeds is around 30%. Similar findings were presented for the energetic cost of swing leg retraction in animals [137],[138], and results obtained with mechanical models as in [92],[126] further highlight the importance of modelling swing leg retraction in legged locomotion energetics. Furthermore, the rotational hopping strategy also allows for a redirection of centre of mass after touchdown, which costs no energy due to the smooth rolling transition of the wheel. This effectively results in a trajectory like that in spring-mass models for locomotion [12].

As indicated in [13] and [122], walking energetics can be modelled with a rimless spoked wheel, where the legs are interpreted as spokes. The rolling collision loss studied here is

indeed identical to the spoked wheel collision, as revealed by a simple rotation of the system (the effect of gravity is negligible over a collisional event). If walking therefore is associated with the same collisional energy loss as rolling, Figure 4.6b may explain why animals change their gaits at the transition where hopping becomes more advantageous than rolling. Note that this is only true, however, if the rotational hopping strategy presented in this work does capture the correct energetic costs as found in legged animals. If so, the leg, through walking, may incorporate advantages of rolling at slow speeds, and of hopping at faster speeds. Based on the premise of environments with obstacles and the objective to minimise energy, the wide use of legged hopping rather than rolling in nature seems reasonable.

Our results need to be interpreted with consideration of the model assumptions. A simple obstacle may not completely represent the complexity of natural environments, and legs can certainly exploit more subtle effects than a rigid wheel. Nevertheless, we showed the conditions at which hopping outperforms rolling strategies to overcome an obstacle in a wheel, and we largely verified the energetic loss predictions in experiments. The results state that if the moment of inertia of the body is small, the superiority of hopping becomes apparent even at low locomotion speeds. The slender legs of animals hint toward a design in nature to reduce leg moment of inertia, possibly to exploit the same physical effects as studied in the wheel model. In the next chapter, we explore if the rotational impulses to induce the rotational hopping strategy can be implemented in robotic systems to define a novel mode of locomotion.

Chapter 5

Rotational Impulses for Robot Locomotion[1]

The theoretical predictions for hopping locomotion based on discrete actuation were studied in Chapters 3 and 4. In this chapter, we further investigate the locomotion dynamics by focusing on stability, the shape of the system, and a particular impulse which acts in the angular degree of freedom. The proposed mode of locomotion suggests a novel locomotion system, which we analyse in this chapter. In addition, this chapter presents the first robot implementation of discrete actuation and we show how the framework can lead to novel locomotion mechanisms for robotics.

5.1 Introduction

Actuation in hopping and jumping robots presents one of the major challenges to build efficient and robust hopping machines. Raibert introduced hopping and running robots using hydraulics, compressed air [86], and combustion engines to supply the required forces for high-speed and robust locomotion [139]. These methods however require heavy actuators or need to be remotely supplied with energy. Animals appear to avoid this disadvantage by employing spring-like behaviour in muscles and tendons [140], [141], which has inspired

[1]This chapter presents the collaborative work with my supervisor F. Iida. I have initiated the problem statement, derived the theoretical equations, designed and built the robot *Robbit*, conducted, planned and prepared the experiments, and wrote the paper. F. Iida helped discussing and revising the paper. The manuscript which is published in the *IEEE Transactions on Robotics* and which forms the basis of this chapter is

- Fabio Giardina and Fumiya Iida. Efficient and stable locomotion for impulse-actuated robots using strictly convex foot shapes. *Transactions on Robotics*, doi: 10.1109/TRO.2018.2813359, 2018.

engineers to develop smarter actuation mechanisms such as series [142] or parallel elastic actuation [36].

Recently, there has appeared a trend of research that studies hopping and jumping robots with impulsive actuation. Elasticity-stored impulses (ESI) are used in robots like the EPFL jumper [77] where a rapid change from standing to ballistic motion is realised with a 4 bar linkage and a torsion spring. Based on a similar design, the robot Salto [78] is furthermore capable of redirecting its posture during flight phase for a controlled second jump, easily timed due to the impulsive nature of the actuation. These types of jumping robots are considered beneficial for celestial exploration [143].

Based on a different mechanism, momentum-stored impulse (MSI) actuators store impulsive energy in a rotating flywheel. The robot Cubli [144] uses the MSI to lift a cube lying on its face onto one of its edges or vertices, using the flywheel thereafter to balance the cube. Space roboticists have exploited this actuation method for exploratory ventures in unknown environments [145], using impulses for locomotion in low-gravity environments. Similarly, the 3D M-blocks [146] make use of angular impulses to overcome the magnetic potential of their locking mechanism and reconfigure themselves into new structures.

The obvious advantage of impulses is their ability to propel a system over great obstacles as demonstrated for instance by the *sand flea* robot [147]. Exploiting the accuracy of impulsive actuation furthermore helps to plan a precise landing point. Space robots exploit this property to reach targets in complex and unknown environments by planning a sequence of jumps. A more subtle but no less important advantage of impulsive actuation is its intuitive effect: an impulse applied at a specific point in time changes a system's velocity instantaneously. No integration of the system dynamics needs to be performed to know the outcome of an actuation. This property enables fast trajectory prediction and therefore control decisions to be made, which is shown in the agile motion of Salto [78].

Despite the importance of impulsive actuation, the approach was explored neither for periodic locomotion nor for economical use of impulses. To maintain or improve locomotion speed given an impulse, it is important to control the stance phase dynamics. The simple and intuitive actuation with impulses should, however, not be tainted with complex sensory feedback. Ringrose [40] argues that a robot with a curved foot can be self-stabilised, meaning that no active feedback control is necessary for stable locomotion. Based on this principle, we have been exploring the influence of strictly convex foot shapes on hopping locomotion in robots like *Cargo* [39]. We found not only that stable and periodic locomotion can be achieved without any feedback control, but also that we can greatly decrease the energetic cost of locomotion. The intuitive stabilising properties of strictly convex shapes therefore lend themselves as an ideal match for impulsive actuation.

In this chapter, we explore the effect of strictly convex foot shapes on the locomotion performance of impulse-actuated systems in terms of speed and economic use of impulses, and compare the results to the theoretical performance of an MSI actuated cube. We first present tools to understand the effect of shape on the dynamics in a theoretical model, and then study the predictions in the case of a disc with an off-centred mass actuated by MSI in simulation. We further present a real world implementation with the robot *Robbit* to validate our findings.

The remaining chapter is structured as follows: Section 2 introduces the modelling approach and the control for locomotion with impulsive actuation and strictly convex shapes. Section 3 presents methods used to find limit cycles, proof of stability, and the results of the system's locomotion performance. Section 4 introduces the robot *Robbit*, designed using MSI actuation and a strictly convex shape of a disc with an off-centred mass. Experimental results and comparison with the simulation model are presented in Section 5. Section 6 discusses the results, and Section 7 concludes the chapter.

5.2 Locomotion Model

The locomotion model presented here is defined using standard planar rigid body dynamics. That is, the rigid body considered is completely defined by its total mass, moment of inertia with respect to the centre of mass, the centre of mass, and its boundary or strictly convex shape $\boldsymbol{s}(\varphi)$, which defines the set of points of interaction with the environment as a function of the angular parameter φ as shown in Figure 5.1. Strict convexity, which is a property of the shape $\boldsymbol{s}$ if $\boldsymbol{s}^T \frac{d^2\boldsymbol{s}}{d\varphi^2} < 0 \quad \forall \varphi \in [-\pi, \pi]$, is required to distinguish the studied systems from polygons, which cannot roll without impacts. We furthermore assume a planar model, as the presented locomotion mode does not depend on the lateral dimension.

5.2.1 Constrained Equations of Motion

We would like to point out that we assume a no-slip condition at this point to simplify analysis. As explained in more detail later, the results presented in Section 5.3.3 will consider friction of the Coulomb type for the prediction of robot performance. We implement interactions by specifying kinematic constraints *a priori*, and solve the resulting equations to find the enabling forces. We will denote with $\boldsymbol{q} = (x, y, \phi)^T$ the generalised coordinates with x and y the coordinates of the centre of mass with respect to the inertial frame of reference I located at origin O and ϕ the angular rotation of the body fixed frame of reference S with respect to I. We enforce the rolling constraint by requiring that the relative velocity between the ground

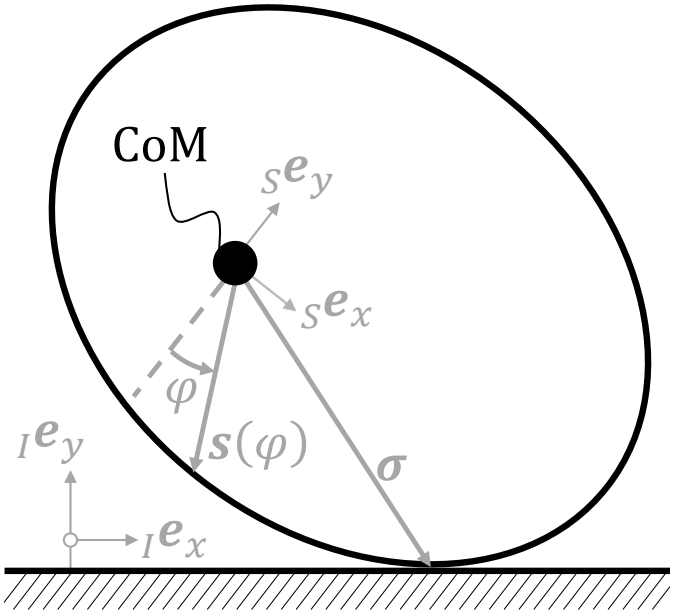

Fig. 5.1 Definition of shape $\boldsymbol{s}$ as a function of the parameter φ, and contact function $\boldsymbol{\sigma}$ as a function of the system state ϕ. I is the inertial frame of reference, and S is the chosen body-fixed frame of reference.

contact point on the robot and the ground vanishes, i.e.

$$\mathbf{J}_c\,\dot{\boldsymbol{q}} = \begin{pmatrix} \dot{x} - \sigma_y(\phi)\dot{\phi} \\ \dot{y} + \sigma_x(\phi)\dot{\phi} \end{pmatrix} = \mathbf{0}, \tag{5.1}$$

with $\mathbf{J}_c$ the Jacobian of the ground contact and $\dot{\boldsymbol{q}}$ the generalised velocity. We will refer to the vector function $\boldsymbol{\sigma} = (\sigma_x, \sigma_y)^T$ as contact function, as it represents the vector pointing from the centre of mass to the current contact point. After defining the kinematic constraints on acceleration level, we can use Gauss's principle to enforce the constraints via Lagrangian multipliers in the equations of motion. The equations of motion of the constrained system with possible external force $\boldsymbol{h}$, that includes also the gravitational force, read

$$\mathbf{M}\,\dot{\boldsymbol{u}} = \boldsymbol{h} + \mathbf{J}_c^T\,\boldsymbol{\lambda}, \tag{5.2}$$

where $\mathbf{M}$ is the generalised mass matrix, and $\boldsymbol{u} = \dot{\boldsymbol{q}}$ the generalised velocity. The Lagrange multipliers are found by combining (5.2) and the derivative of (5.1)

$$\boldsymbol{\lambda} = -\left(\mathbf{J}_c\mathbf{M}^{-1}\mathbf{J}_c^T\right)^{-1}\left(\mathbf{J}_c\mathbf{M}^{-1}\boldsymbol{h} + \boldsymbol{\xi}\right), \tag{5.3}$$

with $\boldsymbol{\xi}$ the gyroscopic terms which arise due to the kinematic constraints.

5.2.2 Impulsive transitions

We employ a Newtonian kinematic impact law in normal direction with coefficient of restitution $\varepsilon = 0$ to model inelastic impacts. We model tangential impacts also with a coefficient of restitution $\varepsilon = 0$ and assume a no-slip condition. This avoids the effects of friction and tangential compliance and simplifies the governing dynamics of the locomotion mode presented in the next subsection. More specifically, we require during this impulsive event

$$\dot{\boldsymbol{g}}^{+} + \mathbf{E}\dot{\boldsymbol{g}}^{-} = \mathbf{0}, \tag{5.4}$$

where $\mathbf{E} = \mathbf{0}$ is the diagonal matrix of coefficients of restitution, $\dot{\boldsymbol{g}} = \mathbf{J}_c \dot{\boldsymbol{q}}$ is the contact point velocity, and we use the superscripts $+$ and $-$ to indicate post-contact and pre-contact conditions, respectively. The requirement (5.4) then leads to a post-contact velocity

$$\boldsymbol{u}^{+} = \left(\mathbf{I} - \mathbf{M}^{-1}\mathbf{J}_c^T \left(\mathbf{J}_c\mathbf{M}^{-1}\mathbf{J}_c^T\right)^{-1}\mathbf{J}_c\right)\boldsymbol{u}^{-}, \tag{5.5}$$

which defines the transition behaviour from unconstrained to constrained equations of motion in terms of velocity. Note that the transition of generalised coordinates $\boldsymbol{q}$ is smooth and does not change over the impulsive event.

To transition from constrained to unconstrained equations of motion we do not require any kinematic conditions, except that the impulsive force applied to the system is causing the ground contact point to have a velocity component which is pointing away from the ground. In other words, if we apply an impulse $\boldsymbol{\zeta}$, we only need to satisfy the condition

$${}_I\boldsymbol{e}_y^T\mathbf{J}_c\boldsymbol{u}^{+} = {}_I\boldsymbol{e}_y^T\mathbf{J}_c\mathbf{M}^{-1}\boldsymbol{\zeta} + {}_I\boldsymbol{e}_y^T\mathbf{J}_c\boldsymbol{u}^{-} > 0, \tag{5.6}$$

where ${}_I\boldsymbol{e}_y$ is the unit vector in vertical direction of the inertial frame of reference I, as indicated by the left subscript.

5.2.3 Locomotion with Strictly Convex Shapes

We now describe the method for locomotion using strictly convex shapes. Inertial properties of the system are mass m_S and moment of inertia I_S with respect to the centre of mass. The position of the centre of mass is indicated by the generalised coordinates x and y, in horizontal and vertical direction, respectively. We apply a torque T in an arbitrary point P, as indicated in Figure 5.2 (I), causing an accelerated motion in form of rolling around

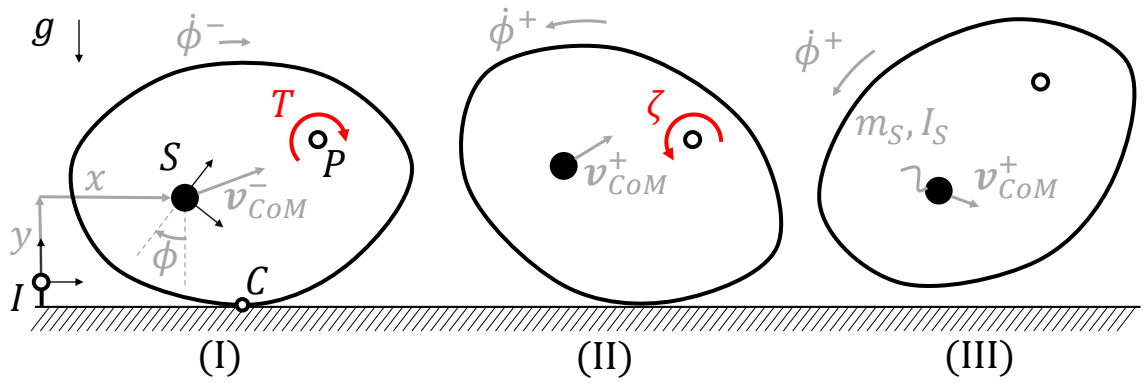

Fig. 5.2 Locomotion of arbitrary strictly convex shape through momentum-stored impulse. (I) Rigid body with centre of mass S and generalised coordinates $\boldsymbol{q} = (x, y, \phi)^T$ is actuated with a constant torque T around arbitrary point P. The current angular velocity $\dot{\phi}^-$ is such that the system rolls instantaneously around contact point C, causing a centre of mass velocity $\boldsymbol{v}^-_{CoM}$. (II) An angular impulse $\zeta = T \times t_S$, with t_S the stance phase time, instantaneously changes the angular velocity to $\dot{\phi}^+$ and induces a flight phase. Note that the centre of mass translational velocity is not affected directly by the angular impulse. (III) During flight phase, no torque is applied. The system with mass m_S and moment of inertia around the centre of mass I_S is only influenced by gravitational acceleration g.

contact point C. The centre of mass trajectory of the system is constrained by the shape and is always perpendicular to the contact function $\boldsymbol{\sigma}$ during stance phase. Note that due to the strict convexity of the shape, the body rolls over the ground without any collisions.

To induce flight phase, we need to apply an impulsive force as defined by (5.6). Here we come to the central property of this mode of locomotion. The torque T which has accelerated the system must have generated the angular momentum $L = T\,t_S$ as a result of the reaction torque in point P, t_s being the time for which the constant torque T was applied to the body. We exploit this angular momentum and assume that we can transfer it in an inelastic collision to the main structure. A possible outcome of such an event is indicated in Figure 5.2 (II). The impulse causes an angular velocity which is opposite in direction to the stance phase, hence causing a backward rotation which leads to a flight phase (III).

We assume the reaction torque has acted on a flywheel located in point P with moment of inertia I_R with respect to P. The angular velocity of the flywheel after time t_S under constant torque T is then

$$\dot{\phi}_R^- = \dot{\phi}_{R,0} + \frac{T\,t_S}{I_R}, \tag{5.7}$$

With $\dot{\phi}_{R,0}$ its initial angular speed. For the transfer of impulse, we exploit conservation of angular momentum which results in an expression for the post-impact angular velocity of the

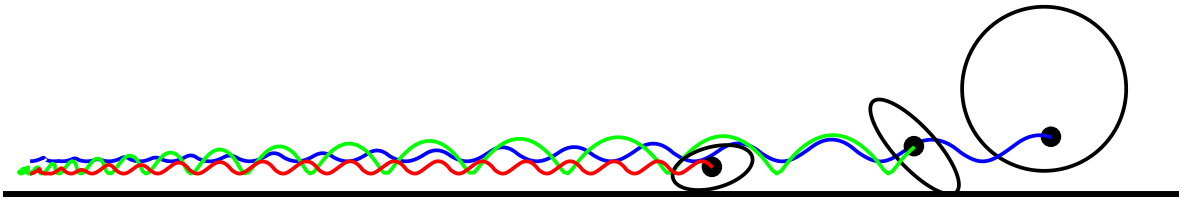

Fig. 5.3 Diversity of hopping behaviour for different shape functions in simulation. The blue trajectory corresponds to the off-centred disc with radius $R = 0.2$m and eccentricity $a = R/2$, the green trajectory to an ellipse with semi-major axis $0.75R$ and semi-minor axis $0.25R$, and the red one for an ellipse with semi-major axis $0.5R$ and semi-minor axis $0.25R$. Actuation for all three cases is $T = 0.38\,\mathrm{Nm}$ and impulse limit $\zeta_0 = 0.052\,\mathrm{Nms}$.

main body

$$\dot{\phi}^+ = \frac{\dot{\phi}^- I_S + \dot{\phi}_R^- I_R}{I_S + I_R}. \tag{5.8}$$

The transferred impulse is then simply derived by

$$\zeta = I_S \left(\dot{\phi}^+ - \dot{\phi}^- \right). \tag{5.9}$$

We can now define a control method to induce hopping in strictly convex shapes with momentum-stored impulse actuation. We define the control parameters constant torque T and impulse limit ζ_0, and start in stance phase, i.e. with the constrained equations of motion (5.2) and a system state $\boldsymbol{q}_0$ which comply with the ground contact conditions. First, the constant torque is applied onto the system, accelerating both the main body and the flywheel, until the impulse (5.9) reaches the impulse limit ζ_0. Subsequently, momentum between the flywheel and the main body is exchanged, causing a backward rotation and inducing flight phase. No torque is applied during flight phase. Once any shape point coincides with the ground, an impact forces the transition from flight to stance, initiating a new cycle by applying the constant torque T.

We have tested this control method for various shape function in simulation as shown in Figure 5.3, highlighting how this simple control law generates stable locomotion trajectories for randomly chosen strictly convex shapes. Note that the three illustrated cases are controlled with exactly the same control law and inertial parameter values.

Table 5.1 Parameter ranges for simulation and robot.

	Parameter	Symbol	Value
Generalized coordinates	Horizontal position	x	$[-\infty, \infty]$ m
	Vertical position	y	$[0, \infty]$ m
	Angular position main body	ϕ_S	$[-\pi, \pi]$ rad
	Angular position flywheel	ϕ_R	$[-\pi, \pi]$ rad
Experiment & simulation fixed parameters	Foot radius	R	0.2 m
	Eccentricity	a	0.1 m
	Mass main body	m_S	0.974 kg
	Mass flywheel	m_R	0.431 kg
	Moment of inertia main body	I_S	$3.004 \cdot 10^{-3}$ kg m^2
	Moment of inertia flywheel	I_R	$1.543 \cdot 10^{-3}$ kg m^2
	Gravitational acceleration	g	9.81 $\frac{\text{m}}{\text{s}^2}$
	Coefficient of restitution	ε	0 [−]
Experiment control $\beta = \{T, \zeta_0\}$	Torque	T	$[0.1, 0.3]$ N m
	Impulse limit	ζ_0	$[0.04, 0.07]$ Nms

5.3 Stability of Locomotion

The subsequent analysis is applied to a shape defined by a disc with an off-centred mass, where R denotes the radius of the disc, and a stands for the eccentricity of the centre of mass, measured from the midpoint of the disc. This description simplifies the contact function to

$$\boldsymbol{\sigma}(\boldsymbol{q}) = \begin{pmatrix} -a\sin(\phi) \\ a\cos(\phi) - R \end{pmatrix}. \tag{5.10}$$

The numerical parameters of the system are given in Table 5.1. The applied control sequence is as described in the previous section.

In the next step, we investigate if this control strategy, together with the defined contact function (5.10), can lead to periodic solutions corresponding to continuous locomotion.

5.3.1 Finding Periodic Solutions

Periodic and continuous motion, i.e. a motion which maps the take-off state back to itself after one cycle of stance and flight phase, improves the performance of impulse-actuated systems. If we look at the Poincaré section at the pre-take-off position, the system (without the flywheel) can be completely defined by its angular velocity $\dot{\phi}$ and its posture ϕ due

to the fact that the centre of mass follows a trajectory predefined by the contact function. Given angle and angular velocity at take-off, the trajectory until the next take-off point is completely defined by the control $\beta = \{T, \zeta_{lim}\}$, which describes the set torque and impulse limit. The impulse limit is defined as $\boldsymbol{\zeta}_{lim} = [0, 0, \zeta_{lim}]^T$ pointing in the direction of unit vector $\boldsymbol{e}_\phi$. We ask the question whether there is a control configuration $\beta^* = \{T^*, \boldsymbol{\zeta}^*_{lim}\}$, i.e. a torque-impulse limit combination, which maps the system state just before take-off $\boldsymbol{z}^{-*}_{TO} = (\phi^{-*}_{TO}, \dot{\phi}^{-*}_{TO})^T$ to itself. The subscripts TO and TD indicate take-off and touchdown states, respectively. The state of the flywheel has no influence on the dynamics except at the impulsive event, but we need to make sure that the angular velocity of the flywheel $\dot{\phi}^-_{R,TO}$ is being mapped back to itself to truly guarantee periodic behaviour.

We describe next the forward dynamics of one cycle to search for fixed points. Every new iteration starts with the computation of the post-take-off state

$$\boldsymbol{u}^+_{TO} = \mathbf{M}^{-1}\boldsymbol{\zeta}_0 + \boldsymbol{u}^-_{TO}, \tag{5.11}$$

followed by a mapping of the post-take-off state to the pre-touchdown state through the body's ballistic motion given by the implicit equation for the flight time t_F

$$y + \dot{y}t_F - \frac{1}{2}gt_F^2 + a\cos\left(\phi_{TO} + \dot{\phi}_{TO}t_F\right) - R = 0. \tag{5.12}$$

The pre-touchdown velocities can then be calculated with

$$\boldsymbol{u}^-_{TD} = \boldsymbol{u}^+_{TO} - g\,t_{F\,I}\boldsymbol{e}_y, \tag{5.13}$$

which can be mapped to the post-touchdown velocities using (5.5). The touchdown position in generalized coordinates is then given by the ballistic equations

$$\boldsymbol{q}_{TD} = \boldsymbol{q}^+_{TO} + \boldsymbol{u}^+_{TO}t_F - 1/2g\,t_{F\,I}^2\boldsymbol{e}_y. \tag{5.14}$$

As pointed out in Section 5.2.1, the stance phase is modelled through the kinematic constraints defined by the ground. The case of the off-centred disc is defined by the contact function (5.10), which renders the constrained equations solely dependent on the quantities ϕ and $\dot{\phi}$, i.e. the angular position and its temporal derivative. The constrained equations of motion arising from (5.2), can be written in a concise ODE in the case of the off-centred disc by replacing $z_1 = \phi$ and $z_2 = \dot{\phi}$ to yield

$$\begin{bmatrix}\dot{z}_1\\ \dot{z}_2\end{bmatrix} = \begin{bmatrix} z_2 \\ -\frac{T + mga\sin z_1 + maRz_2^2\sin z_1}{mR^2 + ma^2 + I_S - 2mRa\cos z_1}\end{bmatrix}. \tag{5.15}$$

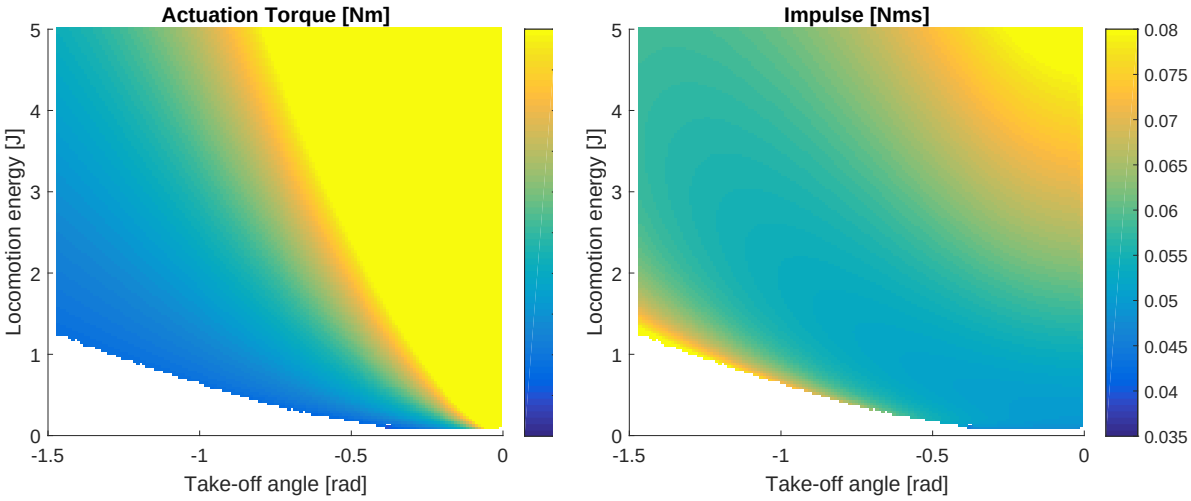

(a) (b)

Fig. 5.4 Fixed point actuation β^* found in nonlinear optimization as a function of take-off angle and total energy before take-off. The control is defined by torque (a) T [Nm] and angular impulse limit (b) ζ_0 [Nms]. Note that the results are computed for a 150x150 grid on the shown angle-energy space.

To search for solutions, we use a single-objective constrained nonlinear program implemented in Matlab® using *fmincon*. We provide initial values of the actuation for the nonlinear solver by assuming the flight phase is symmetric, i.e. $\phi_S^{TO} = -\phi_S^{TD}$, where the superscripts TO and TD indicate take-off and touchdown conditions, respectively.

As a constraint to the nonlinear solver, we force the objective function to return its value once the initial condition ϕ_{TO} is reached. The objective function then solely depends on the other two recurring quantities, and we define the cost as

$$C = \sqrt{\left(\frac{\dot{\phi}_0 - \dot{\phi}_1}{\dot{\phi}_0}\right)^2 + \left(\frac{\zeta_0 - \zeta_1}{\zeta_0}\right)^2}, \tag{5.16}$$

where the subscript 1 indicates the state after going through the forward dynamics (5.11) to (5.15).

The fixed point actuations found in the nonlinear optimization are shown in Figure 5.4. The colour indicates the value of obtained torque in Figure 5.4a, and impulse limit in Figure 5.4b, as a function of the fixed point's take-off angle and locomotion energy. We defined the locomotion energy as the system energy just before take-off, which is proportional to the state $\dot{\phi}_0$. White areas indicate that no fixed point was found. This arose mainly due to the fact that the take-off energy was lower than the potential energy required to reach posture ϕ_0.

Figure 5.4 conveys an important message, which is that fixed points exist for the described control method. It means that there exists periodic locomotion for which the torque not only accelerates the flywheel back to its initial speed at the take-off angle, but also makes up for the energy lost during collision, by re-accelerating the main body during stance phase as governed by the ODE (5.15). In other words, for any point in the state space above the white area there exists a fixed point control configuration β^*. The fixed point torques and impulses transition smoothly in the state space, suggesting that neighbouring fixed points have a similar behaviour. As we will see in the next section, stability is not guaranteed by this smooth transition. An interpretation of the locomotion behaviour is also possible by looking at the fixed point actuations: a high torque in combination with a low impulse, as in the bottom right region of the state space, corresponds to a short stance phase, while a high impulse with a low torque, as in the bottom left region, means that stance phase is long. The proposed control strategy therefore leads to a variety of periodic motions in our proposed locomotion method.

5.3.2 Stability of Fixed Points

We have shown that fixed points exist for the disc with off-centred mass, but the periodic trajectory of the robot is only maintained if it is also stable in the face of disturbances. To study the stability of the found fixed points, we can look at the linearisation of the concatenation of (5.11) to (5.15)

$$\boldsymbol{z}_1 = \boldsymbol{\Gamma}(\boldsymbol{z}_0, \theta), \tag{5.17}$$

where θ represents all fixed parameters such as mass and actuation torque. The linearised map is

$$\mathbf{A} = \frac{\partial \boldsymbol{\Gamma}}{\partial \boldsymbol{z}}\Big|_{\boldsymbol{z}^*,\theta^*} = \begin{bmatrix} \frac{\partial \Gamma_1}{\partial \phi} & \frac{\partial \Gamma_1}{\partial \dot{\phi}} \\ \frac{\partial \Gamma_2}{\partial \phi} & \frac{\partial \Gamma_2}{\partial \dot{\phi}} \end{bmatrix}\Big|_{\phi_0^*,\dot{\phi}_0^*,\theta^*}, \tag{5.18}$$

and we make use of the fact that this term dominates the dynamics in a Taylor series expansion for infinitesimally small disturbances $\delta\boldsymbol{z}$. If therefore the magnitude of disturbance decreases for all possible directions over one stance iteration, the nonlinear fixed point is locally asymptotically stable. This is the same as saying that the absolute value of the eigenvalues of $\mathbf{A}$ has to be smaller than 1, i.e. $\mid \lambda_i \mid < 1 \, \forall i \in \{1,2\}$. It is obvious that (5.17) cannot be represented in a closed expression as it contains differential and implicit equations. We show in Appendix B how to overcome these impediments and still be able to obtain an accurate linearisation of (5.17) around a fixed point. We computed the stability for all the found fixed point actuations (see Figure 5.4). The coloured points in Figure 5.5a refer to the absolute value of the maximal eigenvalue of the linearised map in Equation (5.18), as a function

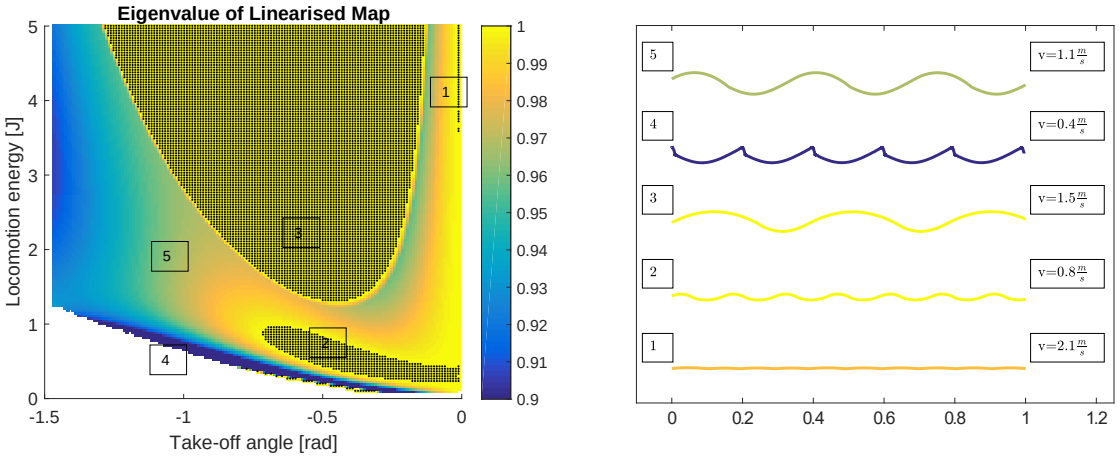

(a) (b)

Fig. 5.5 Stability of the off-centred wheel model as a function of take-off postures and total energy before take-off. Control parameters for the corresponding fixed points are given in Figure 5.4. (a) Eigenvalues of the linearized return map of (5.17). Unstable fixed points for which $|\lambda|_{max} > 1$ are marked with a black dot. (b) Centre of mass trajectories for various stable and unstable fixed points. Velocity on the right hand side is derived by the time taken to reach the 1m mark.

of take-off angle and locomotion energy. We highlight unstable regions, i.e. regions for which $|\lambda|_{max} > 1$, by small black dots. We observe that a large area of the state space is stable, meaning that the fixed point control method in these points is rejecting small state disturbances. As we will see in Section 5.3.2, the system controlled by a stable fixed point control β^* not only rejects small disturbances, but converges to the fixed point even from resting position. We further note that even though the fixed point control varies smoothly within the state space as seen in Figure 5.4, there are abrupt stability changes in Figure 5.5a, as seen in the transition from the coloured stable to the black dotted unstable area. We analysed the instability and found that the unstable fixed point actuations converge to a stable period-2 cycle when perturbed. This means that even if a fixed point is deemed to be unstable, the fixed point control β^* still converges to periodic hopping locomotion. The performance of these points has to be questioned, however, as we find that every second impulse reduces rather than increases locomotion speed.

The locomotion trajectories of centre of mass of the disc for some regions are illustrated in Figure 5.5b together with their locomotion velocity. The motion of trajectory type 1 is operating at high frequency and disappearing hopping height, looking as if the system was sliding on the ground. Bearing in mind that it has set out with the highest locomotion energy, it is also the fastest gait. Motion of type 2 and type 3 are both unstable, yet different

in behaviour. While type 2 looks like a sinusoidal trajectory with symmetric flight and stance phase behaviour, type 3 shows more impulsive stance phase properties. The latter particularly looks like running and hopping centre of mass trajectories of animals at higher speeds. Motion type 4 is the most stable trajectory and shows the least smooth behaviour. It is characterised by a slow final phase during stance, almost halting at the take-off position, followed by a flight phase with vanishing take-off speed in translation, but quick retraction of the shape structure until it hits the ground. The large region of stability characterised by motion type 5 shares smooth and symmetric locomotion trajectories, similar to type 2.

5.3.3 Performance of Control

To study the performance of the fixed-point actuation as per Figure 5.4, we initialised the off-centred disc from resting position. We employ a numerical multibody-dynamics simulation specialised for ground contact modelling with unilateral constraints as presented in Section 2.5. We cannot use the analytical approach as we used for the stability analysis because we assumed bilateral constraints of the forward-dynamics, which is only admissible while the constraint forces in normal direction to the ground are larger than zero, i.e. $\lambda_N > 0$. This condition is violated, when the centrifugal acceleration is larger than the gravitational one, which leads in the bilateral constraint case to the ground pulling the system down, while in a unilateral constraint case, a flight phase is induced. There is a second advantage of using the detailed model, which is that we can simulate a more realistic scenario with friction. Friction is modelled with a Coulomb friction law

$$\lambda_T = \mu \lambda_N \mathrm{Sgn}(\gamma_T), \tag{5.19}$$

where λ_T is the tangential friction force at the contact point, μ is the friction coefficient, λ_N is the normal force at the ground contact point, Sgn is the sign function with $\mathrm{Sgn}(-|x|) = -1, \mathrm{Sgn}(|x|) = 1$, and $\mathrm{Sgn}(0) = \{-1,1\}, x \in \mathbb{R}$, and γ_T is the tangential velocity of the ground contact point. The same model has been used and is described in more detail in [36] for another hopping robot. It is largely based on the LCP formulation of dynamics with unilateral constraints presented in [109].

The system is modelled with two rigid bodies, namely the flywheel and the main body, with properties as described in Table 5.1. The equations of motion of the multibody system are derived using the projected-Newton-Euler approach, and we assumed gravity was the sole constant external force. We assume no damping at this stage in the internal angular degree of freedom and choose a friction coefficient of $\mu = 1$. As implied, we start the simulation from a resting position and apply the torque and impulse limit as found by the fixed point search

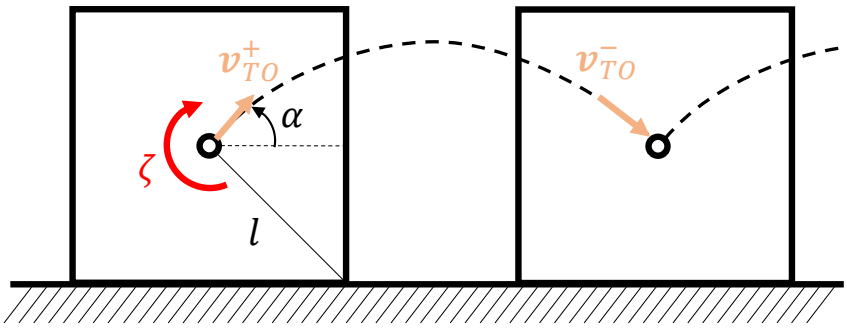

Fig. 5.6 Simplified hopping model of non-strictly convex shapes. The impulse ζ induces the take-off velocity $\boldsymbol{v}_{TO}^{+}$, perpendicular to the diagonal l. The shape of the body is only considered at take-off and touchdown, and flight phase is modelled via a ballistic motion of a point mass.

(see Figure 5.4) for 30 different fixed point positions ϕ and energies E_{TO}. The torque is only being applied during stance phase and only until the flywheel is ready to transfer the impulse ζ_0. The simulation runs for 20 seconds with a time step of $dt = 2 \times 10^{-4}$ s using an Euler integration method.

We compare our results to the theoretical case of a cube actuated with a flywheel as has been studied in [148]. We set the inertial parameters of the cube in accordance with the off-centred disc parameters given in Table 5.1. In terms of size, we set the diagonal of the face of the cube to be $l = 2(R-a)$, as shown in Figure 5.6. The cube lies on one of its faces and we apply an impulse and write the resulting velocity after impulse

$$\boldsymbol{u}_{TO}^{+} = \boldsymbol{u}_{TO}^{-} + \frac{\zeta}{ml^2 + I_S} \begin{pmatrix} l\cos\alpha \\ l\sin\alpha \\ -1 \end{pmatrix}, \tag{5.20}$$

with α the take-off angle with respect to the horizontal axis. We assume a ballistic flight phase, according to the translational initial velocity $\boldsymbol{v}_{TO}^{+}$, during which we ignore the shape of the cube and its rotation. At touchdown, we require for simplicity that the cube lands on its face. Next, we find the impulse required per travelled distance using (5.20) together with the restitution law for translational velocities $\boldsymbol{v}_{TO}^{-} = \varepsilon \boldsymbol{v}_{TO}^{+}$

$$\frac{\zeta}{x} = \frac{g(ml^2 + I_S)(1-\varepsilon)}{2l\,u_x^{+}\sin\alpha}, \tag{5.21}$$

with ε the coefficient of restitution, and u_x^+ the locomotion speed. This equation defines a cost of travel in terms of required impulse over a certain distance as a function of locomotion speed. If energy is restored during the stance phase, the coefficient of restitution becomes greater than zero, hence reducing the cost. For the case of an inelastic cube, we set $\varepsilon = 0$, and α to $\pi/4$. Note that this simple model is not confined to a cube shape. Any polygonal shape can be studied by adapting the centre of mass to contact point distance l, and its corresponding angle α.

Figure 5.7 shows the performance of 900 fixed point actuations sampled from a uniform 30x30 grid in Figure 5.4. The simulation ran for a total of 20 seconds. The vertical axis corresponds to the average velocity over the last 10 seconds, and the horizontal axis is the sum of the transferred impulses over the last 10 seconds divided by the distance travelled during the last 10 seconds. The off-centred disc was initialised from resting position. The brightness of each dot indicates its maximum absolute eigenvalue, taken from the results displayed in Figure 5.5. The results show that for fixed velocities, the least demanding locomotion actuation in terms of impulse per travelled distance correlates with stability of the theoretical return map. This is understood for the case of white dots, as the instability forces the system to use two impulses per stance for locomotion, as discussed in Section 5.3.2. For stable fixed points, the performance tends to improve the smaller the maximal eigenvalue of the linearised fixed point. This behaviour is desirable, as it shows that the most efficient modes of locomotion are also the most stable ones. We find that stability increases with the take-off angle, meaning that a long stance phase improves stability. Indeed, we find that the most stable trajectories are of the type 4 and 5 as in Figure 5.5b. Trajectories with short stance phases as compared to their flight phase as in type 3, tend to be unstable. Furthermore, the figure opposes the theoretical findings of the inelastic cube performance to the off-centred disc. We observe that the strictly convex shape of the disc for the most stable actuation can lead to a requirement of impulse per travelled distance ten times lower than for the cube. This dominance of the disc can be explained by its dynamic motion, i.e. by the fact that a part of the kinetic energy from the previous cycle is conserved in the next one. In fact, if we assign a coefficient of restitution of $\varepsilon = 0.87$ to the cube equation in (5.21), we find that the impulse per travelled distance closely matches the most stable disc performances as shown by the blue dashed line. We can therefore claim that the cube would have to conserve 87% of its velocity at every collision in order to keep up with the off-centred disc performance. In a next step we will examine if this observation can be replicated in a real-life experiment.

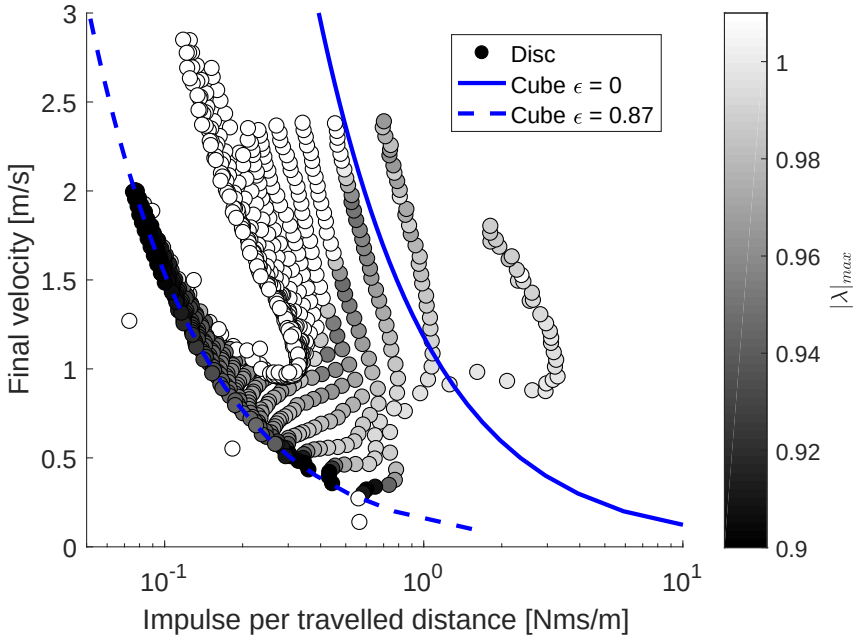

Fig. 5.7 Locomotion speed as a function of impulse per travelled distance after 20 seconds of simulation starting from resting position of the off-centred disc model. The system is controlled with the found fixed point actuations in a uniform 30×30 grid based in the same state space as shown in Figure 5.4. Brightness indicates the absolute maximal eigenvalue of the fixed point return map. The solid line indicates the theoretical impulse per travelled distance of a cube shape with inelastic collisions $\varepsilon = 0$, and the dashed line for a cube with coefficient of restitution $\varepsilon = 0.87$ as per Equation (5.21).

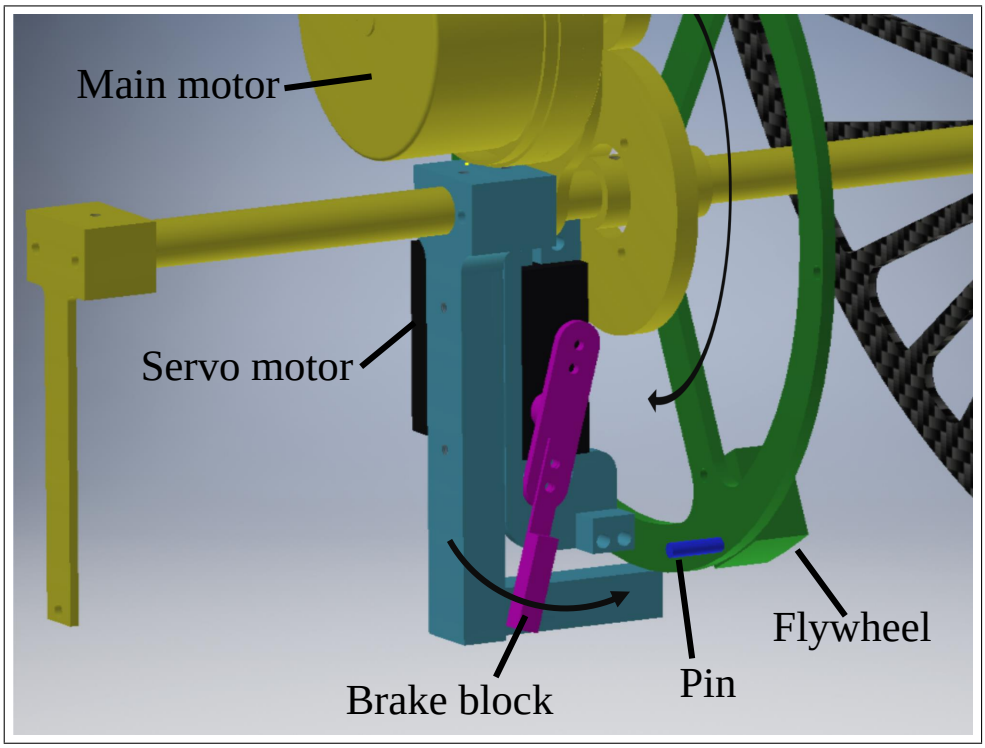

Fig. 5.8 Mechanism of the brake for impulse transmission. The rotation of the flywheel is stopped by an aluminium brake block which is moved by the servo motor to close the connection between flywheel pins and the main robot structure.

5.4 Robot Design

We designed and built a robot named *Robbit* specifically to operate close to the theoretical ideal. There are three main design challenges, namely the impulsive actuation, the reduction of moment of inertia of the main structure, and the extension of the planar model assumption in the real, three dimensional world. Parameter values are in accordance with Table 5.1 for inertial and geometrical parameters.

Our main actuation on the robot is a 100W Maxon® EC 60 flat motor, torque controlled with a Maxon® EPOS2 controller which is not on the robot but placed away from it and connected with wires. The braking mechanism is operated with a standard Parallax® servo motor. The design of the impulsive angular actuation uses a similar mechanism as presented in [144]. As shown in Figure 5.8, our main actuator is fixed on the main body of the robot and is transmitting its torque with a gear reduction of 2.4 to the flywheel which is rotating around the main steel shaft of the robot. The rotation velocity of the main motor relative to the robot is registered by the motor controller with hall-sensors and a rotary encoder. Once the desired rotation speed of the flywheel is reached, the braking mechanism is activated.

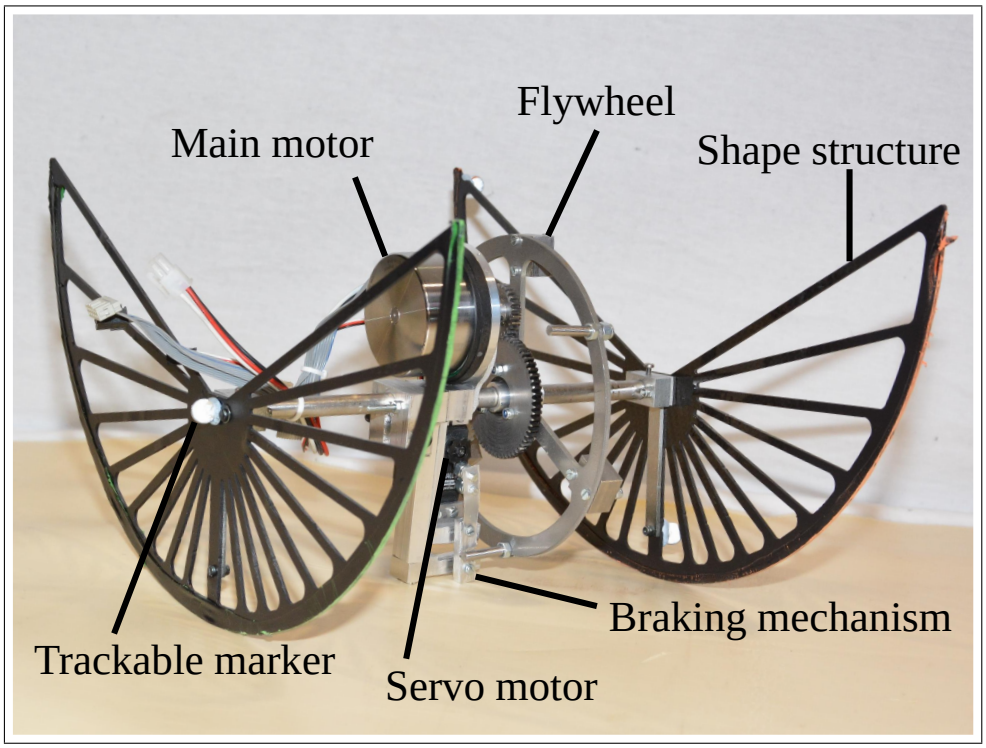

Fig. 5.9 The off-centred disc robot *Robbit*.

Three steel pins firmly attached to the flywheel are passing through a gap in the main robot structure each once per revolution. A small aluminium plate is attached to the servo motor, which can be moved across the gap upon servo motor activation. This blocks the pins from moving through the gap and causes the angular momentum to be exchanged between the flywheel and the gap structure. Another aluminium structure then transfers the impulse to the main steel shaft, inducing a rotation of the whole robot.

For reduction of the moment of inertia, we chose a carbon fibre sheet of 2mm thickness with a spoked wheel-like structure. To mimic the planar dynamics in the physical model, we designed the robot symmetrically in its transversal dimension, connecting the two carbon fibre semi-discs with an aluminium rod of 200mm length.

5.5 Experimental Results

To test Robbit, we prepared a locomotion track with an OptiTrack® motion capturing system which recorded four trackable markers rigidly fixed on the robot with a framerate of 250Hz. The system is controlled centrally with a desktop PC running Matlab® from which the torque targets are sent to the motor controller, encoder signals are being evaluated for a braking

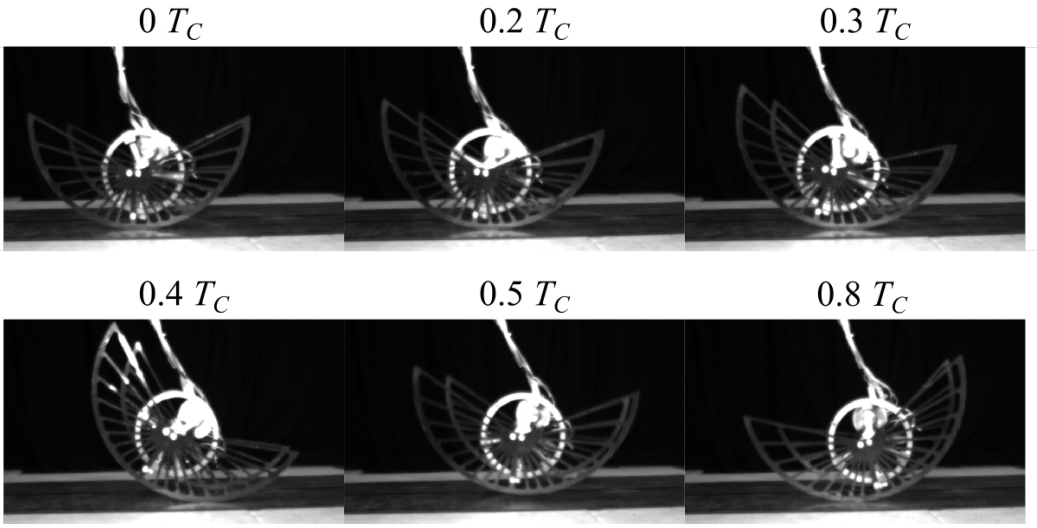

Fig. 5.10 Series of pictures of *Robbit* over one gait cycle T_C from slow motion recordings (300Hz).

decision, and the braking signal is being sent via a COM-port to an Arduino® micro-controller which operates the servo motor. The robot starts at rest and a constant torque is applied until the defined impulse-limit is reached, which caused the braking mechanism to be activated. The motor torque is then set to zero for 100ms during flight phase, before it is again set to the nominal torque. We ran the experiment for 6s and recorded the trajectory of the trackable markers.

Figure 5.10 illustrates the robot's motion with a series of pictures taken over one period of the locomotion gait. The period time T_C is around 0.3s. During $0.4T_C$ of the cycle, the main motor is accelerating the flywheel, which causes the main structure to roll over its carbon fibre feet. Once the predefined impulse limit is reached, the servo motor engages the brake, which induces a momentum transfer between the flywheel and the main robot body. The picture at $0.5T$ shows the robot in mid-flight phase, where the main motor torque is set to zero and the brake is disengaged by the servo motor. The cycle then ends with the beginning of the next stance phase. As can be seen from the series of pictures, this cycle results in a net forward motion of *Robbit*.

The result of the centre of mass trajectories for the generalised coordinates $\boldsymbol{q}$ are shown in Figure 5.11, excluding the transient phase. The control corresponds to a torque of 0.16Nm and an impulse limit that is reached at a relative angular velocity of the flywheel and main structure of $58\frac{\text{rad}}{\text{s}}$. The figure shows the centre of mass trajectories for seven consecutive hops as a function of the cycle progress in percent. We compare the experimental result to the prediction of the simulation framework described in Section 5.3.3. We see that the

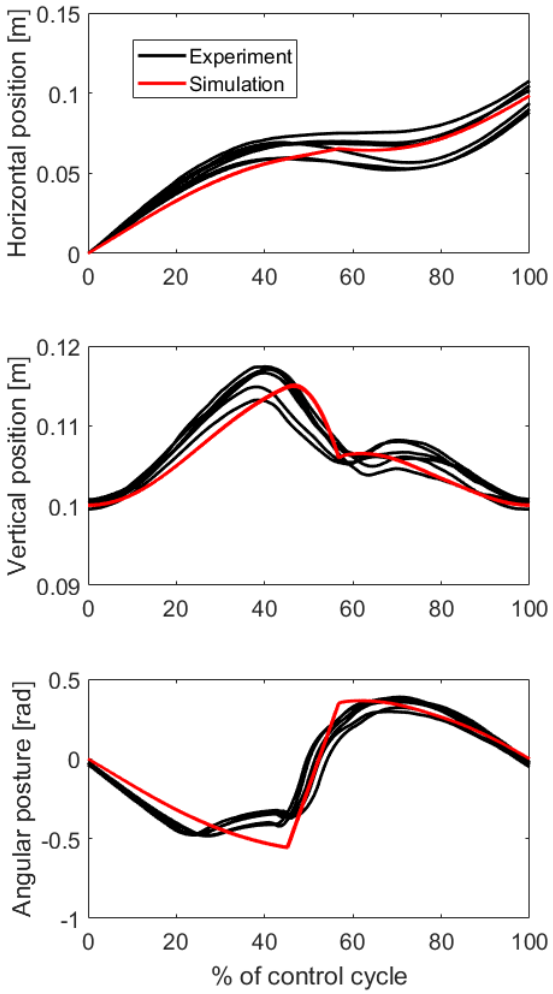

Fig. 5.11 Centre of mass trajectories of generalised coordinates $\boldsymbol{q} = [x, y, \phi]$ of experiment and simulation excluding the transient phase. The horizontal axis captures one full control cycle. The black lines correspond to seven consecutive hops in experiment, and the red line shows the simulation result with the same actuation parameters as in the experiment ($T = 0.16\,\text{Nm}$ and $\zeta_0 = 0.059\,\text{Nms}$).

simulation predicts the magnitude of displacement over the full gait cycle, as well as the observed double hump in the vertical position coordinate. The second hump is due to the backward rotation after touchdown, lifting the centre of mass first before the rolling direction changes, which can be observed in both simulation and real-world experiment.

We controlled the robot with a range of control parameters, as shown in Table 5.1 under *Experiment control*. The velocities of these experiments as a function of the impulse per travelled distance (derived from impulse limit and the measured hopping frequency) are shown in Figure 5.12, together with the theoretical cube performance. The results show, in accordance with the theoretical predictions, that the impulse per distance is roughly ten times lower than the cube's theoretical prediction. Almost all of the experimentally recorded trajectories correspond to trajectory type 4 in Figure 5.5b, which are stable, efficient, and characterised by a long stance phase followed by a rather short flight phase. The experiments further show that any configuration of control parameters β leads to bounded and almost periodic locomotion after a few transient hops. The system therefore not only outperforms a cube in its economical use of impulses, but also converges to periodic and continuous locomotion without precisely defined control parameters. The system finds its fixed point autonomously for the given control, a behaviour which we ascribe to the self-stabilising properties of the strictly convex shape.

5.6 Discussion

The results showed, based on the cases of a disc with off-centred mass and a cube, that strictly convex shapes outperform theoretical performance of non-strictly convex shapes in terms of their locomotion speed as a function of impulse per travelled distance. By comparing systems in terms of their impulse per travelled distance at constant speeds, we essentially compare their energetic costs of transport. The dimensionless cost of transport as defined by [149] for locomotion in animals, is the ratio of metabolic rate to the product of speed and body weight. This definition has been adopted by the robotics community, such as in [150], by replacing *metabolic cost* with *energy used*. Animals reduce their energy use with mechanisms to efficiently redirect their centre of mass velocity [151]. Among others, two important mechanisms have been thoroughly studied in biomechanics and robotics, namely spring-mass models [12] and inverted pendulum models [152]. Both mechanisms conserve a fraction of the kinetic energy from the previous step to the next. In the case of strictly convex shapes, energy is conserved by smoothly redirecting the centre of mass through a rolling motion. Loss-less redirection of centre of mass is necessary to minimise the cost of transport, but it is not sufficient. A significant source of energy loss in terrestrial locomotion

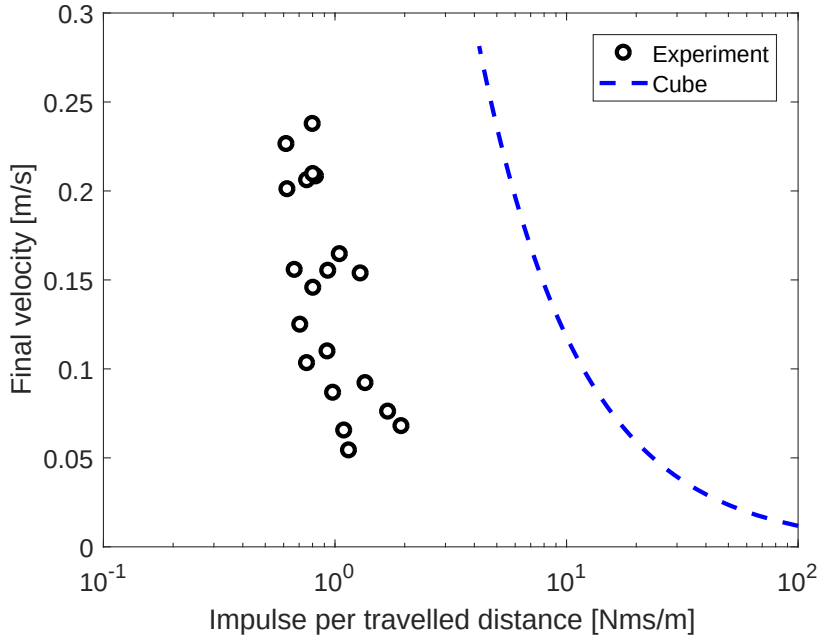

Fig. 5.12 Experimental converged hopping speeds as a function of impulse per travelled distance. Each circle indicates a robot experiment with fixed actuation parameters. We set the parameter range for the series of experiments for torque between 0.1 and 0.3 Nm and impulse limit between 0.04 and 0.07 Nms. Experiment duration was 6 seconds and the data plotted corresponds to the average speed as a function of the average impulses over the travelled distance. The dashed line corresponds to the theoretical speed of an impulsively actuated cube with face diagonal $l = 2(R-a)$ and coefficient of restitution $\varepsilon = 0$.

occurs due to interactions with the ground. As we showed in Figure 5.7, a cube would have to restore 87% of its velocity at touchdown to perform with the same cost of transport as the off-centred disc for a given locomotion speed, which indicates a low collisional cost at touchdown in the strictly convex shape case. This observation agrees well with studies of bipedal walking with curved feet, as the authors describe a reduction in energy loss in the step-to-step transition compared to point feet [54], [55].

In this work, we have also demonstrated how strictly convex shapes can lead to stable hopping locomotion without any state feedback except the flywheel speed. The self-stabilising properties of curved feet have been studied for locomotion in monopods, bipeds, and quadrupeds [40]. Many other examples of self-stabilising locomotion exist [36], [39], but the applications move beyond locomotion; related work in the stabilisation of juggling through a convex shape [43] showed how apex and paddle position can be self-stabilised, meaning no sensory feedback is required to juggle a ball with a paddle. This relates to our hopping system given a fixed point actuation β^*, as no feedback from the environment is necessary to stabilise the motion, not even to transition from resting position to the final locomotion speed. An extension of this work could include temporal change of shape to further improve the cost of transport or locomotion speed. The potential of active external shape is abundant in robotics. There are examples of robots that use their strictly convex shape to actively propel themselves, as shown in the modular loop robot presented in [153], or in the spherical robot with inflatable pouches that induce a rolling motion, as studied in [154]. We have recently shown that a shape change during locomotion which does no positive work on the system can indeed increase locomotion speed [79].

Our proposed locomotion method can help to improve energy use for locomotion with momentum stored impulse actuation. This is especially useful in exploratory ventures where energy is scarce, as is the case in space robotics, such as in [148]. Furthermore, our locomotion method can provide a new mode of locomotion for the vast number of spherical robots [155] which have been built and studied in recent years. For instance, a spherical robot with internal momentum-stored impulse actuation and off-centred mass can generate the described hopping motion, which would enhance its locomotion capabilities.

Our findings, shown in Figure 5.7, indicate that stability and efficiency are coupled such that the fixed points associated with the smallest maximal eigenvalue of their return map are also the ones which demand the smallest impulse per travelled distance. We have presented similar findings of the coupling between stability and efficiency in [36], and also for the case of a hopping robot with a strictly convex foot shape. It is a striking feature of these locomotive systems that they are both efficient and robust.

5.7 Conclusion

In this chapter, we studied the locomotion of strictly convex shapes actuated by momentum-stored impulses. We proved for the simple case of a disc with an off-centred mass, that fixed points to this locomotion methods exist, and that a large number of them are stable. A simulation of the system from resting position reveals the superiority in terms of required impulse per travelled distance, as compared to the case of an impulse-actuated cube. We validated our findings in a real world platform with the robot *Robbit*, showing that ten times lower impulses are required to travel a certain distance compared to the theoretical case of a cube. The results demonstrate the significance of shape in the dynamical behaviour of hopping, and how it can be used to improve stability and efficiency of locomotion in robots. In the next chapter, we further study the effect of shape on locomotion performance but other than in this chapter we allow for discrete foot shape changes during locomotion.

Chapter 6

Improving Hopping Dynamics with Inelastic Impacts[1]

Discrete actuation can be used to increase the system energy, but it can also be used to reconfigure the robot and thus change its shape and environmental interaction. In this last technical chapter, we show one of the simplest reconfigurations which consists of switching between two discrete foot shapes. The different foot shapes are associated with different energetic impact collision losses, and we show that the right timing of foot shape changes can improve locomotion speed, despite the fact that no positive energy is added to the system. Discrete actuation thus not only emphasises impulses which increase the kinetic energy of the system, but also impulsive shape changes in locomotion systems which alter the system-environment interaction passively.

6.1 Introduction

In legged locomotion, impacts of a moving body with the ground are well approximated with impulses, especially after McGeer discovered passive dynamic walking in rigid machines [13]. Since then, researchers have found simple models to explain various behaviours in animal locomotion using impact inducing collision models, e.g. in walking [44] or hopping [41]. Impacts are usually considered unavoidable, yet undesirable as they are inherently

[1] This chapter presents the collaborative work with my supervisor F. Iida. I have initiated the problem statement, designed and built the robot *CaneBot*, conducted, planned and prepared experiments, and wrote the paper. F. Iida helped discussing and revising the paper. The peer-reviewed publication which forms the basis of this chapter is

- Fabio Giardina and Fumiya Iida. Discrete foot shape changes improve dynamics of a hopping robot. In *International Symposium on Experimental Robotics*, pages 113–122. Springer, 2016.

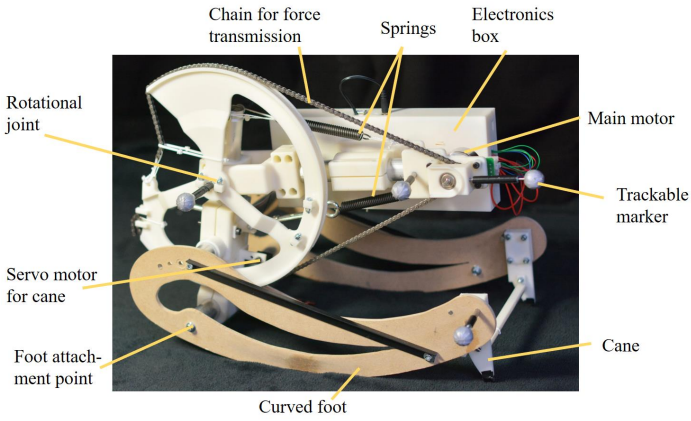

Parameter	Value
Mass upper body	1.34 kg
Mass lower body	1.43 kg
Foot radius	0.4 m
Spring constant	2.52 N/mm
Gear ratio	10:1
Joint to foot attachment point length	0.16 m
Joint to upper body CoM length	0.17 m
Foot attachment point to cane length	0.33 m

Fig. 6.1 The robot used to investigate influence of shape changes in hopping on locomotion speed and table with main mechanical parameter values.

coupled to mechanical energy loss. Although there are theoretical studies that show cases of legged locomotion without collisional energy loss [65], every legged animal and robot undergoes some loss due to impact in real systems. In fact, it was found that the energetic cost for human like walking is mainly due to the impulsive impacts in the step-to-step transition [67]. Minimising the impact losses can then be achieved by applying toe-off impulses just before the step transition [10], [156]. A detailed collisional analysis of a simple model by Ruina et al. suggests that multiple impacts during the stance phase reduces the energetic loss, due to a sequenced redirection of the centre of mass [51]. Stability considerations in a simple double pendulum model revealed that impacts provide essential stabilising effects which cannot be induced otherwise, e.g. impulsive and instantaneous velocity transitions [63], [157]. Even though mathematical tools exist to analyse the influence of impulses in mechanical systems, e.g. by means of the impulse extended Lyapunov function [158], it is hard to define design rules for legged systems due to the convoluted dependency of dynamics and morphology. Nevertheless, a simple analysis of a bipedal model shows that a flat or round foot shape improves energy efficiency over a point foot model [49], which was also concluded in a study with human subjects [54], where the authors point out that the rolling like behaviour of the centre of pressure progression in human walking is beneficial for the centre of mass redirection in terms of energy efficiency. From this perspective, it is important to carefully design the morphology as a function of impact losses, for which a mathematical method is presented in [159]. Furthermore, it might also be beneficial to change the foot

shape during the locomotion gait to adapt to impacts to which the pronation of the human foot just before touchdown might hint [160]. Shape changing locomotive robots have been studied in the past, such as the contour changing wheel [161], yet we had to acknowledged that the role of shape induced impacts in robotics is an understudied topic.

In this chapter we are investigating how discrete and controlled shape changes in a hopping robot can alter locomotion properties, and use forward speed as the main measure for evaluation. The next section presents the used system and methods to study the influence of shape induced impacts on locomotion, results are illustrated in Section 3, Section 4 contains an analysis of the main findings, and the last Section 5 concludes the chapter.

6.2 Methods

To analyse the influence of shape change during locomotion, a curved foot hopping robot with two linked rigid bodies was built, as is shown in Figure 6.1. This system is driven by a motor torque in the joint between the rigid bodies, generated by a motor on the upper body tip. Two linear extension springs are placed between the upper and lower body to achieve parallel elastic actuation. The robot is equipped with a curved foot shape, which has proven to show good performance in both stability and efficiency [36]. The foot is made out of plywood and is operating on a wooden floor. The main geometrical properties of the robot can be found in the table depicted in Figure 6.1. In order to induce a foot shape change during locomotion, a small mechanical structure, from now on referred to as *cane*, is placed in the front tip of the foot which can be either extended or retracted, and hence switch between two discrete shape states. When extended, the front part of the curved foot is bypassed during rolling due to the blocking cane, altering the dynamics and therefore locomotion behaviour. When the cane is retracted the robot moves as if no cane was there to influence locomotion.

The main motor is controlled by an open-loop signal which induces a motor torque in the robot joint approximated by a bi-directional pulse as shown in Figure 6.2. For a curved foot hopping robot, this type of signal has shown to be better in terms of stability and efficiency as compared to a sinusoidal signal [37]. The motor torque is applied first in positive direction for $100ms$ and then in negative direction for another $100ms$ with respect to the lower body (causing the robot to contract first and then extend) with a torque amplitude of $\pm 0.4Nm$. The period time T is given by the applied control frequency. The cane is being extended according to the cane duty cycle CDC in synchronisation with the motor torque frequency for $CDC \cdot T$ seconds and after a delay of $CD \cdot T$ seconds. The influence of the cane at various times is tested by varying CDC and CD for constant open-loop control parameters of the motor. The progression of the robot for two extreme cases with the cane being either permanently

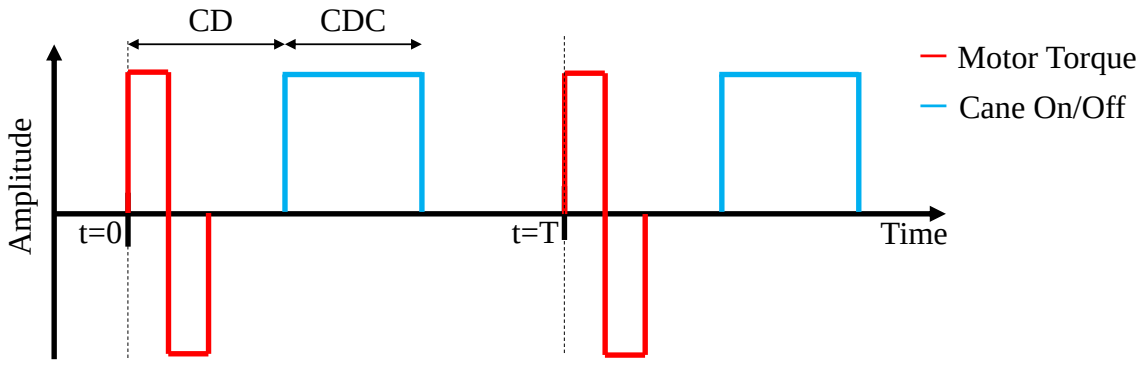

Fig. 6.2 Main motor and cane open-loop control as a function of time. T is the period of the assigned main motor control frequency, CD is the delay as a fraction of the period, and CDC is the cane duty cycle within the period.

retracted or extended is shown in a series of pictures in Figure 6.3. It is important to note that the cane is designed not to do any positive work on the robot when in contact with the ground, but to induce only inelastic collisions. The only energy needed to operate the cane is for retraction and extension during non-ground contact phase, which is assumed to be negligible.

The robot is driven by a 70W Maxon EC 45 flat motor and is controlled via a Roboteq SBL 1360 motor controller. The cane is being retracted with a Parallax 6V standard servo and a linear spring is pulling it back to the extended position if the servo motor is disabled. The robot is untethered and powered by three lithium polymer batteries, providing 24 volts. Radio modules are installed to establish communication with the host pc, and an Arduino Mega 2560 micro controller coordinates the operation. The motion is tracked using 6 reflective markers placed on the robot which are being recorded by an OptiTrack motion capturing system. Trajectories are also being evaluated from video analysis using the software Kinovea.

6.3 Results

The following results are shown for a main motor control frequency of $2.8Hz$, and a pulsed motor torque of $\pm 0.4Nm$ for a 10 second run per experiment. It is important to note that the only difference in the remaining report is induced by the timing of the passive cane, not the main motor control.

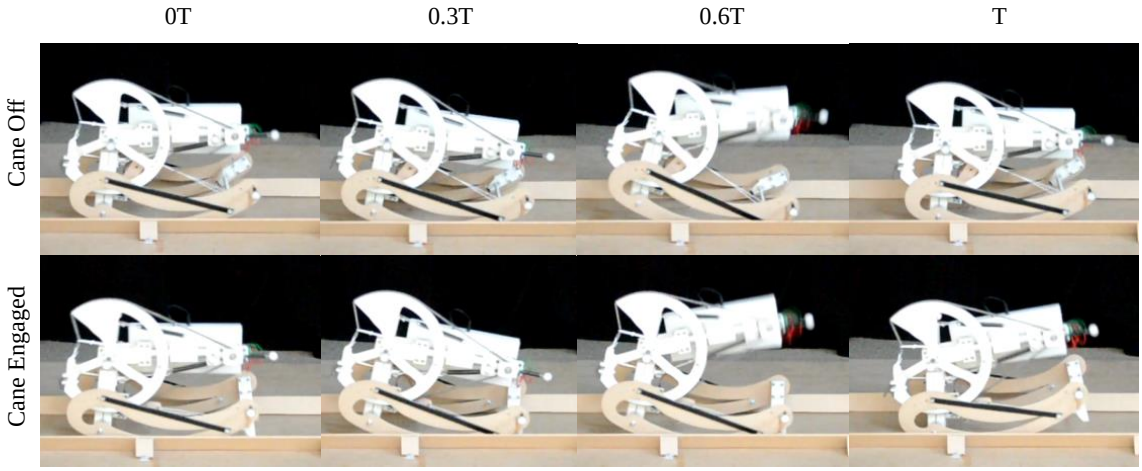

Fig. 6.3 Robot progression over one period T of the main motor control for the case with retracted cane and extended cane.

Figure 6.4 shows the trajectory of the uppermost tracked marker on the upper body of the robot for different cane control. Figure 6.4*a* shows the behaviour with retracted cane throughout the run, and Figure 6.4*b* the behaviour with permanently extended cane. The grey circles in both plots indicate the start of a new pulse cycle of the main motor. For the retracted cane case, the dynamics suggest a period-1 behaviour, meaning that the trajectory reaches the initial state after T seconds with respect to the main motor actuation period. For the extended cane, another regular pattern emerges, although the system state returns to identical values only after $2T$. This period-2 behaviour was found to be slightly slower than the cane-less period-1 motion, which might be explained by the "looping" of the trajectory, i.e. the backward motion of the tracked marker.

Figure 6.5 illustrates the locomotion distance covered as a function of the cane timing. The abscissa shows the cane duty cycle *CDC* and cane delay per period *CD* in the format CDC/CD that was applied to the run. A value of $0.5/0.2$ for example indicates a duty cycle of 0.5 and a cane delay of $0.2T$. Figure 6.5*a* shows the cane timing for duty cycles of 0.5 and delays between 0 and $0.5T$, whereas Figure 6.5*b* illustrates cane duty cycles of 1 with delays ranging from 0 to T. The ordinate shows the average travelled distance per hop, which is proportional to the average hopping speed. The performance of the cane being permanently on or off is indicated with a solid grey or black line, respectively. Note that the robot was initiated from a resting position, and the average hopping distance includes also the initial transient phase. The series of experiments was repeated five times, and the figure shows error bars of one standard deviation around the average.

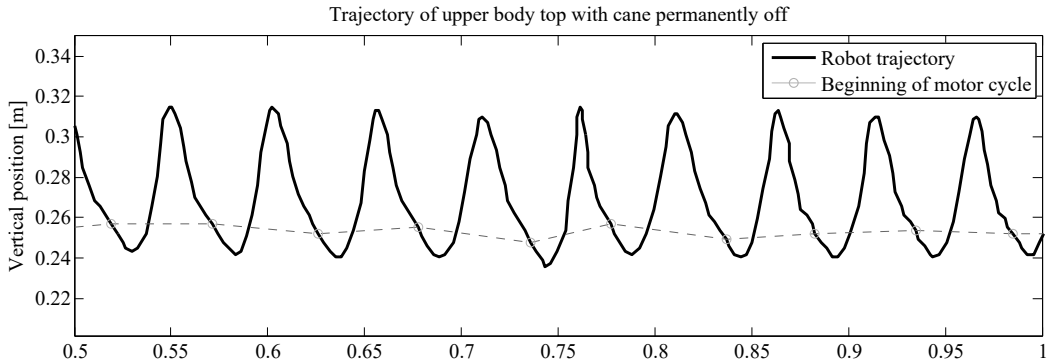

(a)

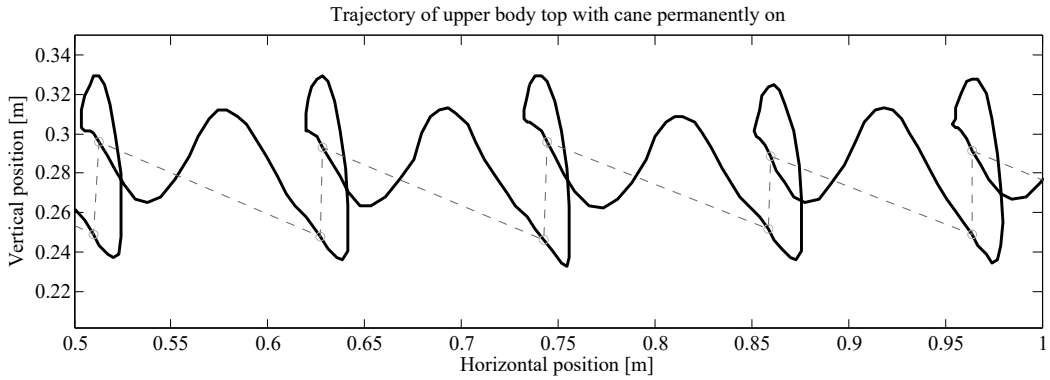

(b)

Fig. 6.4 Trajectories of upper body top marker for a retracted cane (a), and extended cane (b) for the same main motor control. The grey circles indicate the main motor timing with period T.

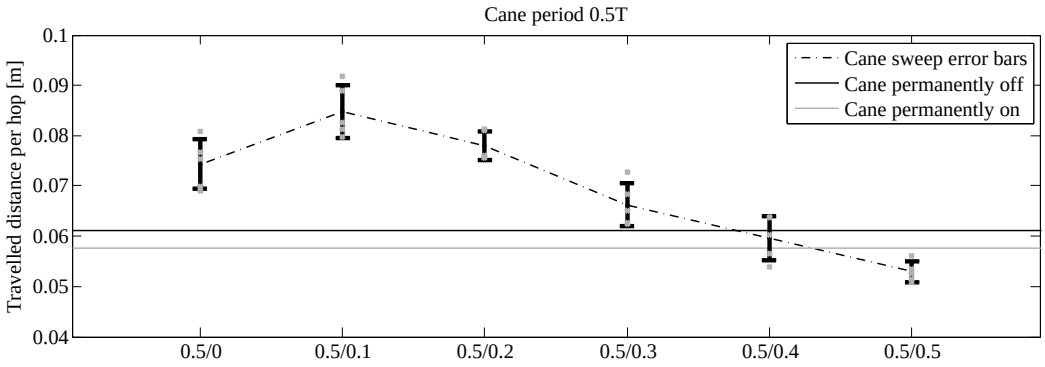

(a)

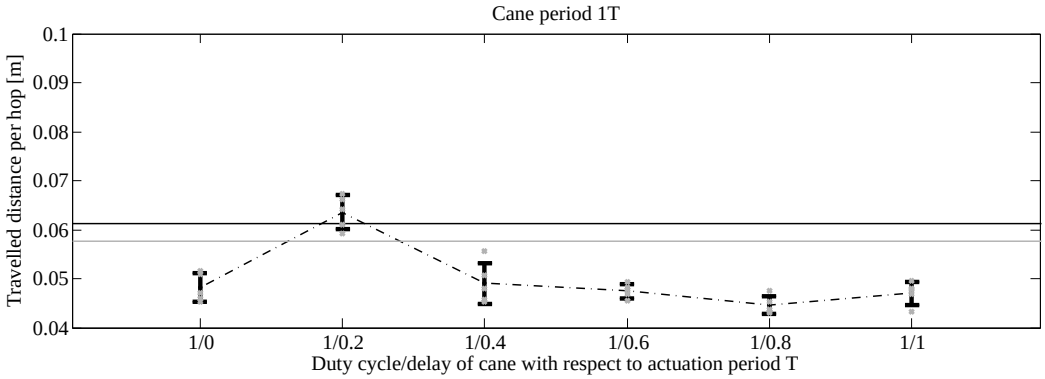

(b)

Fig. 6.5 Averaged travelled distance per hop over a $10s$ run for different cane timings for open-loop control with $\pm 0.4Nm$ motor torque, and $2.8Hz$ actuation frequency. The cane timing on the abscissa is indicated by cane duty cycle CDC over cane delay per period CD in the format CDC/CD. The error bar indicates one standard deviation for the five sets of experiments that were conducted.

The results show how for constant main motor control, the travelled distance can be altered significantly by the timing of the cane. If the cane has a duty cycle of 0.5, the hopping distance is increased for almost any cane delay. The peak velocity is reached when the cane is turned on after a delay of $0.1T$, covering a distance of around $8.4cm$ per hop, which is around $\frac{1}{4}$ body length per hop. This corresponds to a *speed increase of roughly* 40% compared to the cases of the cane being permanently on or off. If the cane is operated only every second period, which is for duty cycles and delays per period of $CDC + CD \geq 1$, the performance decreases generally compared to the $0.5\,CDC$ case and is most of the time even lower than cases of the cane being permanently on or off.

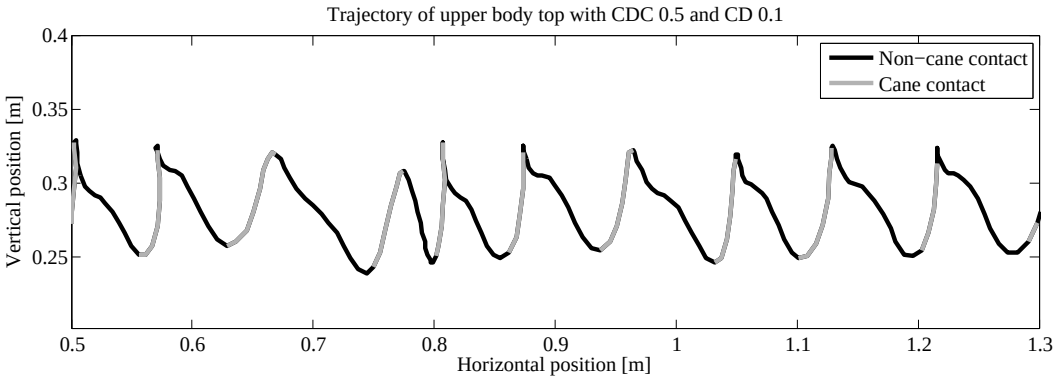

Fig. 6.6 Trajectory of the upper body top marker and cane ground contact times for the fastest case with duty cycle of 0.5 and delay of $0.1T$.

6.4 Analysis

The apparent increase of hopping speeds as a function of the cane timing may seem surprising given that there is no positive work being done by the cane, but only passive and energy consuming impacts are induced through the discrete foot shape change. In order to understand what is happening in the collisional process one needs to consider the actual cane contact. Figure 6.6 shows the trajectory without the initial transient phase of the upper body top marker for the fastest cane control with $CDC\,0.5$ and $CD\,0.1$. The parts of the plotted trajectories which are grey indicate contact of the cane with the ground which was extracted visually. It is interesting to note that the "looping" of the upper body trajectory is somehow being avoided by the cane timing of the fast cane control. This is even more surprising, as the motion seems to be rather chaotic and no distinct periodicity can be observed. One might expect the looping to occur at least once, but it was not observed in any of the five trials.

After analysing the resulting motion of the robot in the captured trajectories, we identified three occurring cases just before take-off which seem to distinctly define the subsequent dynamics. In order to simplify understanding, we are making use of the impulsive eccentric wheel model as is presented in [41] and illustrations of the three cases are depicted in Figure 6.7. The first case (a) is naturally emerging in the stable cane-less hopping motion and is characterised by a leading ground contact point to the centre of mass with respect to the direction of travel just before take-off. The impulsive motor torque then causes a backward rotation during flight phase and the robot lands with a leading centre of mass position relative to the ground contact point. This causes the robot to roll in forward direction after touchdown. Interestingly, the point of touchdown is naturally adjusted such that the same take-off posture is achieved after the rolling phase in every hopping iteration, hinting to

self-stable characteristics of the system. Case (b) occurs with an extended cane and a forward rolling angular velocity $\dot{\phi}$ which is negligible. The ground contact point and centre of mass of the robot are roughly aligned with respect to the travelling direction. The take-off pulse causes a strong backward rotation, shifting the point of touchdown further back than in case (a) and hence inducing accelerated rolling in the next hopping iteration. Lastly, case (c) is observed with an extended cane and a forward rolling angular velocity $\dot{\phi} \gg 0$. In this case, the impulsive impact of the cane with the ground induces a rotation of the centre of mass around the point of cane contact, which promotes a ballistic trajectory that is favourable for a long jump. This behaviour is similar to pole vaulting, where the athlete is using the pole's contact point as a centre of rotation to surpass a raised bar. Due to the ballistic effect, the pulsed actuation torque can only cause a slight backward rotation, leading to a small distance of point of touchdown and centre of mass in travelling direction. This means that the gained rolling speed during stance phase is the smallest of the three presented cases.

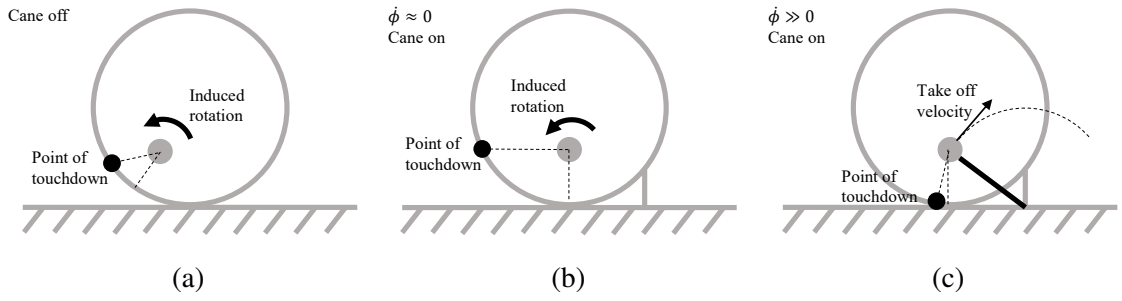

Fig. 6.7 Three cases of observed take-off positions using a wheel with eccentric point mass model presented in [41]. The grey filled circles indicate the centre of mass of the robot model, and the black arrows show the main take-off motion after the pulsed motor torque was applied.

The three shown cases can be used to explain the observed discrepancies in locomotion trajectories. As was already explained, case (a) causes the cane-less period-1 motion, which naturally emerges after a few transient hops. The period-2 motion, as shown for example in Figure 6.4(b) with the cane being permanently engaged, is explained by a switching between cases (b) and (c). The high rolling velocity $\dot{\phi} \gg 0$ in case (b) after touchdown causes the pole vaulting effect seen in case (c), and the small rotational retraction in case (c) then causes a small angular rolling velocity $\dot{\phi} \approx 0$, which in turn gives rise to case (b) in the next hopping iteration. Now, how can this simple model explain the trajectories observed in 6.6(b) for the $CDC/CD = 0.5/0.1$? We observed that this cane control causes the robot to operate mostly in case (c), the pole vaulting mode. Whenever the decelerating case (b) is about to be induced by a previous case (c), the cane is being blocked by the ground and can not extend due to the body posture and previous retraction of cane, which really induces the faster

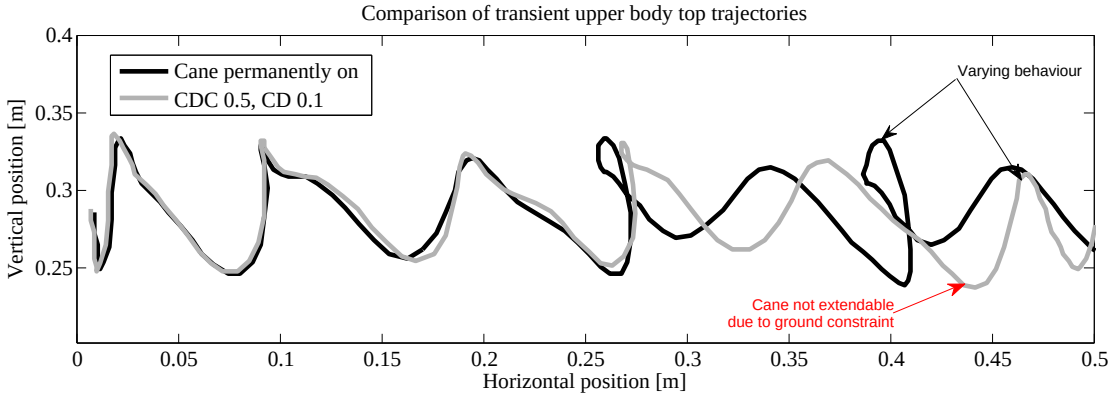

Fig. 6.8 Transient trajectories of the upper body top marker for the case with the cane being permanently on, and the case with duty cycle of 0.5 and delay of $0.1T$.

cane-less case (a) instead of (b). The robot naturally chooses the best option for increased locomotion speed with this control and avoids case (b) completely, only operating in (c) and switching to (a) in some extreme cases. No period-2 motion is observed as the cane extends not always quite to its full extent before ground contact occurs, leading to a slightly different and chaotic behaviour. Figure 6.8 compares the transient phase of the best control case $CDC/CD = 0.5/0.1$ and the case with permanently engaged cane. The first appearance of the blocking cane, inducing the state (a) instead of (b) and avoiding the decelerating looping trajectory, is indicated as well.

6.5 Conclusion

In this chapter we presented that a discrete change in foot shape during locomotion of an open-loop controlled hopping robot can induce a variety of locomotion gaits and increase the travelling speed. The foot shape is passive and does not do any positive work on the robot, but influences the time and direction of dissipative impacts. With a simple model, three distinct cases were identified just before take-off, which define how the pulsed torque influences the touchdown posture. The fastest locomotion speed can only be achieved by switching between the accelerating cases and avoiding the decelerating case, which can be realised by the right timing of shape change. The presented insights may provide a new perspective for the development of control laws for increased locomotion stability, efficiency and speed through foot shape changes.

Chapter 7

Conclusions

In this thesis, the concept of discrete actuation was described and its benefits for the understanding and control of hopping locomotion were presented. The discretisation is such that the dynamical system becomes piecewise passive, meaning that actuation is only allowed at a finite number of instants in time. To this end, the dynamics of hopping locomotion were translated to a discretised system with the eccentric wheel model which is subject to impulses and passive flight and stance phase. The theoretical model was used for the study of locomotion trajectories in robots and animals in Chapter 3 and for energetics of locomotion strategies in environments with obstacles in Chapter 4. The practical benefit of impulsive actuation in real-world robots was subject of Chapters 5 and 6, where rotational impulses were used to induce hopping locomotion in the robot *Robbit*, and where the timing of impacts in the robot *CaneBot* was identified to be strongly influencing locomotion dynamics, respectively.

The presented work in this thesis is only a small step in the endeavour of building autonomous, stable, and energy effective robots. This chapter therefore aims to relate the findings presented in the various chapters to the greater picture, and discusses future work which aims to navigate this research in the direction of the end goal. The next section will discuss the achievements in the context of the contributions stated in Section 1.4.

7.1 Discussion of Contribution

The discretised actuation approach was applied to the case of hopping locomotion with the goal of understanding locomotion physics and of predicting locomotion characteristics of robots and animals while revealing a clear causality of actuation to behaviour. The eccentric wheel model introduced in Chapter 3 suggested how such a discretisation can be done and how it can be used to predict locomotion dynamics of robots and animals. The dynamics of

one full gait cycle was reduced to 4 nonlinear maps in closed form, two for the impulsive events occurring at touchdown and take-off, and two for the energy-conservative maps of flight and stance phase. The concatenation of those four maps provided a prediction of the system's state from each hopping iteration to the next, without the need for integration. However, this only applies for the case where the take-off impulse is synchronised with the take-off angle, and thus the system becomes autonomous. In the open-loop case, the stance phase must be integrated in order to find the correct state at the time of impulse. The arising stance phase dynamics is governed by the differential equations of the form (5.15) (dropping the torque term T) and are easily integrated numerically. In fact, we know that the solution is periodic and energy-conservative and it therefore suffices to solve only half the period to reconstruct the full solution of the stance phase dynamics.

We would like to point out that other discretised models commonly do not study hopping or running locomotion, but mostly focus on walking as for instance in [44] and [10]. On the other hand, spring-mass models such as in [12] predominantly study hopping and running locomotion, presumably due to the elastic energy storage of the spring which is intuitively associated with hopping (there are, of course, important contributions of spring-based models to explain walking rather than running/hopping such as in [20]). The eccentric wheel model showed that hopping locomotion can well be studied with the discretised approach due to the energy-conserving property of the rigid strictly-convex shape in the model. Other than storing elastic energy in a spring, the model stores potential energy due to gravity and redirects the centre of mass velocity over the stance phase–in analogy with the spring-mass model. The stance phase trajectory in the eccentric wheel model is predefined through the mechanical shape, which means that once the stance phase energy is known, the resulting trajectory and any velocity state can simply be computed through an algebraic relation. This stands in contrast to the spring-mass model, where knowing the energy at a given state requires an integration of the non-linear differential equations over the full path - uncertain if the system actually ends up in the point of query. The spring-mass model thus requires an integration of a second-order nonlinear differential equation as described in [12]. The advantages of a rigid shape which predefines a locomotion trajectory is that it provides a constant path of the centre of mass during stance phase. This opposes the spring, which has an infinite number of possible stance phase paths, which makes it much more flexible, yet less robust.

The self-stabilising properties of rigid and curved feet has been suggested by Ringrose in [40], where he showed how locomotion can be achieved without feedback control. Ringrose demonstrated the self-stabilising properties in his robot *Robop* for hopping in place, and a similar design was developed in [36] for forward hopping. The analysis of the forward hopping case, where the robot is solely controlled with an open-loop actuation, shows the

remarkable self-stabilising properties of the system: forward hopping is easily achieved from resting position without controlling the transition phase. Appendix C explains how open-loop stability is achieved in the impulsive wheel model with centred mass. Concrete results are given for actuation, timing, size and inertia properties of the system and how they relate to self-stability.

Discrete actuation was used to study the physics of hopping locomotion and to understand the energetic cost of overcoming an acute obstacle with different locomotion strategies. The idea was initiated through the question why are there no wheels in nature, and what are the conditions for which legs are better than wheels? Although there are examples of animals passively rolling by exploiting the natural environment [162], [163], [164] or even actively pushing spherical objects [165], few species in the animal kingdom propel themselves forward using a rolling locomotion strategy [166], [167]. The reasons for the missing wheel in nature is obviously a difficult question to ask given the complexity of animals. We therefore asked the question slightly differently and in the well-defined context of discrete actuation: given the morphology of a wheel, is it energetically better to roll or to hop over obstacles? As elaborated in Chapter 4, the Froude number and the moment of inertia of the wheel were identified to be the determinant properties for energy optimality of either hopping or rolling. The analysis revealed that in the limit case of infinitely small obstacle heights, as derived in Appendix A, rolling is outperformed above a Froude number of 1. This seems at first sight surprising, as rolling is commonly associated with no energetic loss for vanishing obstacle heights, but so is hopping in the case of vanishing obstacle heights. The Froude number implies that rolling loss is proportional to the centripetal acceleration of the wheel mass around the obstacle tip, while the hopping loss is proportional to gravitational acceleration. This argument has previously been made to interpret limiting factors of walking [168], and optimality transition from walking to running was also reported in [11]. The Froude number appears to define the transition speeds even for non-limit cases, and we show in Appendix A that above a value of $Fr = 2$, hopping is always the better strategy to overcome the obstacle.

We have shown with the rotational hopping strategy, as presented in Chapter 4, that the modelling of mass distribution can lead to a novel way to overcome the obstacle, which is energetically beneficial for low moment of inertia. "Low moment of inertia" can be made precise, as we show in Appendix A. The energy saving mechanism at ground collision of the rotational hopping strategy compared to the trivial hopping strategy vanishes as the numerical value of the moment of inertia becomes equal to the mass $I = m$. Large legged animals which have a moment of inertia greater than their body mass do not exist any more, but dinosaurs like Tyrannosaurus rex might have been close to satisfying this condition. Interestingly,

scientists are still debating whether Tyrannosaurus rex was capable of running or merely walking [169].

The nature of the impulses discussed in this section so far, assumes that they are *translational*, that is, they change the translational velocity of system's centre of mass directly to increase momentum in the direction of locomotion. Translational impulses stand in contrast to *rotational impulses*, where a change in the body's rotation around its centre of mass is induced and there is no direct contribution in the direction of locomotion. There is a way, however, to convert the rotational momentum into translational motion through the shape of the body and the interaction with the environment, which was discussed in detail in Chapter 5. Not only did the rotational impulse in the robot *Robbit* induce flight phase through the strictly convex foot shape, but the charging of the flywheel to generate the next impulse also accelerated the system during stance phase. It is due to these two mechanism that forward hopping locomotion can be achieved through rotational momentum transfer in a single rigid body. The body of the robot therefore facilitates purposeful behaviour and reduces the control effort to an impulse in a single point in time. Such systems where the morphology facilitates control is studied under the umbrella of *morphological computation* [6]. Its meaning was described as a "task distribution" between the controller, the morphology, and the environment. Based on this premise, the body can take up tasks of the controller to simplify or replace control. The ability of the body to fulfil control tasks was addressed in Blickhan et al.'s paper "Intelligence by mechanics" [8], where the spring-mass model was analysed for its self-stabilising property.

Self-stability was found in *Robbit*, as it robustly converges to a steady forward hopping behaviour from standstill. The precise mechanism behind the self-stabilising property is not understood, although Appendix C hints towards a self-stabilising principle in the open-loop control case. Understanding the effects of self-stabilty is not always straightforward as the analysis of bicycle stability shows: a bicycle can roll by itself when given an initial speed, but, other than previously assumed, gyroscopic or caster effects are not required to self-stabilise the bike, although they might be contributing to overall stability [170]. The mass distribution and the front axis tilt in the bike were found to cause self-stability in a complex interaction. It might be that the eccentric wheel hopping mode also is, despite of its simplicity, caused by a complex interaction of various dynamical effects. It is surprising how mechanical systems designed to exploit mechanical self-stability are highly energy effective. The robot *Ranger* [71] based on the passive dynamic walkers uses the inverted pendulum gait and surpasses humanoid robots such as Honda's *Asimo* [171] by a cost of transport roughly 10 times lower. The observation is further supported with the energy efficient hopping robot *Cargo* [39], and in the curved foot hopping robot *CHIARO* [36], where energy effectiveness and stability were

found to be correlated. This thesis reports on a comparable phenomenon, where the robot performance of *Robbit* shows that the stablest gaits, i.e. the ones with the lowest eigenvalue of the return map, are also the most effective ones. The coupling of energy effectiveness and stability might be explained by the eigenvector decomposition of the collision matrix in Appendix A, which provides the collisional energy losses and thus the energy sinks in the system. The most efficient hopping patterns will converge to the least collision loss, which is in this case the proposed locomotion mode. The coupling of efficiency and stability in discretely actuated systems is a recurring phenomenon and might promote understanding the process of self-organisation and self-stability by defining causal relations.

Chapter 6 discussed the benefits of impacts on the locomotion dynamics. Not only was it possible to change the gait of the hopping robot due to the discrete foot shape changes, but additional impacts did not reduce the locomotion speed, but increased it by 40% when the impacts were applied with the right timing. It is not easily understood how the impact improves locomotion speed, as it is a combination of main motor control and environmental interactions which determine the forward hopping locomotion behaviour. What the study clearly underscores is the importance of foot contact point in the process of locomotion, which is what the discrete foot shape change essentially controls. The importance of contact points for control and locomotion stability has been understood since the introduction of zero moment point control [89], where the centre of pressure on the foot, i.e. the current contact point, is defining the stability and control scheme.

7.2 Related Work

The idea of discrete actuation has his roots in the hopping robot *CHIARO*, which I developed as a result of my master's thesis [172]. The motivation behind developing the new robot was the reduction of degrees of freedom in the ankle joint of a previous version, and replacing the torsion spring in the ankle by a curved foot. This was the first step in discretising the behaviour enabled by an element of high complexity (in this case the torsion spring) by pre-programming the behaviour in a rigid shape. Both stability and energetic cost of locomotion were improved by the discretisation through shape [36]. The idea opened up novel possibilities for design and robust locomotion. The robot *Cargo* is based on the design of *CHIARO* and uses the discretised property to achieve one of the lowest cost of transport in a robotic system and highest resilience to changes in payload [38], [39].

The robot platform *CHIARO* has further been used for the study of control input towards the energetic cost of transport. The robot is by default controlled with a sinusoidal control input, but the question arose to what extent this is an optimal solution in terms of the energetic

cost of transport. As discussed in Section 1.1, energy optimality in legged locomotion is often found to approach a discretely actuated system in the limit, with impulses being the most energy effective control input. Indeed, the same observation was obtained in two studies with the hopping robot *CHIARO* [37], [173], where impulsive control inputs lead to most energy effective hopping locomotion.

The complex interaction of morphological parameters and control is difficult to grasp for us humans, especially in higher dimensional morphology and actuation space. The objective function for optimisation of the energetic cost of transport, locomotion speed, or stability is only obtained through the dynamics which are influenced by the intricate interaction between morphology, control, and the environment. In an attempt to study the state of human understanding of causality in morphology and control parameters on the objective, we generated a probabilistic model based on the Bayesian theory to see if a computer can "understand" the physics of a plant as well as a human can [174]. To this end, we applied the developed optimization algorithm on the *CHIARO* platform and asked it to improve locomotion speed by both changing morphology and control iteratively. We phrased the control problem in such a way, that the system is a discretely actuated system, meaning that we only allowed for impulse-like actuation. We found that the optimisation algorithm worked surprisingly well in the context of discrete actuation, and we found that it even outperforms a human engineer in higher-dimensional parameter spaces.

7.3 Future Work

The purpose of discrete actuation is not only to facilitate understanding of stability and energetics on a fundamental physical level, but also to provoke the question how should robots perceive and plan their actions in a natural or man made world? That is, how is the outcome of an action computed efficiently such that it can be used for motion planning? The segmentation of the real world into shapes is an important milestone in making sense of the world. The success of recent computer vision algorithms for image classification supports this view, as it employs deep convolutional neural networks, which essentially separate features in the image which are detected in different layers of the network [175]. These networks are, at least partially, bio inspired [176], but to what extent and how the brain plans its actions is not known. Given the capacity of the brain to understand shapes and its interaction, the solution to efficient motion planning for robots might be in the discretisation of forces and shapes - a dynamic version of deep convolutional neural networks. Such a controller could help to make efficient decisions by providing the minimum necessary information.

One issue in motion planning is the freedom of actuation over time, which renders the problem of finding a solution for the locomotion problem difficult. As we showed in the discretised modelling approach, changes in velocities can be reduced to few instances in time at the impulsive events, thus simplifying the possibilities of control enormously. This is not only more intuitive to think about dynamics, but it also drastically reduces control dimensionality due to the discrete actuation possibilities, which could bolster learning algorithms like reinforcement learning [177] to be applicable to locomotion problems.

A good benchmark for the discretised modelling approach is its use for motion planning in rough terrain. Reinforcement learning has recently shown to be capable of generating locomotion over complex terrain for bipedal and octapedal locomotion [178], and the discretised modelling approach could be tested in a similar approach. At the same time, optimisation methods could be used to compute real-time optimal control in the rough environment with the simplified system. We will use the results to plan locomotion in more complex systems.

As mentioned in the previous section, the coupling of self-stability and energy effective locomotion can be observed in various cases. The discretised modelling approach, and, in particular, the eccentric wheel model can be used as a simple tool to analyse the relationship between the two aspects of locomotion. To this end, the self-stability analysis as presented in Appendix C can be extended to the case where the energy is not mapped back to its initial state over the flight phase. The coupling of energy-effectiveness and stability in discretely actuated systems may be key to understanding certain classes of self-organising systems.

References

[1] David Silver, Aja Huang, Chris J Maddison, Arthur Guez, Laurent Sifre, George Van Den Driessche, Julian Schrittwieser, Ioannis Antonoglou, Veda Panneershelvam, Marc Lanctot, et al. Mastering the game of go with deep neural networks and tree search. *Nature*, 529(7587):484–489, 2016.

[2] Hans Moravec. *Mind children: The future of robot and human intelligence*. Harvard University Press, 1988.

[3] Eric Dietrich. Computationalism. *Social Epistemology*, 4(2):135–154, 1990.

[4] Rolf Pfeifer and Fumiya Iida. Embodied artificial intelligence: Trends and challenges. In *Embodied Artificial Intelligence*, pages 1–26. Springer, 2004.

[5] Gentaro Taga, Yoko Yamaguchi, and Hiroshi Shimizu. Self-organized control of bipedal locomotion by neural oscillators in unpredictable environment. *Biological Cybernetics*, 65(3):147–159, 1991.

[6] Rolf Pfeifer, Fumiya Iida, and Gabriel Gómez. Morphological computation for adaptive behavior and cognition. In *International Congress Series*, volume 1291, pages 22–29. Elsevier, 2006.

[7] Herman Haken. Synergetics. *Physics Bulletin*, 28(9):412, 1977.

[8] Reinhard Blickhan, Andre Seyfarth, Hartmut Geyer, Sten Grimmer, Heiko Wagner, and Michael Günther. Intelligence by mechanics. *Philosophical Transactions of the Royal Society of London A: Mathematical, Physical and Engineering Sciences*, 365(1850):199–220, 2007.

[9] Phillip J Holmes. The dynamics of repeated impacts with a sinusoidally vibrating table. *Journal of Sound and Vibration*, 84(2):173–189, 1982.

[10] Arthur D Kuo. Energetics of actively powered locomotion using the simplest walking model. *Journal of Biomechanical Engineering*, 124(1):113–120, 2002.

[11] Manoj Srinivasan and Andy Ruina. Computer optimization of a minimal biped model discovers walking and running. *Nature*, 439(7072):72, 2006.

[12] Reinhard Blickhan. The spring-mass model for running and hopping. *Journal of Biomechanics*, 22(11-12):1217–1227, 1989.

[13] Tad McGeer et al. Passive dynamic walking. *The International Journal of Robotics Research*, 9(2):62–82, 1990.

[14] Thomas A McMahon. The role of compliance in mammalian running gaits. *Journal of Experimental Biology*, 115(1):263–282, 1985.

[15] R McNeill Alexander. Three uses for springs in legged locomotion. *International Journal of Robotics Research*, 9(2):53–61, 1990.

[16] Claire T Farley, James Glasheen, and Thomas A McMahon. Running springs: speed and animal size. *Journal of Experimental Biology*, 185(1):71–86, 1993.

[17] Thomas A McMahon, Gordon Valiant, and Edward C Frederick. Groucho running. *Journal of Applied Physiology*, 62(6):2326–2337, 1987.

[18] Reinhard Blickhan and Robert J Full. Similarity in multilegged locomotion: bouncing like a monopode. *Journal of Comparative Physiology A: Neuroethology, Sensory, Neural, and Behavioral Physiology*, 173(5):509–517, 1993.

[19] Andre Seyfarth, Hartmut Geyer, Michael Günther, and Reinhard Blickhan. A movement criterion for running. *Journal of Biomechanics*, 35(5):649–655, 2002.

[20] Hartmut Geyer, Andre Seyfarth, and Reinhard Blickhan. Compliant leg behaviour explains basic dynamics of walking and running. *Proceedings of the Royal Society of London B: Biological Sciences*, 273(1603):2861–2867, 2006.

[21] Xiaoxiang Yu and Fumiya Iida. Minimalistic models of an energy-efficient vertical-hopping robot. *IEEE Transactions on Industrial Electronics*, 61(2):1053–1062, 2014.

[22] R McNeill Alexander. A model of bipedal locomotion on compliant legs. *Philosophical Transactions of the Royal Society of London B: Biological Sciences*, 338(1284):189–198, 1992.

[23] Tad McGeer. Passive bipedal running. *Proceedings of the Royal Society of London B: Biological Sciences*, 240(1297):107–134, 1990.

[24] Juergen Rummel and Andre Seyfarth. Stable running with segmented legs. *The International Journal of Robotics Research*, 27(8):919–934, 2008.

[25] H Rad, Pedro Gregorio, and Martin Buehler. Design, modeling and control of a hopping robot. In *proceedings of the IEEE International Conference on Intelligent Robots and Systems (IROS)*, volume 3, pages 1778–1785. IEEE, 1993.

[26] Martin Buhler and Daniel E Koditschek. Analysis of a simplified hopping robot. In *proceedings of the IEEE International Conference on Robotics and Automation (ICRA)*, pages 817–819. IEEE, 1988.

[27] Marc H Raibert. Hopping in legged systems—modeling and simulation for the two-dimensional one-legged case. *IEEE Transactions on Systems, Man, and Cybernetics*, (3):451–463, 1984.

[28] Justin E Seipel, Philip J Holmes, and Robert J Full. Dynamics and stability of insect locomotion: a hexapedal model for horizontal plane motions. *Biological Cybernetics*, 91(2):76–90, 2004.

[29] Alberto E Minetti. The biomechanics of skipping gaits: a third locomotion paradigm? *Proceedings of the Royal Society of London B: Biological Sciences*, 265(1402):1227–1233, 1998.

[30] Marc H Raibert, H Benjamin Brown Jr, and Michael Chepponis. Experiments in balance with a 3d one-legged hopping machine. *The International Journal of Robotics Research*, 3(2):75–92, 1984.

[31] Jesse A Grimes and Jonathan W Hurst. The design of atrias 1.0 a unique monopod, hopping robot. In *proceedings of the International Conference on Climbing and Walking Robots (CLAWAR)*, pages 548–554, 2012.

[32] Sang-Ho Hyon and Tsutomu Mita. Development of a biologically inspired hopping robot-" kenken". In *proceedings of the IEEE International Conference on Robotics and Automation (ICRA)*, volume 4, pages 3984–3991. IEEE, 2002.

[33] Fumiya Iida, Jürgen Rummel, and Andre Seyfarth. Bipedal walking and running with spring-like biarticular muscles. *Journal of Biomechanics*, 41(3):656–667, 2008.

[34] Ben Brown and Garth Zeglin. The bow leg hopping robot. In *proceedings of the IEEE International Conference on Robotics and Automation (ICRA)*, volume 1, pages 781–786. IEEE, 1998.

[35] Murat Reis and Fumiya Iida. Hopping robot based on free vibration of an elastic curved beam. In *proceedings of the IEEE/ASME International Conference on Advanced Intelligent Mechatronics (AIM)*, pages 892–897. IEEE, 2011.

[36] Fabian Gunther, Fabio Giardina, and Fumiya Iida. Self-stable one-legged hopping using a curved foot. In *proceedings of the IEEE International Conference on Robotics and Automation (ICRA)*, pages 5133–5138. IEEE, 2014.

[37] Jonathan Hunt, Fabio Giardina, Andre Rosendo, and Fumiya Iida. Improving efficiency for an open-loop-controlled locomotion with a pulsed actuation. *IEEE/ASME Transactions on Mechatronics*, 21(3):1581–1591, 2016.

[38] Fabian Günther, Yafeng Shu, and Fumiya Iida. Parallel elastic actuation for efficient large payload locomotion. In *proceedings of the IEEE International Conference on Robotics and Automation (ICRA)*, pages 823–828. IEEE, 2015.

[39] Fabian Guenther and Fumiya Iida. Energy-efficient monopod running with a large payload based on open-loop parallel elastic actuation. *IEEE Transactions on Robotics*, 33(1):102–113, 2017.

[40] Robert Ringrose. Self-stabilizing running. In *proceedings of the IEEE International Conference on Robotics and Automation (ICRA)*, volume 1, pages 487–493. IEEE, 1997.

[41] Fabio Giardina and Fumiya Iida. Simulation of forward hopping dynamics in robots and animals using a template with a circular foot and impulsive actuation. In *proceedings of the IEEE International Conference Biomedical Robotics and Biomechatronics (BioRob)*, pages 7–12. IEEE, 2016.

[42] Renaud Ronsse, Philippe Lefèvre, and Rodolphe Sepulchre. Sensorless stabilization of bounce juggling. *IEEE Transactions on Robotics*, 22(1):147–159, 2006.

[43] Philipp Reist and Raffaello D'Andrea. Design and analysis of a blind juggling robot. *IEEE Transactions on Robotics*, 28(6):1228–1243, 2012.

[44] Mariano Garcia, Anindya Chatterjee, Andy Ruina, Michael Coleman, et al. The simplest walking model: stability, complexity, and scaling. *Journal of Biomechanical Engineering ASME*, 120(2):281–288, 1998.

[45] Michael J Coleman, Mariano Garcia, Katja Mombaur, and Andy Ruina. Prediction of stable walking for a toy that cannot stand. *Physical Review E*, 64(2):022901, 2001.

[46] Ambarish Goswami, Benoit Thuilot, and Bernard Espiau. A study of the passive gait of a compass-like biped robot: Symmetry and chaos. *The International Journal of Robotics Research*, 17(12):1282–1301, 1998.

[47] Ambarish Goswami, Bernard Espiau, and Ahmed Keramane. Limit cycles in a passive compass gait biped and passivity-mimicking control laws. *Autonomous Robots*, 4(3):273–286, 1997.

[48] Mariano Garcia, Anindya Chatterjee, and Andy Ruina. Speed, efficiency, and stability of small-slope 2d passive dynamic bipedal walking. In *proceedings of the IEEE International Conference on Robotics and Automation (ICRA)*, volume 3, pages 2351–2356. IEEE, 1998.

[49] Maxine Kwan and Mont Hubbard. Optimal foot shape for a passive dynamic biped. *Journal of Theoretical Biology*, 248(2):331–339, 2007.

[50] Mariano Garcia, Anindya Chatterjee, and Andy Ruina. Efficiency, speed, and scaling of two-dimensional passive-dynamic walking. *Dynamics and Stability of Systems*, 15(2):75–99, 2000.

[51] Andy Ruina, John EA Bertram, and Manoj Srinivasan. A collisional model of the energetic cost of support work qualitatively explains leg sequencing in walking and galloping, pseudo-elastic leg behavior in running and the walk-to-run transition. *Journal of Theoretical Biology*, 237(2):170–192, 2005.

[52] Joachim Hass, J Michael Herrmann, and Theo Geisel. Optimal mass distribution for passivity-based bipedal robots. *The International Journal of Robotics Research*, 25(11):1087–1098, 2006.

[53] C David Remy, Keith Buffinton, and Roland Siegwart. Stability analysis of passive dynamic walking of quadrupeds. *The International Journal of Robotics Research*, 29(9):1173–1185, 2010.

[54] Peter G Adamczyk, Steven H Collins, and Arthur D Kuo. The advantages of a rolling foot in human walking. *Journal of Experimental Biology*, 209(20):3953–3963, 2006.

[55] Fumihiko Asano and Zhi-Wei Luo. The effect of semicircular feet on energy dissipation by heel-strike in dynamic biped locomotion. In *proceedings of the IEEE International Conference on Robotics and Automation (ICRA)*, pages 3976–3981. IEEE, 2007.

[56] Franck Plestan, Jessy W Grizzle, Eric R Westervelt, and Gabriel Abba. Stable walking of a 7-dof biped robot. *IEEE Transactions on Robotics and Automation*, 19(4):653–668, 2003.

[57] Arthur D Kuo. Stabilization of lateral motion in passive dynamic walking. *The International Journal of Robotics Research*, 18(9):917–930, 1999.

[58] Michael J Coleman and Andy Ruina. An uncontrolled walking toy that cannot stand still. *Physical Review Letters*, 80(16):3658, 1998.

[59] Steven H Collins, Martijn Wisse, and Andy Ruina. A three-dimensional passive-dynamic walking robot with two legs and knees. *The International Journal of Robotics Research*, 20(7):607–615, 2001.

[60] Russ Tedrake, Teresa Weirui Zhang, Ming-fai Fong, and H Sebastian Seung. Actuating a simple 3d passive dynamic walker. In *proceedings of the IEEE International Conference on Robotics and Automation (ICRA)*, volume 5, pages 4656–4661. IEEE, 2004.

[61] Kohei Nakajima, Tao Li, Helmut Hauser, and Rolf Pfeifer. Exploiting short-term memory in soft body dynamics as a computational resource. *Journal of The Royal Society Interface*, 11(100):20140437, 2014.

[62] R McNeill Alexander. Walking made simple. *Science*, 308(5718):58–59, 2005.

[63] Yildirim Hürmüzlü and Gordon D Moskowitz. The role of impact in the stability of bipedal locomotion. *Dynamics and Stability of Systems*, 1(3):217–234, 1986.

[64] Anne K Gutmann, David V Lee, and Craig P McGowan. Collision-based mechanics of bipedal hopping. *Biology Letters*, 9(4):20130418, 2013.

[65] Mario Gomes and Andy Ruina. Walking model with no energy cost. *Physical Review E*, 83(3):032901, 2011.

[66] J Maxwell Donelan, Rodger Kram, and Arthur D Kuo. Mechanical work for step-to-step transitions is a major determinant of the metabolic cost of human walking. *Journal of Experimental Biology*, 205(23):3717–3727, 2002.

[67] Arthur D Kuo, Maxwell J Donelan, and Andy Ruina. Energetic consequences of walking like an inverted pendulum: step-to-step transitions. *Exercise and Sport Sciences Reviews*, 33(2):88–97, 2005.

[68] Arthur D Kuo. The six determinants of gait and the inverted pendulum analogy: A dynamic walking perspective. *Human Movement Science*, 26(4):617–656, 2007.

[69] Tad McGeer. Dynamics and control of bipedal locomotion. *Journal of Theoretical Biology*, 163(3):277–314, 1993.

[70] Arthur D Kuo. A simple model of bipedal walking predicts the preferred speed–step length relationship. *Journal of Biomechanical Engineering*, 123(3):264–269, 2001.

[71] Pranav A Bhounsule, Jason Cortell, and Andy Ruina. Design and control of ranger: an energy-efficient, dynamic walking robot. In *proceedings of the International Conference on Climbing and Walking Robots*, pages 441–448, 2012.

[72] Mariano Garcia, Anindya Chatterjee, and Andy Ruina. Efficiency, speed, and scaling of two-dimensional passive-dynamic walking. *Dynamics and Stability of Systems*, 15(2):75–99, 2000.

[73] Mario W Gomes and Andy L Ruina. A five-link 2d brachiating ape model with life-like zero-energy-cost motions. *Journal of Theoretical Biology*, 237(3):265–278, 2005.

[74] Adel Akbarimajd, Majid Nili Ahmadabadi, and Auke Jan Ijspeert. Analogy between juggling and hopping: Active object manipulation approach. *Advanced Robotics*, 25(13-14):1793–1816, 2011.

[75] Anindya Chatterjee, R Pratap, CK Reddy, and Andy Ruina. Persistent passive hopping and juggling is possible even with plastic collisions. *The International Journal of Robotics Research*, 21(7):621–634, 2002.

[76] Umberto Scarfogliero, Cesare Stefanini, and Paolo Dario. Design and development of the long-jumping" grillo" mini robot. In *proceedings of the IEEE International Conference on Robotics and Automation (ICRA)*, pages 467–472. IEEE, 2007.

[77] Mirko Kovac, Martin Fuchs, André Guignard, Jean-Christophe Zufferey, and Dario Floreano. A miniature 7g jumping robot. In *proceedings of the IEEE International Conference on Robotics and Automation (ICRA)*, pages 373–378. IEEE, 2008.

[78] Duncan W Haldane, MM Plecnik, Justin K Yim, and Ronald S Fearing. Robotic vertical jumping agility via series-elastic power modulation. *Science Robotics*, 1(1):eaag2048, 2016.

[79] Fabio Giardina and Fumiya Iida. Discrete foot shape changes improve dynamics of a hopping robot. In *International Symposium on Experimental Robotics*, pages 113–122. Springer, 2016.

[80] Manoj Srinivasan and Andy Ruina. Idealized walking and running gaits minimize work. In *Proceedings of the Royal Society of London A: Mathematical, Physical and Engineering Sciences*, volume 463, pages 2429–2446. The Royal Society, 2007.

[81] John EA Bertram and Andy Ruina. Multiple walking speed–frequency relations are predicted by constrained optimization. *Journal of Theoretical Biology*, 209(4):445–453, 2001.

[82] Russ Tedrake, Teresa Weirui Zhang, and H Sebastian Seung. Stochastic policy gradient reinforcement learning on a simple 3d biped. In *proceedings of the IEEE International Conference on Intelligent Robots and Systems (IROS)*, volume 3, pages 2849–2854. IEEE, 2004.

[83] Katie Byl and Russ Tedrake. Metastable walking machines. *The International Journal of Robotics Research*, 28(8):1040–1064, 2009.

[84] Ian R Manchester, Uwe Mettin, Fumiya Iida, and Russ Tedrake. Stable dynamic walking over uneven terrain. *The International Journal of Robotics Research*, 30(3):265–279, 2011.

[85] Eric R Westervelt, Jessy W Grizzle, and Daniel E Koditschek. Hybrid zero dynamics of planar biped walkers. *IEEE Transactions on Automatic Control*, 48(1):42–56, 2003.

[86] Marc H Raibert. *Legged robots that balance*. MIT press, 1986.

[87] Marc Raibert, Michael Chepponis, and HBJR Brown. Running on four legs as though they were one, 1986.

[88] Jerry Pratt, Chee-Meng Chew, Ann Torres, Peter Dilworth, and Gill Pratt. Virtual model control: An intuitive approach for bipedal locomotion. *The International Journal of Robotics Research*, 20(2):129–143, 2001.

[89] Miomir Vukobratović and Branislav Borovac. Zero-moment point—thirty five years of its life. *International Journal of Humanoid Robotics*, 1(01):157–173, 2004.

[90] Mark W Spong. Passivity based control of the compass gait biped. In *IFAC world congress*, volume 3, pages 19–23, 1999.

[91] Justin Seipel and Philip Holmes. A simple model for clock-actuated legged locomotion. *Regular and Chaotic Dynamics*, 12(5):502–520, 2007.

[92] André Seyfarth, Hartmut Geyer, and Hugh Herr. Swing-leg retraction: a simple control model for stable running. *Journal of Experimental Biology*, 206(15):2547–2555, 2003.

[93] Uluc Saranli, Martin Buehler, and Daniel E Koditschek. Rhex: A simple and highly mobile hexapod robot. *The International Journal of Robotics Research*, 20(7):616–631, 2001.

[94] Richard Altendorfer, Uluc Saranli, Haldun Komsuoglu, Daniel Koditschek, H Benjamin Brown, Martin Buehler, Ned Moore, Dave McMordie, and Robert Full. Evidence for spring loaded inverted pendulum running in a hexapod robot. In *Experimental Robotics VII*, pages 291–302. Springer, 2001.

[95] Fumiya Iida and Rolf Pfeifer. Cheap rapid locomotion of a quadruped robot: Self-stabilization of bounding gait. In *Intelligent Autonomous Systems*, volume 8, pages 642–649. IOS Press, 2004.

[96] Sten Grillner. Locomotion in vertebrates: central mechanisms and reflex interaction. *Physiological Reviews*, 55(2):247–304, 1975.

[97] Auke Jan Ijspeert. Central pattern generators for locomotion control in animals and robots: a review. *Neural Networks*, 21(4):642–653, 2008.

[98] Auke Jan Ijspeert, Alessandro Crespi, Dimitri Ryczko, and Jean-Marie Cabelguen. From swimming to walking with a salamander robot driven by a spinal cord model. *Science*, 315(5817):1416–1420, 2007.

[99] Hartmut Geyer and Hugh Herr. A muscle-reflex model that encodes principles of legged mechanics produces human walking dynamics and muscle activities. *IEEE Transactions on Neural Systems and Rehabilitation Engineering*, 18(3):263–273, 2010.

[100] C. R. Taylor, N. C. Heglund, and G. M. Maloiy. Energetics and mechanics of terrestrial locomotion. i. metabolic energy consumption as a function of speed and body size in birds and mammals. *Journal of Experimental Biology*, 97(1):1–21, 1982.

[101] R McNeil Alexander. Estimates of speeds of dinosaurs. *Nature*, 261(5556):129–130, 1976.

[102] Robert J Full and Michael S Tu. Mechanics of a rapid running insect: two-, four-and six-legged locomotion. *Journal of Experimental Biology*, 156(1):215–231, 1991.

[103] R McNeill Alexander. Walking and running: Legs and leg movements are subtly adapted to minimize the energy costs of locomotion. *American Scientist*, 72(4):348–354, 1984.

[104] R McNeill Alexander. Simple models of human locomotion. *Computational and Mathematical Methods in Medicine*, 1(2):129–135, 1997.

[105] R McNeill Alexander. Simple models of walking and jumping. *Human movement science*, 11(1):3–9, 1992.

[106] Simon Mochon and Thomas A McMahon. Ballistic walking. *Journal of Biomechanics*, 13(1):49–57, 1980.

[107] Thomas A McMahon. Mechanics of locomotion. *The International Journal of Robotics Research*, 3(2):4–28, 1984.

[108] Christoph Glocker. Energetic consistency conditions for standard impacts. *Multibody System Dynamics*, 29(1):77–117, 2013.

[109] Christoph Glocker and Christian Studer. Formulation and preparation for numerical evaluation of linear complementarity systems in dynamics. *Multibody System Dynamics*, 13(4):447–463, 2005.

[110] Christian Walter Studer. *Augmented time-stepping integration of non-smooth dynamical systems*. PhD thesis, ETH Zurich, 2008.

[111] Terence J Dawson and C Richard Taylor. Energetic cost of locomotion in kangaroos. *Nature*, 246(5431):313–314, 1973.

[112] Ajij Sayyad, B Seth, and P Seshu. Single-legged hopping robotics research—a review. *Robotica*, 25(5):587–613, 2007.

[113] Robert J Full and Daniel E Koditschek. Templates and anchors: neuromechanical hypotheses of legged locomotion on land. *Journal of Experimental Biology*, 202(23):3325–3332, 1999.

[114] Frank Peuker, Christophe Maufroy, and André Seyfarth. Leg-adjustment strategies for stable running in three dimensions. *Bioinspiration & Biomimetics*, 7(3):036002, 2012.

[115] Ke-Jung Huang, Chun-Kai Huang, and Pei-Chun Lin. A simple running model with rolling contact and its role as a template for dynamic locomotion on a hexapod robot. *Bioinspiration & Biomimetics*, 9(4):046004, 2014.

[116] Jingjing Liu, Hongbo Wang, Hongnian Yu, Lili Zhang, Luige Vladareanu, Adrian Bruja, and Gal I Alexandru. Design of a new solution for the wheeled hopping robot. In *proceedings of the UKACC International Conference on Control*, pages 720–724. IEEE, 2014.

[117] Vance A Tucker. The energetic cost of moving about: walking and running are extremely inefficient forms of locomotion. much greater efficiency is achieved by birds, fish—and bicyclists. *American Scientist*, 63(4):413–419, 1975.

[118] Jo Yung Wong. *Terramechanics and off-road vehicle engineering: terrain behaviour, off-road vehicle performance and design*. Butterworth-Heinemann, 2009.

[119] H Shibly, Karl Iagnemma, and S Dubowsky. An equivalent soil mechanics formulation for rigid wheels in deformable terrain, with application to planetary exploration rovers. *Journal of Terramechanics*, 42(1):1–13, 2005.

[120] George R Mastroianni, Michael F Zupan, Donna M Chuba, Robert C Berger, and Alfred L Wile. Voluntary pacing and energy cost of off-road cycling and running. *Applied Ergonomics*, 31(5):479–485, 2000.

[121] Hamid Taghavifar and Aref Mardani. *Off-road Vehicle Dynamics*. Springer, 2017.

[122] Rodolfo Margaria. *Biomechanics and energetics of muscular exercise*. Oxford University Press, USA, 1976.

[123] David V Lee, John EA Bertram, Jennifer T Anttonen, Ivo G Ros, Sarah L Harris, and Andrew A Biewener. A collisional perspective on quadrupedal gait dynamics. *Journal of the Royal Society Interface*, 2011.

[124] James R Usherwood and John EA Bertram. Understanding brachiation: insight from a collisional perspective. *Journal of Experimental Biology*, 206(10):1631–1642, 2003.

[125] Steven H Collins and Andy Ruina. A bipedal walking robot with efficient and human-like gait. In *proceedings of the IEEE International Conference on Robotics and Automation (ICRA)*, pages 1983–1988. IEEE, 2005.

[126] Thomas Libby, Talia Y Moore, Evan Chang-Siu, Deborah Li, Daniel J Cohen, Ardian Jusufi, and Robert J Full. Tail-assisted pitch control in lizards, robots and dinosaurs. *Nature*, 481(7380):181, 2012.

[127] Ambarish Goswami and Vinutha Kallem. Rate of change of angular momentum and balance maintenance of biped robots. In *proceedings of the IEEE International Conference on Robotics and Automation (ICRA)*, volume 4, pages 3785–3790. IEEE, 2004.

[128] Jonas Rubenson, Denham B Heliams, David G Lloyd, and Paul A Fournier. Gait selection in the ostrich: mechanical and metabolic characteristics of walking and running with and without an aerial phase. *Proceedings of the Royal Society B: Biological Sciences*, 271(1543):1091, 2004.

[129] Brandon M Kilbourne and Louwrens C Hoffman. Scale effects between body size and limb design in quadrupedal mammals. *PLoS One*, 8(11):e78392, 2013.

[130] Richard L Marsh, David J Ellerby, Jennifer A Carr, Havalee T Henry, and Cindy I Buchanan. Partitioning the energetics of walking and running: swinging the limbs is expensive. *Science*, 303(5654):80–83, 2004.

[131] Jiro Doke, J Maxwell Donelan, and Arthur D Kuo. Mechanics and energetics of swinging the human leg. *Journal of Experimental Biology*, 208(3):439–445, 2005.

[132] R McNeil Alexander and Alexandra Vernon. The mechanics of hopping by kangaroos (macropodidae). *Journal of Zoology*, 177(2):265–303, 1975.

[133] MA Fedak, NC Heglund, and CR Taylor. Energetics and mechanics of terrestrial locomotion. ii. kinetic energy changes of the limbs and body as a function of speed and body size in birds and mammals. *Journal of Experimental Biology*, 97(1):23–40, 1982.

[134] Donald F Hoyt, Steven J Wickler, and Edward A Cogger. Time of contact and step length: the effect of limb length, running speed, load carrying and incline. *Journal of Experimental Biology*, 203(2):221–227, 2000.

[135] Norman C Heglund and C Richard Taylor. Speed, stride frequency and energy cost per stride: how do they change with body size and gait? *Journal of Experimental Biology*, 138(1):301–318, 1988.

[136] R McNeill Alexander and AS Jayes. A dynamic similarity hypothesis for the gaits of quadrupedal mammals. *Journal of zoology*, 201(1):135–152, 1983.

[137] Matt Haberland, JG Daniël Karssen, Sangbae Kim, and Martijn Wisse. The effect of swing leg retraction on running energy efficiency. In *proceedings of the IEEE International Conference on Intelligent Robots and Systems (IROS)*, pages 3957–3962. IEEE, 2011.

[138] Herman Pontzer. Predicting the energy cost of terrestrial locomotion: a test of the limb model in humans and quadrupeds. *Journal of Experimental Biology*, 210(3):484–494, 2007.

[139] Marc Raibert, Kevin Blankespoor, Gabriel Nelson, and Rob Playter. Bigdog, the rough-terrain quadruped robot. *IFAC Proceedings Volumes*, 41(2):10822–10825, 2008.

[140] R McNeill Alexander. Energy-saving mechanisms in walking and running. *Journal of Experimental Biology*, 160(1):55–69, 1991.

[141] Jack M Winters. Hill-based muscle models: a systems engineering perspective. In *Multiple Muscle Systems*, pages 69–93. Springer, 1990.

[142] Gill A Pratt and Matthew M Williamson. Series elastic actuators. In *proceedings of the IEEE International Conference on Intelligent Robots and Systems (IROS)*, volume 1, pages 399–406. IEEE, 1995.

[143] Joel Burdick and Paolo Fiorini. Minimalist jumping robots for celestial exploration. *The International Journal of Robotics Research*, 22(7-8):653–674, 2003.

[144] Mohanarajah Gajamohan, Michael Merz, Igor Thommen, and Raffaello D'Andrea. The cubli: A cube that can jump up and balance. In *proceedings of the IEEE International Conference on Intelligent Robots and Systems (IROS)*, pages 3722–3727. IEEE, 2012.

[145] Benjamin J Hockman, Andreas Frick, Robert G Reid, Issa AD Nesnas, and Marco Pavone. Design, control, and experimentation of internally-actuated rovers for the exploration of low-gravity planetary bodies. *Journal of Field Robotics*, 34(1):5–24, 2017.

[146] John W Romanishin, Kyle Gilpin, Sebastian Claici, and Daniela Rus. 3d m-blocks: Self-reconfiguring robots capable of locomotion via pivoting in three dimensions. In *proceedings of the IEEE International Conference on Robotics and Automation (ICRA)*, pages 1925–1932. IEEE, 2015.

[147] Boston Dynamics. Sandflea jumping robot. *retrieved at https://www.bostondynamics.com/sandflea*, 2018.

[148] Ross Allen, Marco Pavone, Christopher McQuin, Issa AD Nesnas, Julie C Castillo-Rogez, Tam-Nguyen Nguyen, and Jeffrey A Hoffman. Internally-actuated rovers for all-access surface mobility: Theory and experimentation. In *proceedings of the IEEE International Conference on Robotics and Automation (ICRA)*, pages 5481–5488. IEEE, 2013.

[149] Vance A Tucker. Energetic cost of locomotion in animals. *Comparative Biochemistry and Physiology*, 34(4):841–846, 1970.

[150] Steve Collins, Andy Ruina, Russ Tedrake, and Martijn Wisse. Efficient bipedal robots based on passive-dynamic walkers. *Science*, 307(5712):1082–1085, 2005.

[151] Giovanni A Cavagna, Norman C Heglund, and C Richard Taylor. Mechanical work in terrestrial locomotion: two basic mechanisms for minimizing energy expenditure. *American Journal of Physiology-Regulatory, Integrative and Comparative Physiology*, 233(5):R243–R261, 1977.

[152] Shuuji Kajita, Fumio Kanehiro, Kenji Kaneko, Kazuhito Yokoi, and Hirohisa Hirukawa. The 3d linear inverted pendulum mode: A simple modeling for a biped walking pattern generation. In *proceedings of the IEEE International Conference on Intelligent Robots and Systems (IROS)*, volume 1, pages 239–246. IEEE, 2001.

[153] Jimmy Sastra, Sachin Chitta, and Mark Yim. Dynamic rolling for a modular loop robot. *The International Journal of Robotics Research*, 28(6):758–773, 2009.

[154] Keith W Wait, Philip J Jackson, and Lanny S Smoot. Self locomotion of a spherical rolling robot using a novel deformable pneumatic method. In *proceedings of the IEEE International Conference on Robotics and Automation (ICRA)*, pages 3757–3762. IEEE, 2010.

[155] Richard Chase and Abhilash Pandya. A review of active mechanical driving principles of spherical robots. *Robotics*, 1(1):3–23, 2012.

[156] Jun Ho Choi and JW Grizzle. Feedback control of an underactuated planar bipedal robot with impulsive foot action. *Robotica*, 23(5):567–580, 2005.

[157] Yildirim Hürmüzlü and Gordon D Moskowitz. Bipedal locomotion stabilized by impact and switching: I. two-and three-dimensional, three-element models. *Dynamics and Stability of Systems*, 2(2):73–96, 1987.

[158] Theodosios Pavlidis. Stability of systems described by differential equations containing impulses. *IEEE Transactions on Automatic Control*, 12(1):43–45, 1967.

[159] Xiuping Mu and Qiong Wu. On impact dynamics and contact events for biped robots via impact effects. *IEEE Transactions on Systems, Man, and Cybernetics, Part B (Cybernetics)*, 36(6):1364–1372, 2006.

[160] SD Perry and MA Lafortune. Influences of inversion/eversion of the foot upon impact loading during locomotion. *Clinical Biomechanics*, 10(5):253–257, 1995.

[161] Daniel Mellinger, Vijay Kumar, and Mark Yim. Control of locomotion with shape-changing wheels. In *proceedings of the IEEE International Conference on Robotics and Automation (ICRA)*, pages 1750–1755. IEEE, 2009.

[162] Rhodri H Armour and Julian FV Vincent. Rolling in nature and robotics: a review. *Journal of Bionic Engineering*, 3(4):195–208, 2006.

[163] Mario García-París and Stephen M Deban. A novel antipredator mechanism in salamanders: rolling escape in hydromantes platycephalus. *Journal of Herpetology*, 29(1):149–151, 1995.

[164] JR Henschel. Spiders wheel to escape. *South African Journal of Science*, 86(3):151–152, 1990.

[165] Gerhard Scholtz. Scarab beetles at the interface of wheel invention in nature and culture? *Contributions to Zoology*, 77(3), 2008.

[166] Robert Full, Kathleen Earls, Mary Wong, and Roy Caldwell. Locomotion like a wheel? *Nature*, 365(6446):495–495, 1993.

[167] John Brackenbury. Caterpillar kinematics. *Nature*, 390(6659):453, 1997.

[168] R McNeill Alexander. *Principles of animal locomotion*. Princeton University Press, 2003.

[169] John R Hutchinson and Mariano Garcia. Tyrannosaurus was not a fast runner. *Nature*, 415(6875):1018–1021, 2002.

[170] JDG Kooijman, Jacob Philippus Meijaard, Jim M Papadopoulos, Andy Ruina, and AL Schwab. A bicycle can be self-stable without gyroscopic or caster effects. *Science*, 332(6027):339–342, 2011.

[171] Masato Hirose and Kenichi Ogawa. Honda humanoid robots development. *Philosophical Transactions of the Royal Society of London A: Mathematical, Physical and Engineering Sciences*, 365(1850):11–19, 2007.

[172] Fabio Giardina. Development and analysis of a self-stable, one-legged hopping robot. Master's thesis, ETH Zurich, 2013.

[173] Steve Heim. Dynamics and control for efficient hopping. Master's thesis, ETH Zurich, 2013.

[174] Kaur Aare Saar, Fabio Giardina, and Fumiya Iida. Model-free design optimization of a hopping robot and its comparison with a human designer. *IEEE Robotics and Automation Letters*, 3(2):1245–1251, 2018.

[175] Alex Krizhevsky, Ilya Sutskever, and Geoffrey E Hinton. Imagenet classification with deep convolutional neural networks. In *Advances in Neural Information Processing Systems*, pages 1097–1105, 2012.

[176] David H Hubel and Torsten N Wiesel. Receptive fields and functional architecture of monkey striate cortex. *The Journal of Physiology*, 195(1):215–243, 1968.

[177] Richard S Sutton and Andrew G Barto. *Reinforcement learning: An introduction*, volume 1. MIT press Cambridge, 1998.

[178] Nicolas Heess, Srinivasan Sriram, Jay Lemmon, Josh Merel, Greg Wayne, Yuval Tassa, Tom Erez, Ziyu Wang, Ali Eslami, Martin Riedmiller, et al. Emergence of locomotion behaviours in rich environments. *arXiv preprint arXiv:1707.02286*, 2017.

Appendix A

Energetic Analysis of the Eccentric Wheel Collision

A.1 Eigenvalues and Eigenvectors of the Collision Matrix

The eigenvectors and eigenvalues of the collision matrix are crucial for analysis and comparison of the three strategies given in Chapter 4. The collision matrix is defined as in Chapter 2 with

$$\mathbf{M}_c = -\mathbf{J}_c^T \left(\mathbf{J}_c \mathbf{M}^{-1} \mathbf{J}_c^T\right)^{-1} \mathbf{J}_c. \tag{A.1}$$

The eigenvalues of the collision matrix for a collision with flat ground are

$$\lambda_R = 0, \quad \lambda_{TH} = m, \quad \lambda_{RH} = \frac{mI(k+1)}{mk+I}, \tag{A.2}$$

and the corresponding eigenvectors are

$$\boldsymbol{v}_R = \frac{1}{\sqrt{1+k}} \begin{bmatrix} -k_1 \\ -k_2 \\ 1 \end{bmatrix}, \quad \boldsymbol{v}_{TH} = \frac{k_1}{\sqrt{k}} \begin{bmatrix} -k_1/k_2 \\ 1 \\ 0 \end{bmatrix}, \quad \boldsymbol{v}_{RH} = \sqrt{\frac{k}{1+k}} \begin{bmatrix} k_1/k \\ k_2/k \\ 1 \end{bmatrix}, \tag{A.3}$$

where the subscript R stands for rolling, TH for trivial hopping, and RH for rotational hopping. The k- values are defined as $k_1 = R - a\cos\phi$, $k_2 = -a\sin\phi$, and $k = k_1^2 + k_2^2$. Pure rolling is described for $\lambda_R, \boldsymbol{v}_R$ which explains the vanishing eigenvalue and therefore energy loss. When no eccentricity is modelled ($a = 0$), the pair $\lambda_{TH}, \boldsymbol{v}_{TH}$ describes the trivial hopping strategy loss factor and pre-touchdown velocity, respectively. When an eccentricity is modelled ($0 < a < R$), the pair $\lambda_{RH}, \boldsymbol{v}_{RH}$ corresponds to the rotational hopping strategy

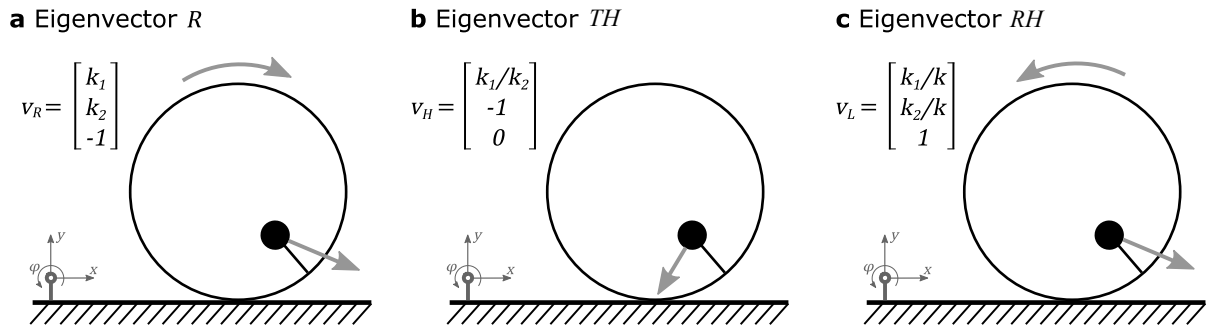

Fig. A.1 **Interpretation of eigenvectors**. Qualitative ground approach velocities for (a) rolling strategy, (b) trivial hopping strategy (with off-centred mass) and (c) rotational hopping strategy.

loss factor and pre-touchdown velocity, respectively. The eigenvectors can be interpreted as touchdown conditions for the corresponding cases, as illustrated in Figure A.1.

A.2 Wheel-Obstacle Energy Loss due to Collision

For the rolling strategy, we use the generalised rolling velocity before impact

$$\boldsymbol{u}_R = \|\boldsymbol{u}_R\| \sqrt{R^2+1}\,[R,0,-1]^T$$

which corresponds to a wheel rolling on flat ground. The energy loss at collision can simply be obtained from the collision matrix. We assume the coefficient of restitution to be negligible, thus allowing for inelastic collisions. We obtain the energetic loss at collision

$$\Delta E_R = \frac{1}{2}\boldsymbol{u}_R^T \mathbf{M}_c \boldsymbol{u}_R = \frac{m\|\boldsymbol{u}_R\|^2}{2}\,\frac{hR\left(2mR^2 - Rhm + 2I\right)}{\left(mR^2+I\right)\left(R^2+1\right)}. \tag{A.4}$$

A.3 Limit Case of Hopping vs. Rolling

For the trivial hopping strategy, we assume the energy needed to hop over the obstacle is simply proportional to the potential energy required to lift the system onto the obstacle. The energy is added before the collision to avoid the obstacle. Therefore

$$\Delta E_{TH} = mgh. \tag{A.5}$$

If the obstacle height is decreased until its limit is reached, a clear distinction can be made for which regions the hopping or rolling strategy become optimal. We take the collision loss of rolling and divide it by the collision loss for hopping as the obstacle height h goes to zero

$$\lim_{h\to 0}\frac{\Delta E_R}{\Delta E_{TH}} = \lim_{h\to 0}\frac{\|\boldsymbol{u}_R\|^2}{g}\left(\frac{R}{R^2+1} - \frac{hmR^2}{2(mR^2+I)(R^2+1)}\right) = \frac{\|\boldsymbol{u}_R\|^2}{g}\frac{R}{R^2+1} \tag{A.6}$$

We take the definition of the rolling velocity $\boldsymbol{u}_R = \|\boldsymbol{u}_R\|\sqrt{R^2+1}\,[R,0,-1]^T$ and get for the forward velocity $u_x = \boldsymbol{u}_R\|R/\sqrt{R^2+1}$. Substitution into Equation (A.6) gives

$$\lim_{h\to 0}\frac{\Delta E_R}{\Delta E_{TH}} = u_x^2\frac{\sqrt{R^2+1}^2}{gR^2}\frac{R}{R^2+1} = \frac{u_x^2}{gR} = Fr, \tag{A.7}$$

with Fr the Froude number of the system. Hence, for negligible obstacle heights, the Froude number gives an indication for the superiority of locomotion strategy, i.e. for $Fr > 1$ hopping is optimal, and for Fr<1 rolling is optimal.

For the non-limit case, we obtain

$$\frac{\Delta E_R}{\Delta E_{TH}} = Fr\left(1 - \frac{hmR}{2(mR^2+I)}\right) = Fr\left(1 - \frac{h/R}{2(1+\alpha)}\right), \tag{A.8}$$

with $\alpha = I/mR^2$. Worst efficiency ratio for hopping occurs when $h = R$ and $\alpha \to 0$, which results in $\Delta E_R/\Delta E_{TH} = Fr/2$. A Froude number of 2 therefore defines the lower optimality limit for hopping over rolling.

A.4 Eigenvalue Ratio

The eigenvalues of the collision matrix determine the energy loss of the collision according to the generalised velocity vector. The conditions for which the rotational hopping strategy is superior to the hopping strategy can be investigated by comparing their eigenvalues, as both pre-collision velocities correspond to a distinct eigenvector for these two cases. The eigenvalue corresponding to the hopping strategy is $\lambda_H = m$ and Equation (A.2) for the rotational hopping strategy.

$$\frac{\lambda_H}{\lambda_L} = \frac{mk+I}{I(k+1)} \tag{A.9}$$

We are interested in the case that $\lambda_H/\lambda_L > 1$, i.e. the rotational hopping strategy superior to the hopping strategy. Hence

$$mk + I > I(k+1) \tag{A.10}$$

$$m > I \tag{A.11}$$

for $k > 0$.

Appendix B

Extension to Chapter 5

The four derivatives in (5.18) have to be computed with care, as some of the occurring partial derivatives do not address quantities that are given in an analytic explicit expression, but rather by a differential equation or an implicit equation. To dissect the expressions we can rewrite (5.18) to

$$\mathbf{A} = \begin{bmatrix} \frac{d\Gamma_1}{d\phi_{TD}} & \frac{d\Gamma_1}{d\dot{\phi}^+_{TD}} \\ \frac{d\Gamma_2}{d\phi_{TD}} & \frac{d\Gamma_2}{d\dot{\phi}^+_{TD}} \end{bmatrix} \begin{bmatrix} K_{1\phi} & K_{2\dot{\phi}} \\ K_{1\phi} & K_{2\dot{\phi}} \end{bmatrix} \Big|_{\phi_0,\dot{\phi}_0}. \tag{B.1}$$

with the suffix *TD* indicating the touchdown state and with

$$K_{1\phi} := \left[\frac{\partial \phi_{TD}}{\partial \phi} + \frac{d\phi_{TD}}{d\dot{\phi}^+_{TO}} \left(\frac{\partial \dot{\phi}^+_{TO}}{\partial \phi} + \frac{d\dot{\phi}^+_{TO}}{d\dot{\phi}^-_{TO}} \frac{d\dot{\phi}^-_{TO}}{d\phi} \right) \right] \Big|_{\phi_0,\dot{\phi}_0}, \tag{B.2}$$

$$K_{1\dot{\phi}} := \left[\frac{\partial \dot{\phi}^+_{TD}}{\partial \phi} + \frac{d\dot{\phi}^+_{TD}}{d\dot{\phi}^-_{TD}} \left(\frac{\partial \dot{\phi}^-_{TD}}{\partial \phi} + \frac{d\dot{\phi}^-_{TD}}{d\dot{\phi}^+_{TO}} \left(\frac{\partial \dot{\phi}^+_{TO}}{\partial \phi} + \frac{d\dot{\phi}^+_{TO}}{d\dot{\phi}^-_{TO}} \frac{d\dot{\phi}^-_{TO}}{d\phi} \right) \right) \right] \Big|_{\phi_0,\dot{\phi}_0}, \tag{B.3}$$

$$K_{2\phi} := \left[\frac{\partial \phi_{TD}}{\partial \dot{\phi}} + \frac{d\phi_{TD}}{d\dot{\phi}^+_{TO}} \left(\frac{\partial \dot{\phi}^+_{TO}}{\partial \dot{\phi}} + \frac{d\dot{\phi}^+_{TO}}{d\dot{\phi}^-_{TO}} \frac{d\dot{\phi}^-_{TO}}{d\dot{\phi}} \right) \right] \Big|_{\phi_0,\dot{\phi}_0}, \tag{B.4}$$

and

$$K_{2\dot{\phi}} := \left[\frac{\partial \dot{\phi}^+_{TD}}{\partial \dot{\phi}} + \frac{d\dot{\phi}^+_{TD}}{d\dot{\phi}^-_{TD}} \left(\frac{\partial \dot{\phi}^-_{TD}}{\partial \dot{\phi}} + \frac{d\dot{\phi}^-_{TD}}{d\dot{\phi}^+_{TO}} \left(\frac{\partial \dot{\phi}^+_{TO}}{\partial \dot{\phi}} + \frac{d\dot{\phi}^+_{TO}}{d\dot{\phi}^-_{TO}} \frac{d\dot{\phi}^-_{TO}}{d\dot{\phi}} \right) \right) \right] \Big|_{\phi_0,\dot{\phi}_0}. \tag{B.5}$$

Computation of most of the terms in (B.1) are straight forward to calculate through (5.11) to (5.15). Special attention however is required for the left-hand side matrix in (B.1), as these derivatives are effectively influencing the result of an integration rather than a closed form expression. To calculate the derivatives, we define the sensitivity with respect to our parameters of interest $p_1 = \phi_{TD}$ and $p_2 = \dot{\phi}_{TD}$ as $\boldsymbol{r}_i = \frac{d\boldsymbol{z}}{dp_i}$. Through differentiation of (5.15)

by p_i, we obtain

$$\dot{\boldsymbol{r}}_i = \frac{d\boldsymbol{f}}{d\boldsymbol{z}}\boldsymbol{r}_i + \frac{d\boldsymbol{f}}{dp_i}, \quad i \in \{1,2\}, \tag{B.6}$$

where $\boldsymbol{f}$ is the right-hand side of (5.15) and the last term drops out since $\boldsymbol{f}$ does not depend on the post-touchdown states. Solving this ODE with initial conditions $\boldsymbol{r}_1(\boldsymbol{z}_0) = (1,0)^T$ and $\boldsymbol{r}_2(\boldsymbol{z}_0) = (0,1)^T$ until $z_1 = \phi_0$, will provide all entries in the left-hand side matrix in (B.1) for the case of an open-loop controlled system. However, our controller is stopping not as a function of time, but as a function of the impulse ζ. In other words, in the shown sensitivity analysis, we did not account for the effect that a disturbance has on the stance phase time t_s. To include this, we first express (5.15) as a function of ζ rather than t. This requires a change of variable with

$$\frac{d\boldsymbol{z}}{dt} = \frac{d\boldsymbol{z}}{d\zeta}\frac{d\zeta}{dt}, \tag{B.7}$$

and therefore get

$$\frac{d\boldsymbol{z}}{d\zeta} = \frac{\dot{\boldsymbol{z}}}{\dot{\zeta}} = \frac{\boldsymbol{f}}{\dot{\zeta}}. \tag{B.8}$$

The derivative of the impulse can be derived from (5.8) to (5.9)

$$\dot{\zeta} = \frac{I_S I_R}{I_S + I_R}\left(\frac{T}{t_s} - \dot{z}_2\right). \tag{B.9}$$

It remains to change the coordinates in (B.6) in terms of impulse instead of time

$$\frac{d\boldsymbol{r}_i}{d\zeta} = \left(\frac{1}{\dot{\zeta}}\frac{d\boldsymbol{f}}{d\boldsymbol{z}} - \frac{\boldsymbol{f}}{\dot{\zeta}^2}\frac{\dot{\zeta}}{d\boldsymbol{z}}\right)\boldsymbol{r}_i. \tag{B.10}$$

The solution of Equation (B.10) now truly leads to the entries of the left-hand side of (B.1) for our control method, as we can simply integrate to the impulse limit ζ_0. Note that in (B.10) we assume knowledge of $z(\zeta)$. If this is not given, the system has to be augmented to a system of four rather than two ODEs, where the additional ODEs are given by (B.8).

The derivatives which derive post-flight phase states require attention, as the equations of the flight time are only given implicitly. More specifically the terms $\frac{\partial \phi_{TD}}{\partial \phi_0}$ and $\frac{\partial \phi_{TD}}{\partial \dot{\phi}^+_{TO}}$ are

$$\begin{aligned}\frac{\partial \phi_{TD}}{\partial \phi_0} &= \frac{\partial}{\partial \phi_0}\left(\phi_0 + \dot{\phi}^+_{TO} t_F(\phi_0, \dot{\phi}^+_{TO})\right) \\ &= 1 + \dot{\phi}^+_{TO}\frac{dt_F}{d\phi_0}\end{aligned} \tag{B.11}$$

and accordingly

$$\frac{\partial \phi_{TD}}{\partial \dot{\phi}_{TO}^{+}} = t_F + \dot{\phi}_{TO}^{+} \frac{dt_F}{d\dot{\phi}_{TO}^{+}}. \tag{B.12}$$

To find the derivatives of the flight time t_F, we simply take the derivative of the implicit Equation (5.12) and solve for $\frac{dt_F}{d\phi_0}$ and $\frac{dt_F}{d\dot{\phi}_{TO}^{+}}$, which yields

$$\frac{dt_F}{d\phi_0} = \frac{-a\sin\phi_0 - \dot{\phi}_{TO}^{+} a t_F \cos\phi_0 + a\sin(\phi_0 + \dot{\phi}_{TO}^{+} t_F)}{\dot{\phi}_{TO}^{+} a\sin\phi_0 - g t_F - a\dot{\phi}_{TO}^{+}\sin(\phi_0 + \dot{\phi}_{TO}^{+} t_F)}, \tag{B.13}$$

and

$$\frac{dt_F}{d\dot{\phi}_{TO}^{+}} = \frac{-a t_F \sin\phi_0 + a t_F \sin(\phi_0 + \dot{\phi}_{TO}^{+} t_F)}{\dot{\phi}_{TO}^{+} a\sin\phi_0 - g t_F - a\dot{\phi}_{TO}^{+}\sin(\phi_0 + \dot{\phi}_{TO}^{+} t_F)}. \tag{B.14}$$

We used the relation $y = R - a\cos\phi_0$ and $\dot{y} = \dot{\phi}_{TO}^{+} a\cos\phi_0$ to replace the vertical position and velocity components in (5.12). The remaining terms of (B.1) are easily calculated.

Appendix C

Self-Stability of the Impulsive Wheel

The example given in this appendix is to demonstrate the power of self-stabilising principles using discrete actuation. The following calculations can help to understand open-loop stability of robots like [36] and [39], where a curved foot facilitates energy effective and stable forward hopping through simple control. The example presented here is introducing the impulsive wheel model, which, in analogy to the model presented in Chapter 3, uses translational impulses as a source of actuation. The resulting dynamics can be described by a simple return map, and analysis can be done using common tools from nonlinear dynamics.

The model used here assumes that the mass is located at the centre of the wheel, which renders its stance phase energy independent of the impulse. This simplifies the analysis enormously while still keeping the self-stabilising property. As we will see, when the right impulse magnitude is applied, the wheel angular position will be stabilised around a fixed point, hinting to the fundamental self-stability property of such systems.

C.1 The impulsive Wheel Model

The impulsive wheel model is depicted in Figure C.1. The wheel has a mass m, a moment of inertia around the centre of mass I, and a radius R. We are given a rolling velocity $\dot{\phi}_S$ and an impulse $\boldsymbol{\zeta} = [\zeta_x, \zeta_y]^T$ which is applied to the wheel every T_C seconds at the wheel-ground contact point. We would like to answer the question if the take-off angle ϕ_{TO}^i can be stabilised, that is, as time goes to infinity, the angle at the impulsive events is constant and the average rotation over one gait cycle is zero (as opposed to perpetually rotating in one direction). The wheel exploits the backward rotation which is induced by the impulse to do so. The direction of the impulse is with respect to a body-fixed direction measured with the angle ϕ from the

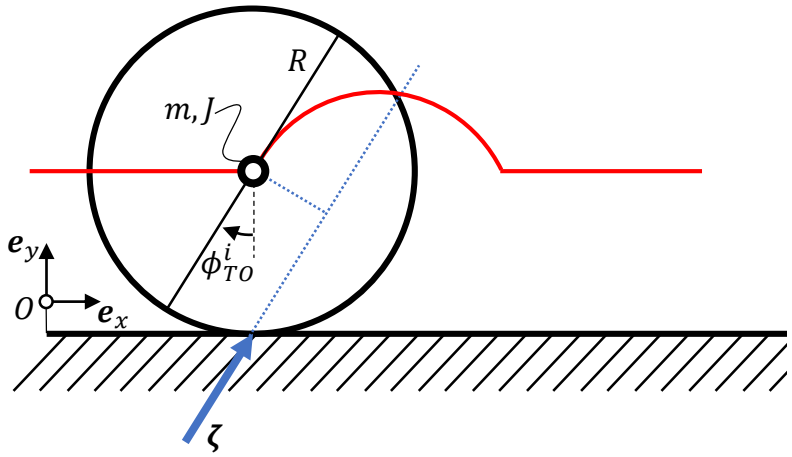

Fig. C.1 Impulsive wheel model subject to impulse $\boldsymbol{\zeta}$ with mass m, moment of inertia around the centre of mass I, and radius R. The take-off angle at iteration i measured in the inertial frame of reference O to a body-fixed reference is described with the angle ϕ^i_{TO}.

vertical axis of an inertial coordinate frame O. The impulse is thus

$$\boldsymbol{\zeta} = \|\boldsymbol{\zeta}\| \begin{pmatrix} -\sin\phi \\ \cos\phi \end{pmatrix}. \tag{C.1}$$

The impulse will cause a transition from rolling to a ballistic motion, which is governed by the momentum balance $\boldsymbol{u}^+ = \mathbf{M}^{-1}\mathbf{J}_c^T\boldsymbol{\zeta} + \boldsymbol{u}^-$, with $\boldsymbol{u}$ the generalised velocity of the system, $\mathbf{M}$ the mass matrix, $\mathbf{J}_c$ the contact Jacobian for the ground, and the superscripts $+$ and $-$ indicate post and pre impulse states, respectively. In the case of a wheel with centred mass, the rolling condition for the pre impuse velocity, and the impulsive force as per Equation (C.1), this yields

$$\begin{pmatrix} \dot{x}^+ \\ \dot{y}^+ \\ \dot{\phi}^+ \end{pmatrix} = \begin{bmatrix} \frac{1}{m} & 0 & 0 \\ 0 & \frac{1}{m} & 0 \\ 0 & 0 & \frac{1}{J} \end{bmatrix} \begin{bmatrix} 1 & 0 \\ 0 & 1 \\ R & 0 \end{bmatrix} \begin{pmatrix} -\sin\phi \\ \cos\phi \end{pmatrix} \|\boldsymbol{\zeta}\| + \begin{pmatrix} -R\dot{\phi}^- \\ 0 \\ \dot{\phi}^- \end{pmatrix}. \tag{C.2}$$

We are interested in the stabilisation of the angular position. The relevant flight phase speed is thus

$$\dot{\phi}_F = -\frac{R}{I}\|\boldsymbol{\zeta}\|\sin\phi + \dot{\phi}_S, \tag{C.3}$$

where $\dot{\phi}_F$ stands for the flight phase angular velocity, and $\dot{\phi}_S$ for the stance phase angular velocity. The impulsive transition is followed by a flight phase of the wheel, which has a

flight phase time

$$t_F = \frac{2\dot{y}}{g} = \frac{2\|\boldsymbol{\zeta}\|\cos\phi}{mg}, \tag{C.4}$$

where g is the gravitational acceleration. We can now map the current take-off angle to the next one, given the system parameters and impulsive actuation, with

$$\phi_{TO}^{i+1} = \phi_{TO}^{i} + t_F\dot{\phi}_F + \dot{\phi}_S\,(T_C - t_F)\,, \tag{C.5}$$

where the subscript TO indicates the take-off state, and the superscript i stands for the iteration number. The equation simply states that the next take-off angle is current take-off angle plus the angular displacements during flight and stance, with the stance phase time being simply the difference between the actuation period and the flight phase time $T_C - t_F$. Note that we are only interested in cases where the flight phase is smaller than the actuation period and will not include other cases in the subsequent analysis. By using definitions (C.3) and (C.4), we obtain

$$\phi_{TO}^{i+1} = \phi_{TO}^{i} - \frac{2R\|\boldsymbol{\zeta}\|^2}{mIg}\sin\phi_{TO}^{i}\cos\phi_{TO}^{i} + \dot{\phi}_S T_C. \tag{C.6}$$

We slightly change the notation of this expression and write

$$\phi_{TO}^{i+1} = \phi_{TO}^{i} - c\sin 2\phi_{TO}^{i} + \dot{\phi}_S T_C, \tag{C.7}$$

where $c = \frac{R\|\boldsymbol{\zeta}\|^2}{mIg}$.

Next, we want to find fixed points of this discrete map, meaning that we want to find take-off angles ϕ^* for which $\phi_{TO}^{i+1} = \phi_{TO}^{i}$. The solution is easily obtained from Equation (C.7) and reads

$$\phi^* = \frac{1}{2}\sin^{-1}\frac{\dot{\phi}_S T_C}{c}. \tag{C.8}$$

This equation shows that there are initial conditions for which the impulsive actuation maps the angle back to itself. We are interested in stability of the hopping motion and therefore need to check whether perturbations in the angle will cause the dynamics to diverge or converge to the equilibrium point. To that end, we calculate the eigenvalue of the return map (C.7) by

$$\frac{\partial\phi_{TO}^{i+1}}{\partial\phi_{TO}^{i}}\Big|_{\phi^*} = 1 - 2\sqrt{c^2 - \dot{\phi}_S^2 T_C^2}. \tag{C.9}$$

the requirement for locally asymptotic stability is that the absolute value of the eigenvalue of the return map is smaller than one, thus

$$\lambda = |1 - 2\sqrt{c^2 - \dot{\phi}_S^2 T_C^2}| < 1. \tag{C.10}$$

This equation defines bounds on the magnitude of the impulse, which are

$$\|\zeta\|_{min} = \sqrt{\frac{\dot{\phi}_S T_C}{c_0}} \tag{C.11}$$

and

$$\|\zeta\|_{max} = \sqrt{\frac{1}{c_0}\sqrt{1 + \dot{\phi}_S^2 T_C^2}}, \tag{C.12}$$

where $c_0 = \frac{R}{mIg}$. The analysis is therefore concluded and we showed that there exists an impulse interval for which the fixed points ϕ^* are locally asymptotically stable, as clearly $\|\zeta\|_{min} < \|\zeta\|_{max}$.

C.2 Discrete-Time Dynamics of the Impulsive Wheel

Through a numerical simulation, we find that for $\lambda > 1$ we find period doubling bifurcations and the system stays stable in the sense of Lyapunov due to higher-order terms. Figure C.2 shows the bifurcation diagram for the hopping wheel with increasing impulse magnitude and fixed parameters mass $m = 1$, Radius $R = 1$, moment of inertia $I = 1$, gravitational acceleration $g = 9.81$, actuator period $T_C = 1$, and kinetic energy during rolling $E_0 = 1$.

The iteration-series shown in Figure C.3 displays the behaviour for increasing impulse with the same system parameters as in the bifurcation diagram. The system shows asymptotic stability for impulses $3.3\frac{\mathrm{kg\,m}}{\mathrm{s}}$, $3.7\frac{\mathrm{kg\,m}}{\mathrm{s}}$, and $3.74\frac{\mathrm{kg\,m}}{\mathrm{s}}$, before the behaviour switches to stability in the sense of Lyapunov with $4\frac{\mathrm{kg\,m}}{\mathrm{s}}$ and $4.2\frac{\mathrm{kg\,m}}{\mathrm{s}}$. At an impulse of $4.3\frac{\mathrm{kg\,m}}{\mathrm{s}}$, the take-off angle clearly diverges over the hopping iterations.

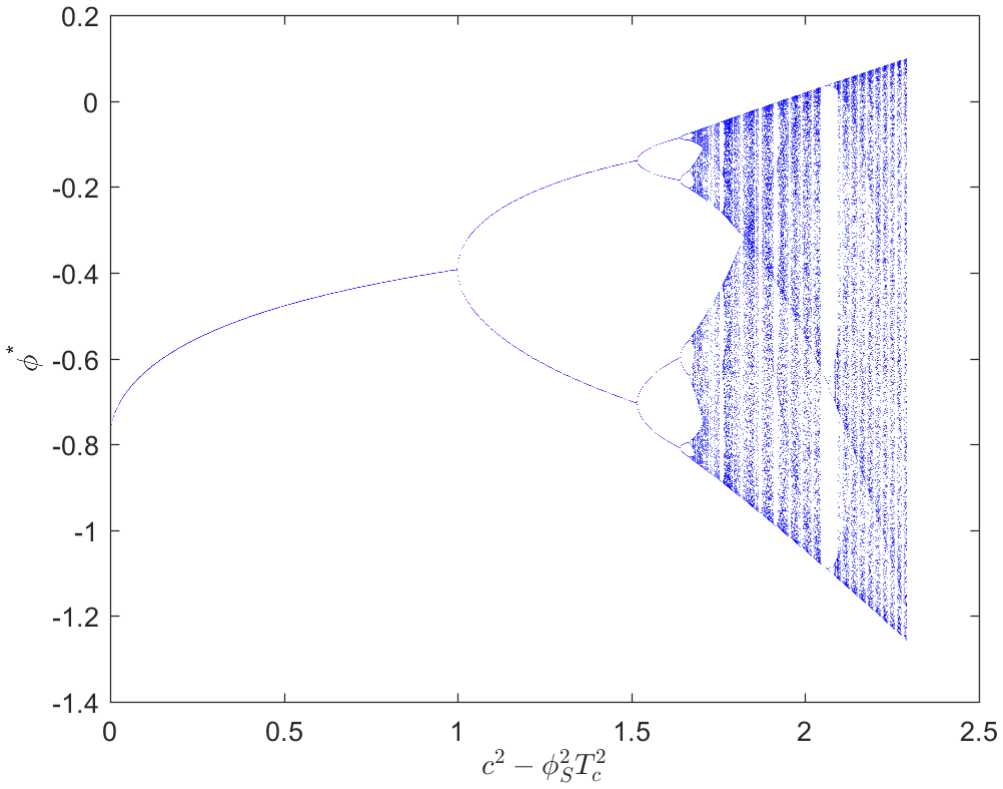

Fig. C.2 Bifurcation diagram of impulsive wheel. Parameters are parameters mass $m = 1$, Radius $R = 1$, moment of inertia $I = 1$, gravitational acceleration $g = 9.81$, actuator period $T_C = 1$, and kinetic energy during rolling $E_0 = 1$.

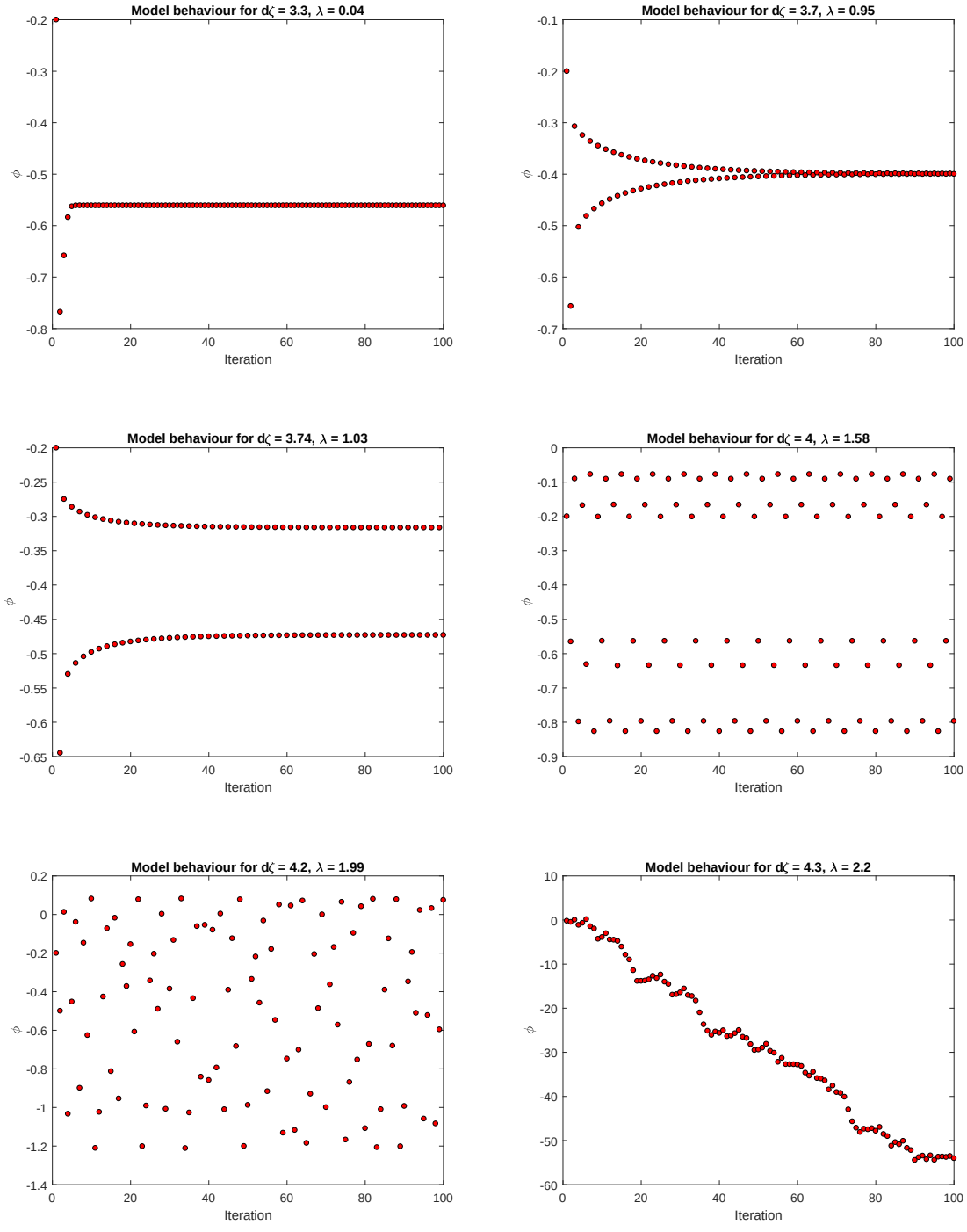

Fig. C.3 Iteration-series of impulsive wheel for various impulse magnitudes. Fixed parameters are mass $m = 1$, Radius $R = 1$, moment of inertia $I = 1$, gravitational acceleration $g = 9.81$, actuator period $T_C = 1$, and kinetic energy during rolling $E_0 = 1$.